Politecnico di Torino

Politecnico di Torino

Corso di Laurea Magistrale in Ingegneria Biomedica
A.A. 2021/2022
Sessione di Laurea Ottobre 2022

Modeling pathological spread through brain connectome in the frontotemporal lobar degeneration spectrum

Relatore:
Prof. Filippo Molinari

Correlatori:
Prof. Massimo Filippi
Prof. Federica Agosta
Dr. Silvia Basaia

Tesi di Laurea di:
Federica Facente

A mio nonno,

Per aver creduto in me e in questo percorso prima di chiunque altro.

Ai miei genitori,

Per tutto l'amore e la forza che mi trasmettono ogni giorno.

TABLE OF CONTENTS

ABSTRACT 7

CHAPTER 1: INTRODUCTION 11

1.1 FTLD 11
1.1.1 FTLD spectrum 11
1.1.2 Epidemiology 12
1.1.3 Neuropathology 12
1.1.3.1 Tau 13
1.1.3.2 TDP-43 14
1.1.4 FTLD spreading 15
1.1.5 Clinical presentation and diagnostic criteria 17
1.1.6 Treatments 18
1.2 MAGNETIC RESONANCE IMAGING (MRI) 20
1.2.1 MRI basic principle 21
1.2.2 Diffusion-weighted MRI 28
1.2.2.1 Diffusion Tensor Imaging 31
1.2.2.2 Tractography 32
1.2.2.3 Neurite orientation dispersion and density imaging 33
1.2.3 Functional MRI 35
1.2.4 Imaging in FTLD 37
1.3 CONNECTOME AND GRAPH ANALYSIS 41
1.3.1 Connectomics 41
1.3.3 Structural and functional connectome in FTLD 46
1.3.4 Network Diffusion Model 52

CHAPTER 2: AIM OF THE PROJECT 55

CHAPTER 3: MATERIAL AND METHODS 56

3.1 PARTICIPANTS 56
3.2 MRI ACQUISITION 58
3.3 MRI ANALYSIS 58
3.3.1 Brain Parcellation 58
3.3.2 T1-Weighted Image Processing 59
3.3.3 Diffusion MRI Processing 59
3.3.3.1 Pre-Processing 59
3.3.3.2 DTI 60
3.3.3.3 NODDI 61
3.3.3.4 Tractography 61
3.3.4 Structural matrices construction 64
3.3.5 Resting-State fMRI Processing 65
3.3.6 Functional matrices construction 65
3.3.7 Graph metrics 66
3.3.8 Network Based Statistics 67
3.3.9 Network Diffusion Model 67
3.3.10 Structural-functional correlations 70

CHAPTER 4: RESULTS 72

4.1 GRAPH METRICS 72
4.2 NETWORK BASED STATISTICS 76
4.3 NETWORK DIFFUSION MODEL 79
4.4 STRUCTURAL-FUNCTIONAL CORRELATIONS 87

CHAPTER 5: DISCUSSION AND CONCLUSIONS 89

APPENDIX.....95
ACKNOWLEDGMENTS.....97
BIBLIOGRAPHY.....99

ABSTRACT

Objective. This study aimed firstly to investigate structural and functional alterations in the brain network of frontotemporal lobar degeneration (FTLD) spectrum using connectome analysis with advanced diffusion-weighted MRI techniques, such as NODDI model, and resting state fMRI (RS fMRI). The second objective was to predict spatiotemporal patterns of neurodegeneration in FTLD exploring the relationship between selective network vulnerability and longitudinal pathological in patients, using a network-based model of pathology spread (NDM).

Materials. Thirty-four behavioral-variant frontotemporal dementia (bvFTD), 11 semantic variant primary progressive aphasia (svPPA) and 11 nonfluent variant primary progressive aphasia (nfvPPA) patients and 48 healthy middle-age controls (aged 41-85 years) were enrolled and underwent single multi-shell diffusion MRI and RS fMRI and longitudinal T1-weighted MRI on a 3T scanner. In order to implement the NDM, 48 healthy young controls (aged 20-31 years) underwent a single multi-shell diffusion MRI scan and a single T1-weighted MRI on a 3T scanner.

Methods. Fractional anisotropy (FA) maps were computed. Intra-cellular Volume Fraction (ICVF) and Orientation Dispersion Index (ODI) maps were estimated using the NODDI model, providing a direct quantification of neurite morphology and its integrity. Graph analysis and connectomics assessed global and local structural and functional topological network properties and regional structural and functional connectivity. In particular, mean distance (MD), eigenvector centrality (EC), degree centrality (DC) and sum of node weights (SN) metrics were obtained. A Network Diffusion Model (NDM) was developed to assess whether the progression of FTLD pathology over time can be modeled by a spreading process, originating from a single regional seed and then proceeding through the healthy structural connectome. The connectivity measures used to create the structural connectome were FA, ICVF and functional connectivity. Three disease epicenters were identified from the peaks of atrophy of each FTLD variant: left inferior temporal gyrus (svPPA), right orbitofrontal cortex (bvFTD) and left supplementary motor area (nfvPPA). Correlations were tested between the longitudinal atrophic changes estimated by NDM and those empirically obtained in FTLD patients over a follow-up of 24 months, by using Pearson's correlation coefficient. Finally, to assess the relationship between structural and

functional connectivity, Pearson's correlation analysis was performed in each group, between FA and functional connectivity and between ICVF and functional connectivity.

Results. Overall, widespread structural changes were observed in bvFTD patients relative to healthy controls. bvFTD patients showed altered structural FA network properties (higher MD and lower DC, SN and EC) also compared svPPA patients. nfvPPA patients showed altered FA properties (higher DC, SN and EC and lower MD) at global level compared to healthy controls. This condition was also verified at a lobar level, in particular in frontal, basal ganglia, parietal, and temporal areas. In contrast, graph analysis applied on functional matrices did not show any significant results. However, considering ICVF measure, a greater altered connections was detected compared to FA maps that allowed to find differences also between svPPA and nfvPPA patients. In addition, ICVF graph analysis measures also showed that svPPA had a lower DC and SN in the temporal lobe compared to healthy controls. The predictive maps obtained by NDM in young controls suggested an early spread of pathology to the left occipital lobe (6 months) and the left inferior frontal lobe (12 months). At 18 months, the left parietal lobe would be reached, whereas in the right hemisphere only few regions in the parietal and occipital lobes would be affected at 24 months. In the case of bvFTD, NDM showed an early spread to the frontal lobe and basal ganglia (6 months) and to the right sensorimotor, parietal, temporal and occipital lobe (12 months), with an involvement of the controlateral hemisphere between 18 and 24 months. In nfvPPA, NDM predicted a pathology spread through all brain regions, except for the occipital lobe, which would be involved after 12 months. Moreover, the degree of atrophy predicted in each region by NDM in healthy young subjects connectome was significantly positively correlated with the longitudinal pattern of patients atrophy in all three FTLD variants ($p<0.05$). Overall, pathology diffusion predicted by NDM applied on ICVF connectome pointed out higher values of correlation related to atrophy predicted by NDM applied on FA maps. In addition, NDM applied on functional matrices also revealed significant results. In svPPA patients, correlations with NDM applied on functional matrices demonstrated higher values of correlation in respect to NDM applied on FA and ICVF connectome. Finally,

in all groups of subjects both structural measures FA and ICVF were significantly positively correlated with functional strength ($p<0.05$).

Discussion. These findings suggested that conventional diffusion-tensor measures might be sensitive enough to highlight connections vulnerable in the FTLD spectrum. In contrast, functional connectivity analysis did not show significant results, suggesting that structural alterations may be earlier in the course of the disease compared to functional network abnormalities. Moreover, ICVF demonstrated to be a clinically relevant more specific biomarker to differentiate syndromes of FTLD spectrum. Specifically, the benefits emerged in the differentiation between svPPA patients and other groups. Moreover, the strong correlations found between the longitudinal atrophic changes estimated by NDM and the empirical longitudinal atrophy patterns support the hypothesis that the healthy architecture of the structural connectome might influence the spatiotemporal progression of atrophy in each FTLD variant. The accuracy values of each model also showed that ICVF had also a greater specificity than FA to model pathology spread. NDM showed significant results also applied on functional matrices. In addition, positive correlations between structural and functional connectivity suggest that structural and functional measures might be combined in order to predict the pathology spreading where both of them demonstrate higher strength connectivity in the network to obtain more relevant results.

Conclusions. Connectome-analysis based on advanced diffusion-weighted models may be useful to evaluate structural disruptions with greater differentiation among FTLD spectrum disorders compared to diffusion-tensor derived measures. Moreover, the implementation of NDM to cross-sectional structural connectome data is a valuable tool to predict future atrophy patterns and pathology spreading in the main variants of the FTLD spectrum.

CHAPTER 1: INTRODUCTION

1.1 FTLD

1.1.1 FTLD spectrum

Frontotemporal lobar degeneration (FTLD) is an umbrella term used to describe a spectrum of neurodegenerative diseases characterized by progressive deficits in behaviour, executive function, and/or language. FTLD patients show neurodegeneration of the frontal and/or temporal lobes with a relative sparing of posterior brain regions, accompanied by protein inclusions (such as tau, TDP-43 or FUS) [1-3].

FTLD spectrum includes frontotemporal dementia (FTD) clinical syndromes, and it is characterized by three main syndromes defined by different early and predominant symptoms (Figure 1): a behavioural-dysexecutive disorder (behavioral variant of fronto-temporal dementia [bvFTD]), the most frequent syndrome; language variants (primary progressive aphasia [PPA]) characterized either by impaired speech production (nonfluent variant [nfvPPA]) or impaired word comprehension and semantic memory (semantic variant [svPPA]); and motor disorders which can present as atypical parkinsonisms (progressive supranuclear palsy [PSP] and corticobasal [CBS] syndromes) or motor neuron disease (MND).

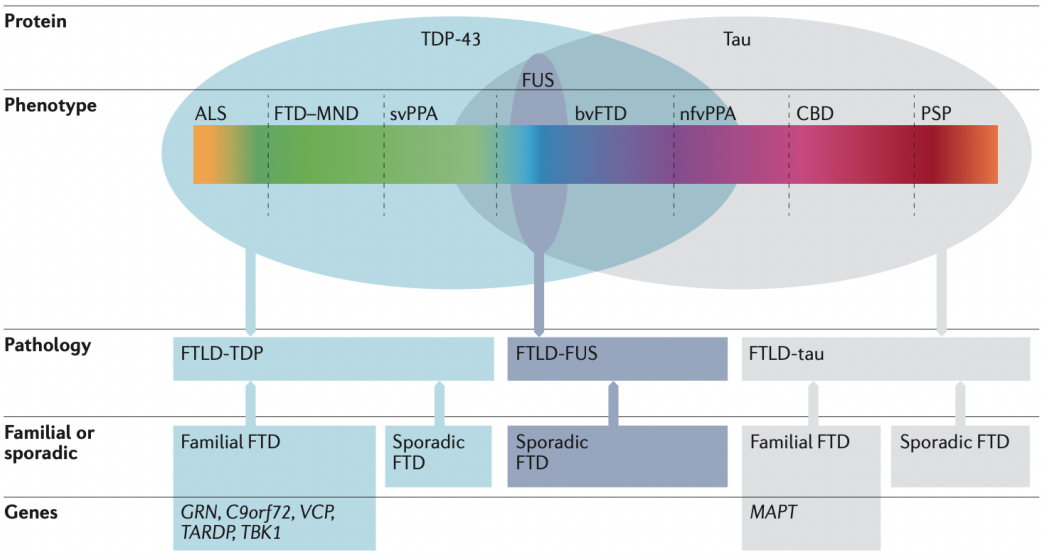

Figure 1: Clinical, pathological and genetic spectrum of FTD [1].

FTLD is a strongly genetic disorder, with 10-20% of cases associated to mutations in the genes MAPT, GRN and C9orf72 [4].
Advanced MRI techniques allowed to define biomarkers able to differentiate variants within FTLD spectrum, examining white matter (WM) and gray matter (GM) impairments.

1.1.2 Epidemiology

FTLD is the second most common cause of dementia in patients younger than 65 years old, after Alzheimer's disease (AD). Dementia affects an estimated 47.5 million people, and 7.7 million new cases are reported each year [5]. However, because the disorder is uncommon in a relatively large at-risk population, it is challenging to estimate the overall population with underlying FTD pathology. Additionally, studies estimating incidence and prevalence rates of FTD are limited by the inherent difficulty identifying FTD disorders [6]. The clinical onset of FTD typically occurs between the age of 45 and 65 years, with a prevalence ranging from 15 to 22 per 100,000 people, and incidence from 2.7 to 4.1 per 100,000 members in this age range [7]. An Italian study in 2019 estimated that the incidence of FTLD in the Italian population is 3.05 per 100.000 person-years and that the bvFTD was the most common phenotype (37%) [8].
FTLD showed a median survival from diagnosis of 7-13 years in clinical cohorts and 6-8 years in studies involving neuropathological confirmed cases. The three main variants of FTD - bvFTD, svPPA, nfvPPA - as well as CBS and PSP, showed nearly equal survival. Concerning MND cases, the life expectancy was severely reduced, with a median survival of 3-5 years [9, 10].

1.1.3 Neuropathology

FTLD syndromes are depicted by deposition of abnormally aggregated proteins in neurons and glial cells, similarly to other neurodegenerative diseases such as AD and Parkinson's disease (PD). Abnormal conformation of these proteins leads to a pathological condition. FTLD spectrum is subdivided according to the presence of one of the following three proteins: tau, TDP-43 and FUS. Tau and TDP-43 cause misfolding of same-species proteins and are able to propagate via cell-to-cell transmission along network connections and across synapses ("prion-like" hypothesis)

(Figure 2) [11]. FTLD-tau and FTLD-TDP pathologies affect most of the FTLD cases and are equally represented. FTLD-FUS has been less studied than the other variants as it is less common [12-14].

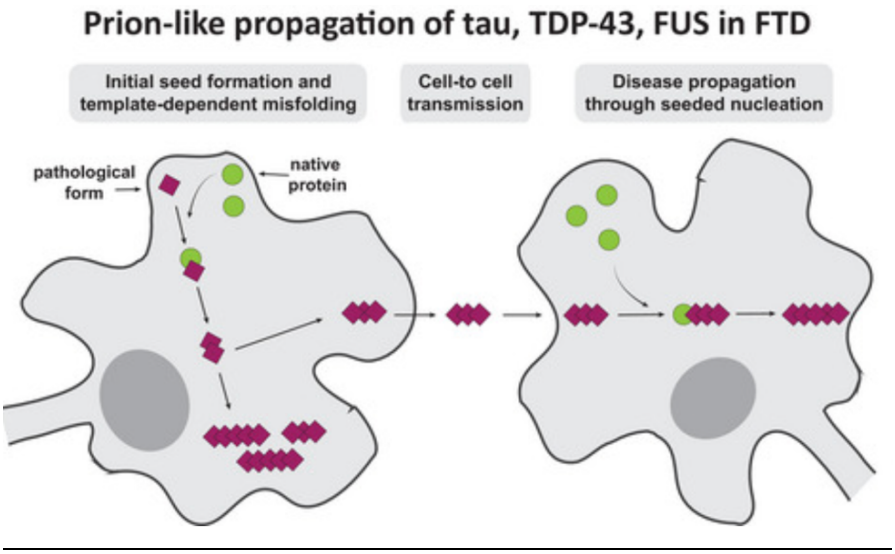

Figure 2: Prion-like propagation [15].

1.1.3.1 Tau

Tau is a microtubule-associated protein (MAPT); its task is the stabilization of microtubules. Human Tau is encoded on chromosome 17q21 [16]. The protein occurs mainly in the central nervous system (CNS) axons and consists largely of six isoforms generated by alternative splicing [17], with a length of protein product ranging between 352 and 441 amino acids. They differ in the presence or absence of two near-amino-terminal inserts of 29 residues each, encoded by exons 2 and 3, and in one of the repeats (R2, 31 residues) in the carboxy-terminal half [18]. Exon 10 inclusion results in 3-repeat or 3R tau, whereas exclusion results in 4-repeat or 4R tau. In healthy patients, 4R and 3R tau presence is balanced [19]. Different tauopathies demonstrate preferential accumulation of 3R and 4R forms, leading to an alter ability of tau to bind to microtubules, caused by an hyperphosphorylation mechanism, and a consequent abnormal tau aggregation (neurofibrillary tangles) [19, 20]. Disorders in which tau pathology is considered the major contributing factor to neurodegeneration are referred to as “primary tauopathies”, while in “secondary tauopathies”, tau aggregation is regarded as a response to other pathological proteins, like amyloid beta (Aβ) in AD [21].

1.1.3.2 TDP-43

TDP-43 is a DNA and RNA binding protein involved in critical RNA processing mechanism [22], such as splicing, microRNA (miRNA) biogenesis, RNA transport, translation and stability, and stress granule formation by interacting with numerous heterogeneous nuclear ribonucleoproteins (hnRNPs), splicing factors and microprocessor proteins [23]. TDP-43 is a 414 amino acid protein that is expressed by the TARDBP gene on chromosome 1. It has two RNA recognition motifs (RRMs) before a glycine-rich, low-sequence complexity prion-like domain [24]. TDP can shuttle between nucleus and cytoplasm, but predominantly resides in the nucleus [25-27]. Through an auto-feedback mechanism TDP-43 maintains its own regulation [28, 29]. When this homeostasis fails, aggregation of abnormal phosphorylation and ubiquitination of TDP-43 is found in cytoplasm, with associated clearing of TDP-43 from the nucleus [30]. Increased cytoplasmatic concentration of TDP-43 provokes prion-like spread, thus degenerating in gain-of-toxic properties and loss-of-function of TDP-43 (Figure 3) [31].

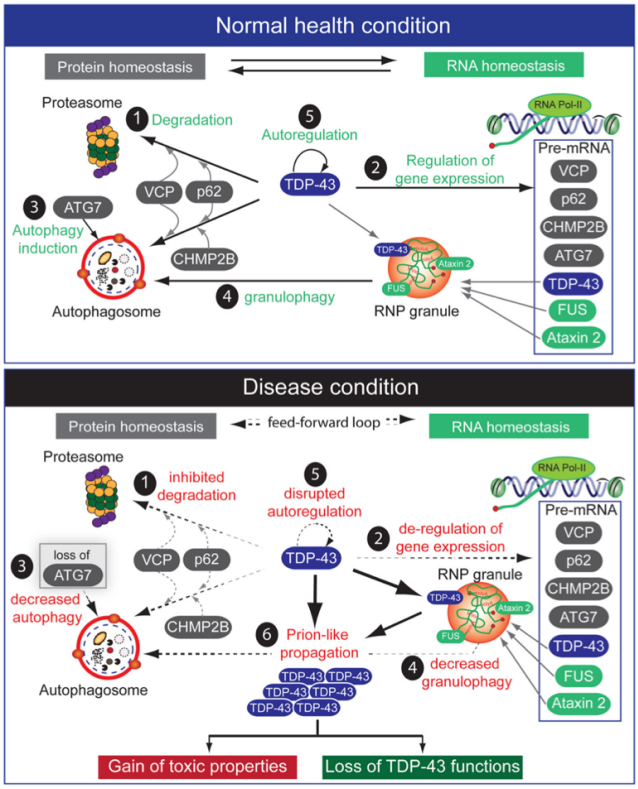

Figure 3:Above: normal health condition of TDP-42 autoregolation; Below: Illustration of disrupted TDP-43 autoregolation and consequent prion-like propagation [31].

TDP-43 is the major disease protein in FTD and ALS (Neumann et al, 2006). FTLD-TDP pathologies are subdivided according to pattern and distribution of TDP-43 [32]:

- type A: presence of neuronal cytoplasmic inclusions (NCI) and dystrophic neurites (DN) in the same proportion (commonly associated to nfvPPA);
- type B: predominance of NCI over DN (commonly associated to FTD-ALS);
- type C: predominance of DN over NCI (commonly associated to svPPA);
- type D: neuronal intranuclear inclusions (NII) are the main histological finding.

1.1.4 FTLD spreading

As mentioned above, spread of FTLD pathologies might be explained by a prion-like mechanism: disease beginning in the gray matter with accumulation of misfolded protein and progressing along fiber pathways. Current studies aim to characterize pattern of disease neurodegeneration over time. Indeed, bvFTD demonstrated sequential dissemination of TDP-43 from frontal lobe to other regions, being described in four patterns of spreading (Figure 4) [33]. In particular, the orbital gyri, rectus, and amygdala are initially involved in bvFTD patients with the lowest pathological burden (pattern I). Lesions appeared in the middle frontal and anterior cingulate gyri, as well as in the superior and medial temporal gyri, striatum, red nucleus, thalamus, and precerebellar nuclei, with increasing disease burden (pattern II). More advanced cases displayed a third pattern (pattern III) with involvement of the motor cortex, bulbar somatomotor neurons, and the spinal cord anterior horn, while patients with the highest damage (pattern IV) were defined by TDP-43 accumulation also in the visual cortex [33].

Moreover, TDP-43 pathology in ALS possibly disseminates in a sequential pattern that permits recognition of four neuropathological stages consistent with the hypothesis that TDP-43 pathology spreads along axonal pathways (Figure 5) [34]. Particularly lesions in the agranular motor cortex, brainstem motor nuclei of cranial nerves and spinal cord -motoneurons were the hallmarks of ALS individuals with the lowest load of TDP-43 pathology (stage 1). Middle frontal gyrus, brainstem reticular formation, precerebellar nuclei, and the red nucleus were involved as the disease burden increased (stage 2). The prefrontal, postcentral neocortex, and striatum were all damaged by TDP-43 disease in stage 3. The hippocampus and other anteromedial areas of the

temporal lobe displayed TDP-43 inclusions in cases with the highest burden of ALS disease (stage 4) [34].

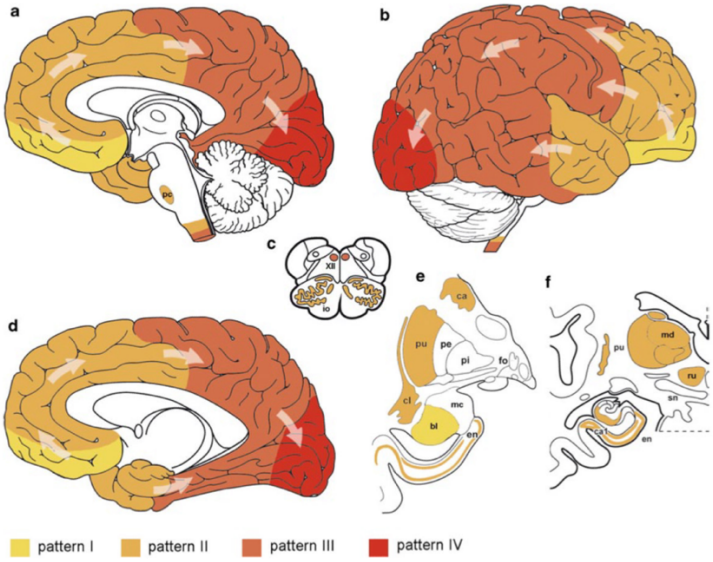

Figure 4: bvFTD pathological patterns [33].

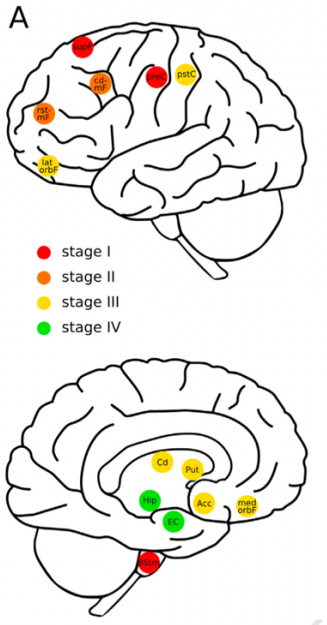

Figure 5: TDP-43 stages in ALS [35].

Usually, in the two PPA variants, atrophy initially appears either in left hemisphere and progressively spreads. Literature showed that earliest changes in svPPA patients include GM loss in the inferior temporal and fusiform gyri, then progression of disease leads to involvement of the middle and inferior frontal gyri, posterior temporal gyrus, inferior parietal lobule and occipital lobe [36-38]. Whereas in nfvPPA patients, peak

of atrophy was identified in the left supplementary motor area, and then spread in the inter-connected zones, involving left frontal operculum, premotor area, anterior insula, and superior and transverse temporal gyri [36, 38, 39].

1.1.5 Clinical presentation and diagnostic criteria

bvFTD

bvFTD is the most common clinical variant and accounts approximately for 70% of all FTD cases [7]. Overall, bvFTD patients are mainly characterized by abnormal behavior and personality changes. Presence of three of the following clinical features leading to possible bvFTD diagnosis: disinhibition, apathy, loss of sympathy/empathy, perseverative, stereotyped and compulsive/ritualistic behavior and hyperorality/dietary changes [40, 41]. Probable bvFTD diagnosis is met when patients demonstrate functional decline and imaging reflects the typical bvFTD frontotemporal degeneration. To conclude, diagnosis of definite bvFTD is reached when histopathological evidence of disease or a known pathogenetic mutation are detected.

PPA

PPA patients are characterized by language deficits leading to significant functional impairment. In the semantic variant of PPA (svPPA), patients progressively lose their capacity of understanding word meanings and coming up with words. The non-fluent/agrammatic variant of PPA (nfvPPA) instead is a condition in which speech becomes agrammatic and effortful. Indeed, the two core features for svPPA diagnosis impaired confrontation naming and poor single-world comprehension [42]. Whereas, nfvPPA patients core features for clinical diagnosis are agrammatism in language production and effortful, halting speech with inconsistent speech sound errors and distortions (apraxia of speech). At least three of the following symptoms are required for svPPA clinical diagnosis: impaired object knowledge, particularly for low-frequency or low-familiarity items, surface dyslexia or dysgraphia, spared repetition and speech production (grammar and motor speech). For clinical diagnosis of nfvPPA two of the following must be present: impaired comprehension of syntactically complex sentences, spared single-word comprehension and spared object knowledge.

Finally, svPPA or nfvPPA diagnosis is definite when the clinical diagnosis is associated to histopathologic changes or to the presence of a pathogenic mutation.

MND

MND encompasses several phenotypes, such as amyotrophic lateral sclerosis (ALS), primary lateral sclerosis (PLS) and progressive muscular atrophy (PMA). ALS is the most common clinical presentation of MND and is characterized by the progressive degeneration of both upper motor neurons (UMN) and lower motor neurons (LMN), whereas PLS is characterized by the progressive degeneration of upper motor neuron only and PMA by degeneration of lower motor neuron [43]. ALS is characterized by muscle weakness, limiting movements, causing muscle atrophy resulting in fatal respiratory failure [44]. Usually, ALS onset is localized in the cerebral cortex and spinal cord, with asymmetric, painless weakness in a limb (spinal onset). But in the 20% of the case, ALS is characterized by bulbar onset, with dysarthria, dysphagia and tongue fasciculations [45]. ALS is diagnosed with the revised El Escorial criteria [46], which requires the presence of clinical, electrophysiological or neuropathologic evidence of LMN degeneration and clinical evidence of UMN degeneration, the progression of signs within a region or to other regions. Such evidence has to be combined with the absence of other diseases or neuroimaging evidence able to explain the observed signs. If there are UMN and LMN signals in the bulbar area and at least two spinal regions, or if there are UMN and LMN signs in three spinal regions, it is considered to be clinically definitive ALS. UMN and LMN signals in at least two locations are required for the diagnosis of clinically probable ALS, with some UMN signs necessarily rostral to the LMN signs [46]. PMA is characterized by clinical and electrophysiological evidence of progressive LMN involvement without evidence of UMN disease. PMA is usually asymmetric and distal and/or proximal onset can occur [47]. PLS is characterized by UMN disease, without LMN involvement after 4 years from disease onset [48].

1.1.6 Treatments

Nowadays, there is no disease-modifying treatment for FTLD. Currently, non-pharmacological therapies are involved to support both patients and caregiver. It is necessary to develop strategies able to maintain behavior, cognition and language in

FTLD patients [49]. Through caregiver training, with the aim to implement communication with the patient, not only it is improved the stress of the caregiver, but also patients' behavior problems are attenuated [50-52]. Moreover, reducing noise and stimulation, or simplifying social situations, could be helpful in management for behavioral disorders (Barton C. et al, 2016). The future of FTLD treatment is to find an approach to target the pathologic tau protein and prevent its prion-like spread [53]. Possible therapeutic strategies include tau aggregation inhibitors, microtubule-stabilizing drugs and immunotherapy [53-55].

1.2 Magnetic Resonance Imaging (MRI)

MRI technology and its clinical usage was firstly introduced in 1971 by Paul Lauterbur and today represents a powerful tools used in hospitals and clinics for medical diagnosis, staging and follow-up of diseases [56]. Therefore, in 1971 it was already demonstrated by Raymond Damadian that the nuclear magnetic signal from pathological and non-pathological tissues differed, thus motivating scientists to consider magnetic resonance for the detection of disease [57].

MRI allowed to overcome limits introduced by other imaging diagnostic methods like Computed Tomography (CT) and x-rays, which uses ionizing radiation harmful to the patients. Indeed, MRI scanners use magnetic field and radio waves and for this reason it imposes very little risk of the tissue damage when frequent imaging is required for diagnosis. Furthermore, with MRI scan it is possible to better differentiate and contrast soft tissue instead of CT that is commonly used to identify bone lesions or pulmonary metastases. To distinguish different tissues is necessary to change MRI sequences parameters obtaining the desired contrast of similar tissues. Chemical substances could be injected intravenously to enhance contrast of some tissues, such as gadolinium which improves the visibility of inflammations, tumors, and blood vessels. Obviously, not all patients tolerate the injection of this type of substances.

Despite the advantages introduced by MRI, there are some situations where it is not recommended to use MRI, such as patients with ferromagnetic metals in the body (i.e., pacemakers), and claustrophobic patients who might not be able to tolerate the exam in the closed MRI scanner [58]. Moreover, due to the long-time duration of MRI scans, patients often move during the exam, and this causes artifacts in the images.

However, with the advent of advanced MRI techniques, numerous investigations for even early diagnosis of many pathologies were identified. In order to describe the structural and functional changes caused by neurodegenerative disorders, MRI is becoming an increasingly significant tool in the research of these pathologies. Advanced MRI techniques might have the potential to identify the distinctive features of each neurodegenerative disease and support both the diagnostic process and the tracking of disease progression [59].

1.2.1 MRI basic principle

MRI is based on the interaction between electromagnetic field and biological tissues. Indeed, any moving particle with a certain mass turns around its axis generating an angular momentum called spin (I). The latter defines energy levels allowed to the particle as:

$$\text{energy levels} = 2I + 1 \qquad (1)$$

For example, hydrogen atom has a spin equal to ½, hence it is allowed spinning around its axis in two towards, clockwise and counterclockwise. A charged particle that spins around its axis induces a magnetic moment (equation 2) which is colinear with the direction of the spin axis.

$$\mu = \gamma \cdot I \qquad (2)$$

where γ is the gyromagnetic ratio of the nucleus, which is a constant, characteristic of a given nucleus and it indicates the amount of magnetic field produced by the particle at each rotation. The strength of this magnetic moment is a property of the type of nucleus and determines the detection sensitivity of MR (Table 1). ^{1}H nuclei possess the strongest magnetic moment, which, together with the high biological abundance of hydrogen in human body, makes it the nucleus of choice for MR imaging.

Table 1: MRI properties of some nuclei.

Nucleus	Spin	*Relative* sensitivity	Gyromagnetic ratio $\frac{\gamma}{2}$ [MHz/T]
^{1}H	$\frac{1}{2}$	1.000	42.58
^{13}C	$\frac{1}{2}$	0.016	10.71
^{19}F	$\frac{1}{2}$	0.870	40.05
^{31}P	$\frac{1}{2}$	0.093	11.26

The magnetic moment of each nucleus has its own module but random direction. Indeed, in a volume of human tissue in a rest condition the vector addition of all magnetic moment will be statistically equal to zero. Vector addition of magnetic moments is called ‘magnetization’ (M) which represents the total tissue charge. When

a constant magnetic field (B0, frequency = 0 Hz) is applied, the protons inside the tissue no longer have a random direction but the external field establishes a preferential direction (figure 6). Therefore, protons are aligned to the external field and the vector addition is no longer equal to zero, but matter has been magnetized. However, magnetic moments of protons in the tissue in this situation may adopt one of two possible orientations: alignment parallel (spin-up orientation) or anti-parallel (spin-down orientation) to B0.

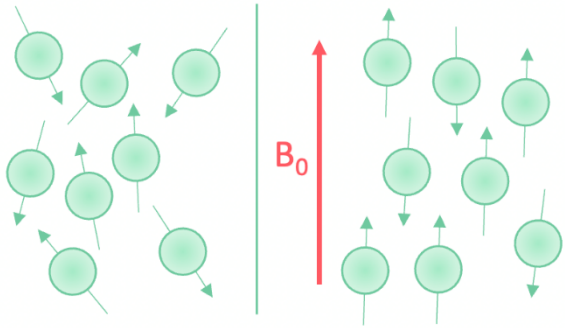

Figure 6: On the left protons are in the rest condition, on the right an external static field is applied, and protons follow a preferential direction aligned to B_0

However, the ratio between spin-up and spin-down protons depends on Boltzmann statistic:

$$\frac{n\uparrow}{n\downarrow} = e^{\frac{\Delta E}{KT}} \approx 1 + \frac{\Delta E}{KT} \qquad (3)$$

- $n\uparrow$: numbers of protons with spin-up orientation
- $n\downarrow$: numbers of protons with spin-down orientation
- ΔE : energy difference between the two orientations
- K : Boltzmann constant
- T : Absolute temperature

The series development of the exponential in equation 3 clearly shows how the relationship between the two orientations is always greater than 1. Indeed, alignment parallel to B0 is the lower energy orientation and is thus preferred and more protons

follow this orientation, while the anti-parallel alignment is the higher energy state. The ratio in equation 3 depends also on temperature and since the ratio must remain constant it is necessary to perform MRI exams in a thermostat environment.

The difference between the total number of parallel and anti-parallel nuclei, is known as the bulk net magnetization M. Net magnetization increases with the increase of B_0; indeed, it is very important that the external field has an intense value to be able to drive all the protons and typically has values greater than or equal to 1 T.

Protons are not perfectly parallel to B_0 because they process around B0 (figure 7). The speed of precession depends on the strength of B_0 and is called the "Larmor frequency". The Larmor frequency is obtained by the Larmor relationship:

$$\omega = \gamma \cdot B_0 \tag{4}$$

where ω is 2π times the precessional frequency, B_0 is the external magnetic field, and γ is the gyromagnetic ratio.

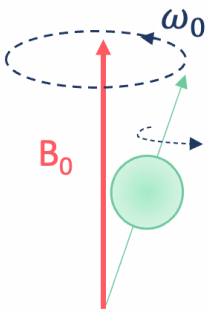

Figure 7: Precessional motion of proton around B0 axis with Larmor angular velocity ω_0

All ^{1}H nuclei possess the same gyromagnetic ratio, but it is necessary that the magnetic field is constant in time and in space so that all protons feel the same external field and all of them have the same Larmor frequency. Since magnetic vectors are not parallel to B_0, they have also a transverse component but because of the precession motion of nuclei the vector addition of transverse component is equal to zero. Therefore, magnetization vector has only the component along the static magnetic field and its intensity is not enough to measure it and create an image. To amplify the reaction of tissues other external energy is provided to tissue and the condition of resonance is reached. Specifically, a radio frequency (RF) pulse at the system frequency, which is

the Larmor frequency, is applied to the particles. System goes in resonance when RF excitation is given, and this conceptually means that it absorbs energy from an external source and the particles that were in a low energy state change their quantum state assuming the highest energy state. The external pulse is an external field B_1 whose frequency is in the RF band; resonance frequency is given by eq. 4 in which for example B_0=1T and $\gamma = 42\ \frac{MHz}{T}$ and the precession frequency is more about 42MHz (RF band). The resonance phenomenon is very selective, in fact according to the frequency it is possible to induce resonance only in particular nuclei, for example in the case of MRI in ^{1}H.

As shown in figure 8A, B_0 is a static field along z axis and B_1 has only transversal component and lies on the xy plane. M is the magnetization vector and has longitudinal and transversal components. When B_1 is applied, protons in spin-up orientation acquire energy and achieve the spin-down orientation; the longitudinal component tends to flag because protons with spin-down and spin-up orientation become equal, and M lies in the xy plane. After a while, the number of protons with spin-down orientation increase and M aligns the -z direction. Hence, M rotates around z axis and in the longitudinal direction as shown in figure 8B and 8C. The deflection angle α is called flip-angle and it is calculated as follow:

$$\alpha = \gamma B_1 t \tag{5}$$

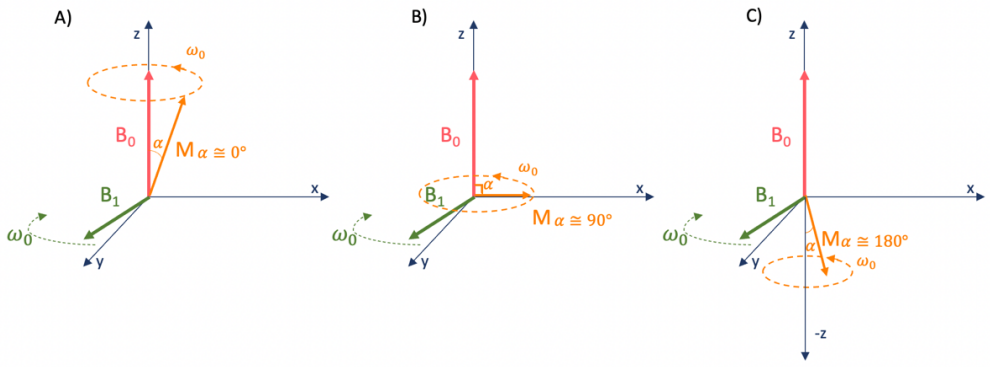

Figure 8: A) Representation of interaction between B_0, B_1 and M. C) Deflection angle = 90° D) Deflection angle = 180°

In MRI pulse of interest have flip-angle equal to 90° or 180°. The net magnetization vector relaxes back to its B0 orientation when the RF pulse is stopped, and the particles return to the equilibrium ratio; the excess energy is released in the form of an electromagnetic signal called free induction decay (FID). Various tissues in human body emit FID in different time, in fact what is important in MRI is signal timing. The two types of energy decay are called spin-lattice decay (with time constant T1, which reflects the time the longitudinal component of the magnetization vector takes to return to the initial condition) and spin–spin decay (with time constant T2, which reflects the time the transversal component of the magnetization vector takes to return to the initial condition). Moreover, magnetic field inhomogeneity, the differences in magnetic susceptibility among various tissues or materials, chemical shift, and gradients applied for spatial encoding have a characteristic time of dephasing called T2* [60]. T2* is shorter than T2 as shown in Figure 9.

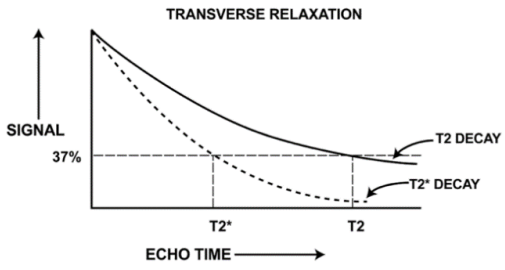

Figure 9: Graph shows T2 and T2 relaxation curves [60].*

The duration of these time constants, ranging from a few milliseconds to seconds, is determined by the type of particles and the substance in the area. More precisely, the spin-lattice relaxation time occurs because of an exchange of energy between the spin system and the lattice (tissue surrounding the protons), whereas the spin-spin decay causes the transfer of energy between spins.

Different tissues have different T_1 and T_2 and different sequences of excitation pulses are used to emphasize one relaxation time at the expense of the other; an MR image is a conversion of time constants in shades of gray. The MRI signal evolution over time follows the following expression:

$$A = A_0 e^{\frac{-t}{T_1}} e^{\frac{-t}{T_2}} \quad (6)$$

- t: timing
- T1: spin-lattice decay
- T2: spin-spin decay
- A0: amplitude a t=0

The amount of time between successive pulse sequences applied to the same slice is called the Repetition Time (TR). The time between the delivery of the RF pulse and the receipt of the echo signal is referred to as Time Echo (TE). T1-weighted and T2-weighted scans are the most common MRI sequences in which, T1 and T2 properties of tissues determine the contrast and brightness of the images. For example, in tissues with shorter T1 values signal back quickly to initial condition producing brighter images, whereas tissues with longer T1 values appear darker because signal decays more slowly (Figure 10).

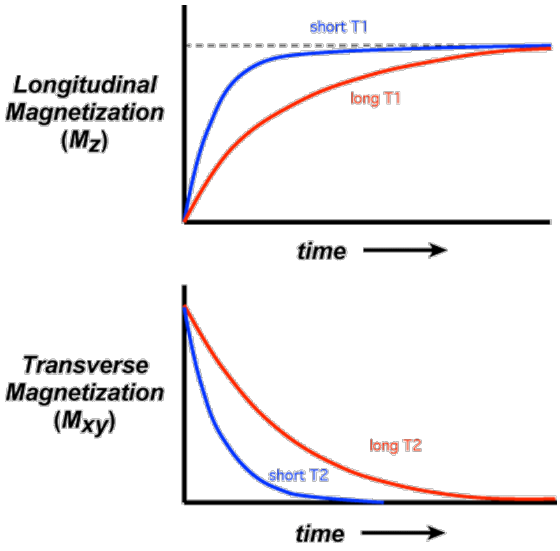

Figure 10: Graph shows T1 and T2 relaxations decays. (Figure taken from: https://mriquestions.com/opposite-effects-uarrt1-uarrt2.html)

T1-weighted images are produced by using short TE and TR times relative to T2-weighted images, having longer TE and TR times. In T1-weighted images, fluids are

very dark, water-based tissues are mid-grey and fat-based tissues are very bright. In T2-weighted images, fluids have the highest intensity, and water and fat-based tissues are mid-gray. Fluid Attenuated Inversion Recovery (FLAIR) is another commonly used sequence, which is like a T2-weighted image, but with longer TE and TR times. As a result, abnormalities remain bright and normal CSF is attenuated and appears dark. This sequence has a high sensitivity to pathology and provides a good differentiation between CSF and abnormalities.

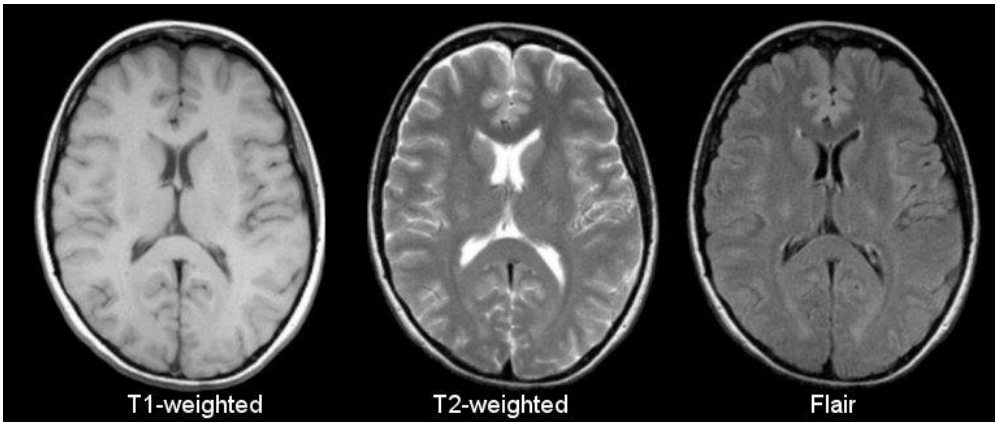

Figure 11: Comparison between different sequences (figure taken from https://case.edu/med/neurology/NR/MRI%20Basics.htm)

Table 2: Comparison between different tissues appearance in T1, T2, and Flair images (table taken from https://case.edu/med/neurology/NR/MRI%20Basics.htm)

Tissue	T1-Weighted	T2-Weighted	Flair
CSF	Dark	Bright	Dark
White matter	Light	Dark Gray	Dark Gray
Cortex	Gray	Light Gray	Light Gray
Fat (within bone marrow)	Bright	Light	Light
Inflammation (infection, demyelination)	Dark	Bright	Bright

1.2.1 T1-weighted images

T1-weighted images provides good contrast between GM (dark gray) and WM (lighter gray) tissues, while CSF is void of signal (black). The longitudinal relaxation of a tissue's net magnetization vector is necessary to produce a T1-weighted image. Fat quickly realigns its longitudinal magnetization with the Bo, and it therefore appears bright on a T1-weighted image. In contrast, water has less transverse magnetization following an RF pulse because its longitudinal magnetization realignment is significantly slower, appearing darker.

T1-weighted MRI is used to investigate GM structural changes (atrophy) by using contrast between GM and WM provided. Indeed, it is possible to parcellate GM and then obtain the volume of each ROI. A detailed description of this procedure will be discussed in paragraph 3.3.2.

1.2.2 Diffusion-weighted MRI

Diffusion is the random thermal motion of molecules. The displacement distribution of molecules in a fluid depends on the time over which diffusion is being quantified, the fluid's viscosity, the temperature, any concentration gradients that might be present, and physical barriers the molecules might encounter. The diffusion of water molecules is used to generate contrast in MR images. The motion of a water molecule that is free to diffuse obeys to the Einstein's law:

$$< r^2 > = 6 \cdot D \cdot t \qquad (7)$$

- $< r^2 >$: mean square displacement
- D : diffusion coefficient (mm^2/s)
- t : diffusion time

Since water molecules do not move freely because there are some biological barriers, in different tissue there is a different D and trough MRI it is possible to measure this value. This diffusion coefficient is often called Apparent Diffusion Coefficient (ADC). Water molecule diffusion patterns can therefore reveal microscopic details about tissue architecture, either normal or in a diseased state. In diffusion weighted imaging (DWI), the intensity of each image element (voxel) reflects the best estimate of the rate of water diffusion at that location. Because water is largely dependent on its cellular environment for mobility and is driven by thermal agitation, the DWI is based on the notion that certain findings could signify pathologic alteration.

An MR experiment by Stejskal and Tanner [61], showed the possibility of detection and quantification of water diffusion in vivo. Applying a symmetric pair of diffusion-sensitizing (bipolar) gradients around the 180° refocusing pulse, they adapted a

standard T2-weighted spin-echo sequence which is the basis of many DWI sequences. Indeed, applying a pair of gradient pulses along the same directional axis sensitizes the MR signal to the water diffusion process. The first gradient pulse causes molecules to acquire phase shifts, the second gradient pulse will cancel the phase shifts by rephasing the (stationary) spins. The refocusing will not be perfect for protons that have moved during the time interval between the pulses, and the signal measured by the MRI machine is reduced (signal loss) (Figure 12). The higher the degree of random motion (e.g. within CSF), the more MR signal loss, conversely the lower the degree of random motion (e.g. in GM or WM), the lower the MR signal loss.

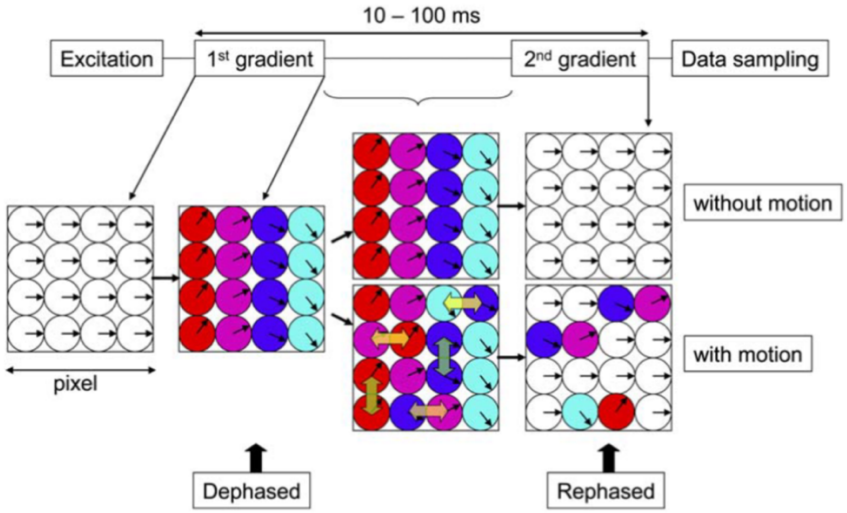

Figure 12: Phases of the signal at each site are shown by the vectors in the circles. Signal loss results from the second gradient's inability to properly refocus the phases if water molecules migrate between the two gradient applications [62].

This signal is given by Stejskal-Tanner equation:

$$S = S_0 e^{-bD} \quad (8)$$

where S0 is the signal strength without any diffusion weighting. The sensitivity of the diffusion sequence to water motion can be varied by changing the gradient amplitude, the duration of the sensitizing gradients, and the time between the gradient pair.

The diffusion-weighting factor is named b-value and the value is given in units of s/mm^2 by:

$$b=\gamma\, G\, \delta\, (\Delta-\delta/3)$$

(9)

where γ is the gyromagnetic ratio, G is the strength of the diffusion-sensitizing gradients, δ is the duration of the gradient pulse, and Δ is the time interval between these gradients. A higher b-value is achieved by increasing the gradient amplitude and duration and by widening the interval between the gradient lobes and this will cause a higher signal loss (darker image). A diffusion-weighted image with a b-value of zero is similar to a typical T2-weighted image; CSF is bright and grey matter is dark. As b-values increased, there is greater signal loss in specific parts of the brain, primarily within the WM. This is because the water within those WM tracts is diffusing primarily along the direction of the tract, and the image that is generated shows correspondingly lower signal. Higher b-values also make the image more susceptible to image artifacts such as movement and magnetic currents called 'eddies' that cause distortions.
However, to extract information about the value of apparent diffusion two signals are needed:

$$\begin{cases} S_1 = S_0 e^{-b_1 D} \\ S_2 = S_0 e^{-b_2 D} \end{cases}$$

(10)

Thus, starting with a Non Diffusion-Weighted image (S1), created for example by setting b1 = 0, and a Diffusion-Weighted image (S2), we can perform the ratio and obtain the apparent diffusion coefficient as follow:

$$\frac{S_2}{S_1} = e^{-(b_2-b_1)D}$$

(11)

$$D = \frac{-\ln\left(\frac{S_2}{S_1}\right)}{b_2 - b_1}$$

(12)

Diffusion measurements are needed along multiple axes and are needed at least a couple of measurements in each direction. The more are the measurements the better is in term of reconstruction of diffusivity in the space.

1.2.2.1 Diffusion Tensor Imaging

In WM, water diffusion is relatively unimpeded in the direction parallel to the fiber orientation. On the other hand, in directions that are perpendicular to the fibers, water diffusion is severely constrained. Thus, the diffusion in fibrous tissues is anisotropic [63]. The diffusion anisotropy is described by a diffusion tensor, whose eigenvalues represent the apparent diffusivity along an axis and eigenvector represent the direction of the gradients that were applied along an axis. Brain has preferred directions that correspond to WM tracts, which are thick bundles of myelinated neurons that connect both nearby and distant parts of the brain. The major diffusion eigenvector (direction of greatest diffusivity) is assumed to be parallel to the tract orientation in regions of homogeneous WM.

Diffusion tensor is a symmetric matrix and the smallest one is represented as follow:

$$D\begin{pmatrix} D_{xx} & D_{xy} & D_{xz} \\ D_{xy} & D_{yy} & D_{yz} \\ D_{xz} & D_{yz} & D_{zz} \end{pmatrix} \quad (13)$$

Where D_{xx}, D_{yy}, D_{zz} represent diffusion calculated along principal directions (x, y and z), whereas off-diagonal terms represent correlations between principal axis. Once tensor's eigenvalues and eigenvector are calculated, diffusion principal directions are obtained.

As shown in figure 13 and 14 each voxel is fitted by a tensor, so represented by a combination of eigenvectors and eigenvalues, that allows for the generation of different types of diffusion maps, such as fractional anisotropy (FA) and mean diffusivity maps. FA measures the degree of diffusion anisotropy by using a measurement of difference among the three eigenvalues calculated as follow:

$$FA = \sqrt{\frac{1}{2}}\frac{\sqrt{(\lambda_1 - \lambda_2)^2 + (\lambda_2 - \lambda_3)^2 + (\lambda_3 - \lambda_1)^2}}{\sqrt{\lambda_1^2 + \lambda_2^2 + \lambda_3^2}} \quad (14)$$

If diffusion is isotropic (λ1 = λ2 = λ3), measure becomes 0, whereas values near to 1 indicate high diffusion anisotropy.

MD describes the overall diffusion and is calculated as follow:

$$Mean\ Diffusivity = \frac{\lambda_1 + \lambda_2 + \lambda_3}{3} \quad (15)$$

Higher is MD value higher is the brain damage. Indeed, when a degeneration occurs in structurally organized tissue, such as WM tracts, MD increases and FA decreases because of a loss of the directionality of diffusion.

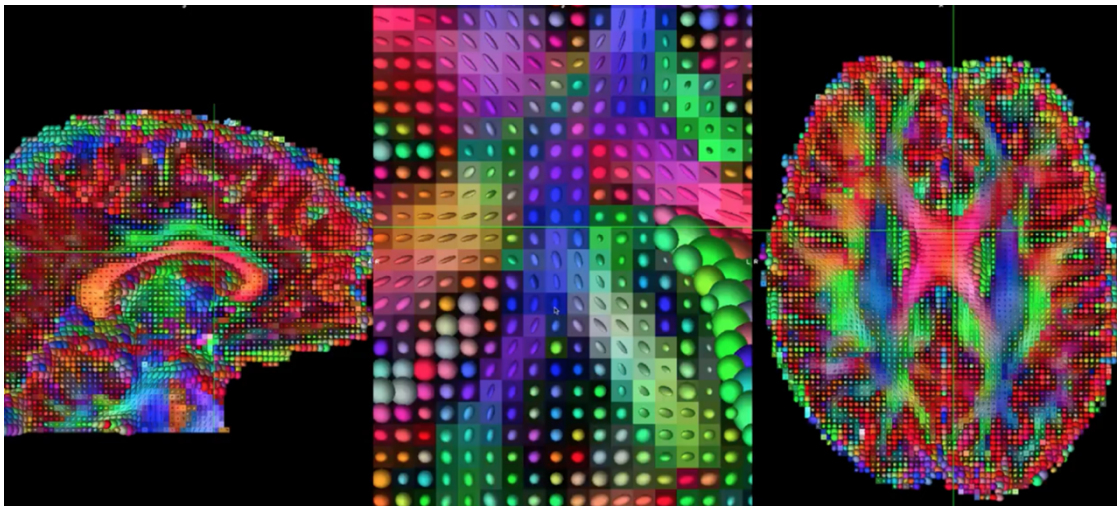

Figure 13: visualization of tensor within each voxel [64]

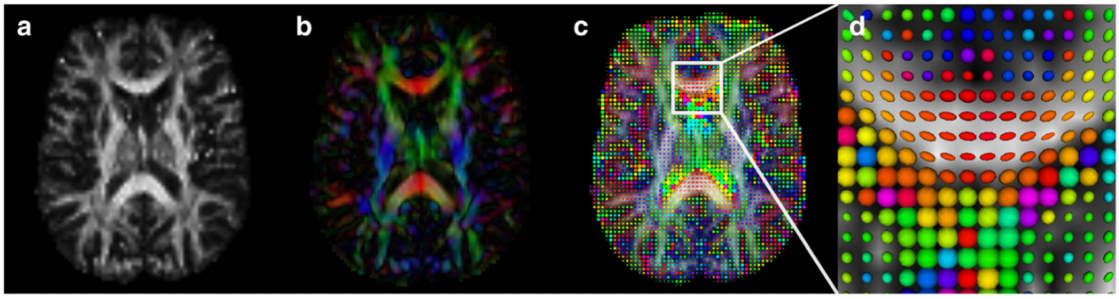

Figure 14: FA maps and diffusion tensor visualization. a) FA map, where higher is the FA value brighter is the pixel b blue colors represent fibers running along the right-left, anterior-posterior, and inferior-superior axes, respectively. c Diffusion tensor representation [65].

1.2.2.2 Tractography

The directional information of DW-MRI can be used to select and follow neural tracts through a process called tractography [66], whose steps will be described in detail in paragraph 3.3.3.4. An overview of the main cerebral tracts is reported in figure 15.

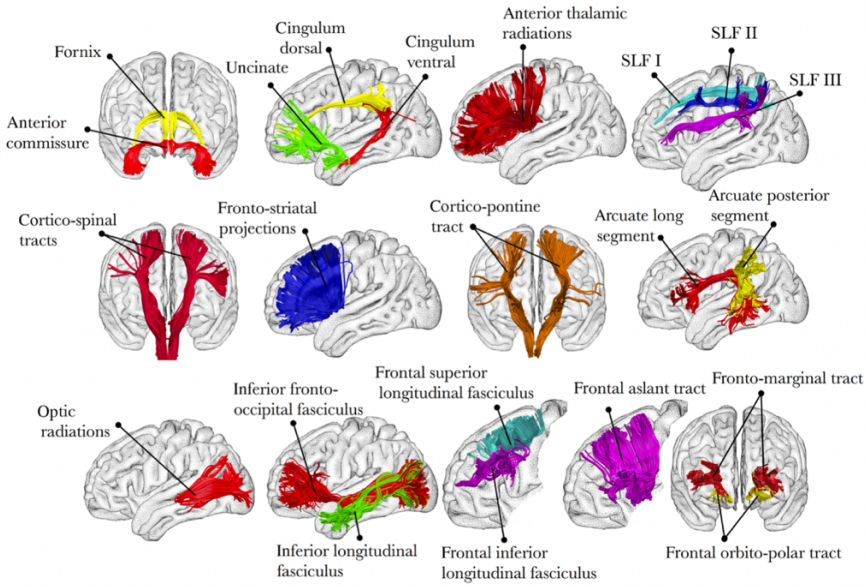

Figure 15: Brain neural tracts. [67]

Tractography is used to enable quantitative analysis of the structural connectivity in the brain's [68], which accuracy depends on the tractography algorithm used and model of the diffusion signal on which it is based [69]. A summary of tractography approach is presented in Table 3 [69].

Table 3: Summary of three major dimensions along which most tractography algorithms can be classified [69].

Dimension	Approach	Description
Probabilistic vs deterministic	Deterministic	Propagates single trajectories in accordance with principal direction of water diffusion (e.g., Basser et al., 2000). Does not estimate the spatial uncertainty of the trajectory.
	Probabilistic	Samples a direction distribution function at each step to determine the propagation direction. Allows estimation of a probability density of the most likely location of the tract, and thus its spatial uncertainty (e.g., Behrens et al., 2003).
Local vs global	Locally greedy	Trajectories propagate incrementally using a near-sighted, voxel-by-voxel approach (Basser et al., 2000; Behrens et al., 2003). Can be affected by noisy voxels.
	Globally optimal	Estimates the globally optimal path between two regions, typically by representing voxel-wise water diffusion as a connected graph and finding the shortest between seed and target voxels (Itturria-Medina et al., 2007; Itturia-Medina et al., 2008; Zalesky, 2008; Zalesky and Fornito, 2009). More robust to noise.
Single vs multi-direction	Single direction	The direction of water diffusion in each voxel is represented using the primary eignvector of the diffusion tensor (Basser et al., 2000; Behrens et al., 2003). Does not distinguish crossing fibers.
	Multi-direction	The direction of water diffusion in each voxel is represented using an orientation distribution function (Behrens et al., 2007; Tournier et al., 2004). Allows resolution of crossing fibers, but requires quality, high angular resolution data.

1.2.2.3 Neurite orientation dispersion and density imaging

Neurite orientation dispersion and density imaging (NODDI) provides an improvement of diffusion MRI through a model which separates the signal arising

from three different tissue compartments: intra-neurite water, extra-neurite water and cerebrospinal fluid (CSF) [70]. Different tissues respond differently to different b-values (multi-shell approach), and this can be used to better characterize cell compartments and fiber orientation. Figure 16 shows how signals basis form differ in the different combinations of tissue and b-value.

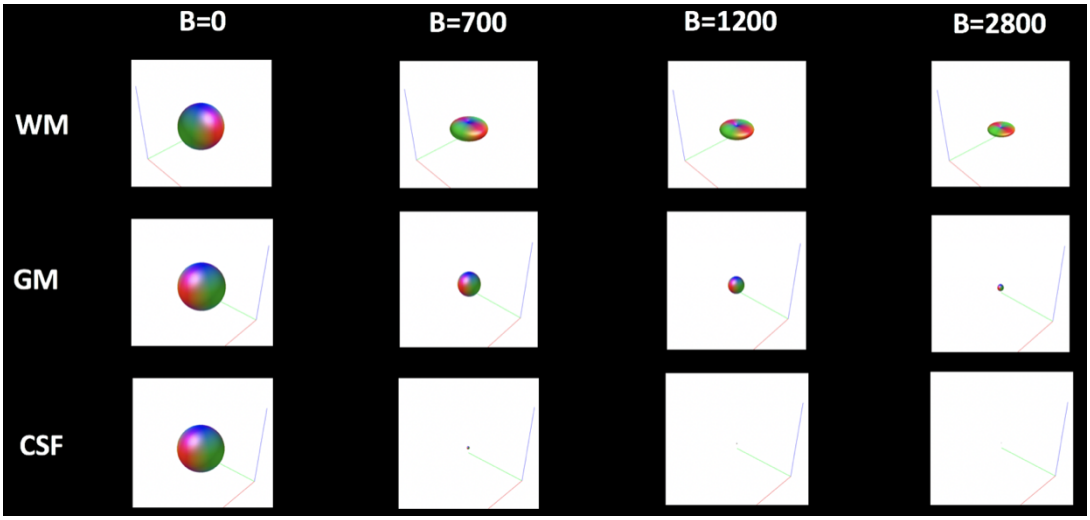

Figure 16: Basis function for different combination of tissue type and b-value [64]

The intra-neurite compartment considers the tissue component of axons and dendrites, the extra-neurite compartment considers the tissue component of cell bodies and glial cells, and the non-tissue comportment (e.g., CSF) accounts for free water (Figure 17) [71].

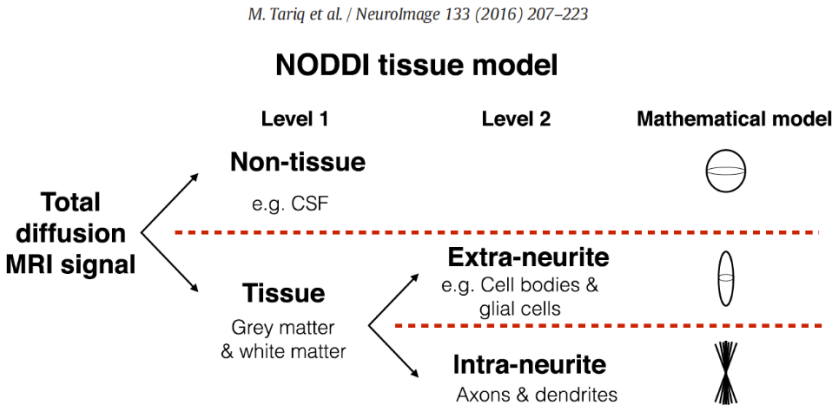

Figure 17: The non- tissue compartment that contains is modeled using isotropic Gaussian diffusion. The region around the neurites is described by an anisotropic diffusion model, whereas the intra-neurite compartment represents the neurites as orientationally dispersed sticks [71].

NODDI allows to estimate neuronal density through intra-cellular volume fraction (ICVF), orientation dispersion through orientation dispersion index (ODI) calculated in the extra-cellular environment and the CSF volume fraction through isotropic water diffusion (ISO) index [71, 72]. Particularly, a loss of directionality in WM tracts should cause a decrease of ICVF measure and an increase of ODI measure. The latter reflects an augmented fibers orientation dispersion in WM structure. NODDI specificity might lead to an improvement of biomarker detection in neurodegenerative diseases at a microstructural level. DTI presents limitations when an image voxel contains fiber populations with more than one dominant orientation. FA values are lower in such areas because of a lower directionality of diffusion on the voxel-scale, which makes the interpretation of FA less straightforward [73]. Furthermore, MD in diffusion tensor MRI is affected by crossing fibers, in fact MD values are lower in complex fiber architecture than in single fiber voxels. Overall, FA and MD are non-specific [74]. Indeed, DTI signal is affected also by biophysical characteristics of neuronal cells [75]. Recent developments in diffusion MRI, like NODDI, have addressed some of the limitations of standard DTI and advanced capacity to characterize tissue microstructure.

1.2.3 Functional MRI

Changes in neuronal activity cause a rapidly increased need of oxygen in active neuron. Consequently, blood flow increases in order to meet the larger demand for oxygen [76]. The change in tissue perfusion causes a net increase of oxyhemoglobin (O2Hb) and a consequent concentration reduction of deoxyhemoglobin (HHb). This hemodynamic response is measured by Blood Oxygen Level Dependent (BOLD) signal.

In 1990 Seiji Ogawa and colleagues showed that hemoglobin shows different magnetic properties: diamagnetic when oxygenated but paramagnetic when deoxygenated [77]. Since the quality of MRI signal is strongly influenced by the uniformity of the magnetic field experienced by water molecules, when HHb interferes with the MRI magnetic field a loss of signal occurs [78]. Brain tissue areas, where the activity occurs, presents lower concentration of HHb, therefore MRI signal decays less rapidly and brighter than areas with higher concentrarion of HHb[76]. Hence, areas with high concentration of O2Hb generate brighter images than areas with HHb that are darker

in the image. This form of fMRI is known also as BOLD imaging that represents the standard technique to generate functional MR images. Moreover, the MRI sequence sensible to the changes in the magnetic field is T2*-weighted, so it is used in functional MRI.

Since fMRI scanning is very fast, it is possible to create a series of images of the brain based on the amount of oxy-Hb, so to track brain activity over time. A typical whole-brain acquisition takes 5 to 10 minutes and provides 100 to 300 volumes. As mentioned above, during brain activity HHB concentration decreases, because blood flow exceeds the brain's metabolic need. As a result, BOLD signal increases after a stimulus as shown in Figure 18.

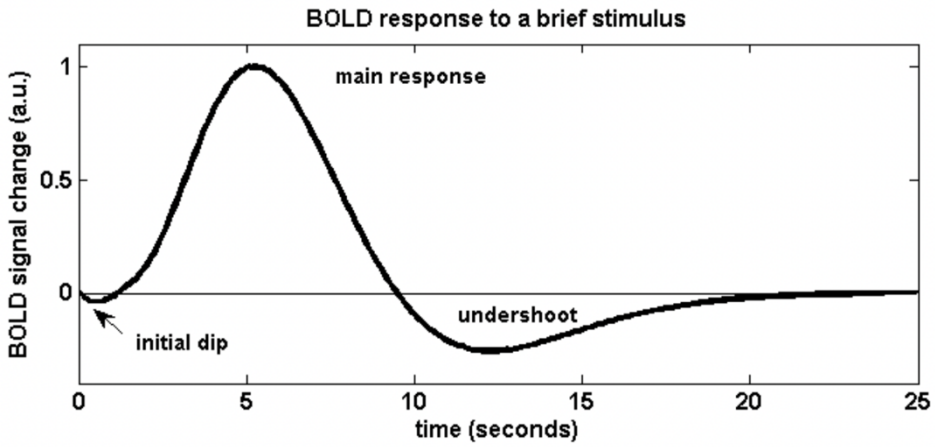

Figure 18: Schematic of the BOLD hemodynamic response to a brief stimulus at time zero. [79].

However, Biswal et al in 1995 observed that the spontaneous low frequency ($f<0.1$ Hz) BOLD signal fluctuations could reveal functional connectivity between brain areas [80]. Hence, Resting-State fMRI (RS-fMRI) measures BOLD signal fluctuations in the absence of a task or stimulus [81]. Correlations between mean signal from different brain areas are then performed to value the connectivity between them; it is assumed that over time of acquisition (~5-10 minutes), the functional connections are not changing.

There are several reasons to use RS-fMRI instead of task-related fMRI for clinical analysis [82]:

- Task-based fMRI is more focused on specific brain areas, while RS-fMRI might show a more general view of brain activations
- RS-fMRI presents low signal to noise ratio relative to task-based fMRI
- Many patients with cognitive or physical impairment are not able to perform tasks accurately in the fMRI scanner
- Task learning could occur in longitudinal studies, giving ambiguous results

RS-fMRI has allowed to identify networks linking regions that are anatomically separate yet functionally intertwined. In FTLD, the most studied networks are those related to cognition: default mode network (DMN), salience network (SN), speech and language network (SPN), executive network (EXN) [83]. DMN involves the posterior cingulate cortex, parietal cortex and medial temporal lobe and it was introduced as a "control state" or "baseline state" in functional connectivity by Marcus E. Raichle in 2001 [84]. Moreover, the DMN is particularly vulnerable to atrophy and deposition of the amyloid protein, in fact, activity changes in DMN in aging and dementia are observed [85]. SN, composed of the anterior cingulate, insula, striatum, and amygdala [86], has a role in focusing attention on meaningful sensory information. Whereas SPN is a structure responsible for speech and langauge production that comprises the left inferior frontal, dorsal insular, supplementary motor and inferior parietal regions [87]. Lastly, EXN involves frontoparietal areas and it is responsible for high- level cognitive functions such as planning, decision making, and the control of attention and working memory [83].

1.2.4 Imaging in FTLD

Standard neuroimaging studies analyze structural and functional activity in specific brain regions, as reported in the following paragraph.

T1-Weighted Imaging

Several studies investigated GM loss distribution in FTLD through T1-weighted imaging (Figure 19). bvFTD is generally characterized by frontotemporal atrophy, involving in particular the prefrontal cortex and anterior temporal regions, insula,

anterior cingulate [37, 88, 89]. Subcortical structures like the striatum, thalamus, hypothalamus and brainstem are often involved [90, 91].

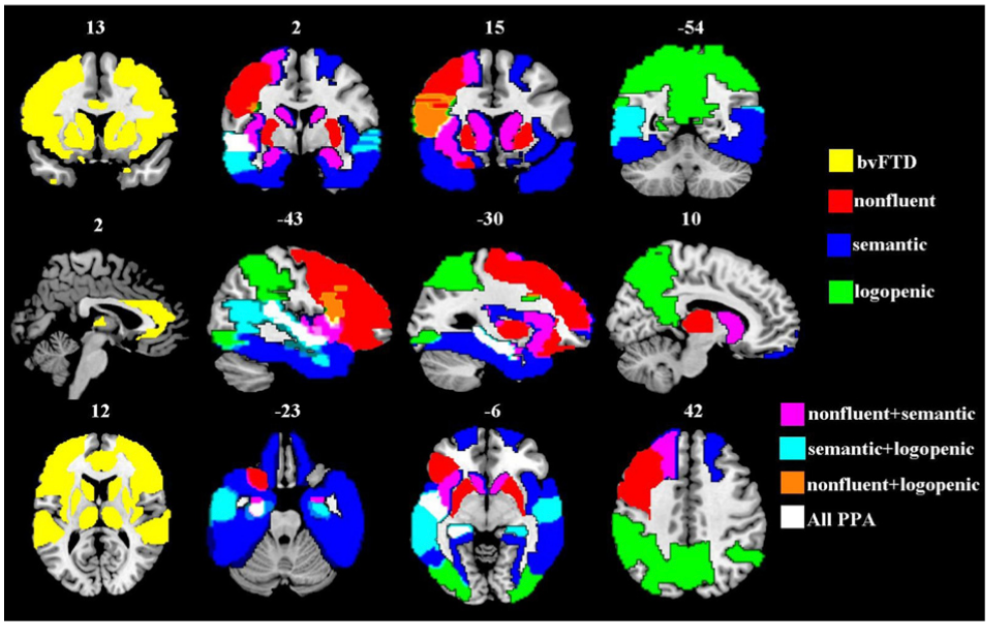

Figure 19: Patterns of GM atrophy in patients with bvFTD and each PPA variant [92].

Whereas bvFTD is associated with wide ranging and bilateral alterations in the frontotemporal areas, PPA cases show more focal and asymmetric structural changes [93]. Indeed, svPPA is associated with commonly left-side antero-inferior temporal lobe atrophy and nfvPPA with predominantly left-sided inferior frontal and insula involvement [1]. Moreover, in svPPA and nfvPPA patients, loss of grey matter in the earliest pathology stage predominantly involves one hemisphere and spreads to the contralateral hemisphere over time [94].

Recent studies investigated grey matter loss in MND patients using T1-weighted imaging. However, there are conflicting results, some studies showed focal atrophy in motor and premotor cortex in ALS patients [95, 96], other highlighted widespread frontotemporal atrophy [97, 98], or even no significant atrophy [99]. These differences might be due to different MRI processing.

Diffusion Weighted Imaging

WM abnormalities have been studied in FTLD spectrum with DTI. Microstructural alterations in WM differentiated FTLD syndromes. In particular, bvFTD patients showed structural changes in frontal lobes and in tracts travelling though the temporal

lobe. svPPA patients presented WM alterations predominantly in the left temporal tract, whereas in nfvPPA patients WM damage was more focus in left inferior frontal lobe, left orbitofrontal, insula, and supplemental motor area [100-103]. However, longitudinal studies demonstrated that WM damage spreads over time also in the right hemisphere (in particular in the uncinate fasciculus) in svPPA patients and in posterior brain areas in bvFTD patients [104, 105].

FTLD is commonly associated to TAU and TDP-43 proteinopathy, and it was tested if FTLD-TAU and FTLD-TDP could be differentiated by DTI technique. Interesting results were obtained in 2013 by McMillan Corey T. and colleagues, who showed how FTLD-TAU presented greater WM burden (decreased FA in bilateral superior longitudinal fasciculus) in contrast to FTLD-TDP [106].

ALS is the most common phenotype of MND, hence the most studied. Most significant alterations (decreased FA and increased MD) in ALS patients were showed in corticospinal tract [107]. Other studies put their effort in evaluating microstructural integrity in patients with PLS; widespread damage in motor areas were found [108]. More recently, ALS has been also characterized with NODDI. NODDI detected more neurodegenerative areas compared to DTI measure. In ALS patients, neurite density index decreased in the corticospinal tracts, corpus callosum and precentral gyrus [70]. Overall, studies have pointed out how WM lesions are more involved in FTLD pathologies in comparison to GM loss, supporting the progression of "prion-like" pathology through the WM connection, that characterize the spectrum [109].

Functional MRI

RS-fMRI might be a sensitive biomarker even for early stage of FTLD syndromes [110]. Studies showed decreased functional activity in the SN and an augmented functional activity in the DMN, in particular in the prefrontal cortex, in bvFTD patients [111, 112]. Hyperconnectivity in DMN in bvFTD patients could represent a maladaptive behavior associated with dementia [113]. svPPA patients are characterized by decreased functional activity in the ventral semantic network, involving anterior middle temporal and angular gyri, and by increased connectivity between the inferior frontal gyrus and the superior portion of the angular gyrus, which suggested possible adaptive changes [114]. Whereas in nfvPPA patients functional

changes involve the left inferior frontal gyrus and the left supplementary motor area, inferior and superior parietal gyri between both hemispheres, and striatum with the supplementary motor area in both hemispheres [115]. Interestingly, some studies had shown how functional strength can represent a biomarker predicting the evolution of atrophy in svPPA and nfvPPA syndromes [39, 116]. Concerning MND, ALS patients often show decreased functional activity in the premotor cortex and DMN [117-119]. ALS patients also show increased activity in inferior frontal lobe, sensorimotor cortex, sensorimotor lobe, parahippocampal gyrus and cerebellum as a compensatory process in early stage of disease, followed by functional failure with pathology spreading [119, 120].

1.3 Connectome and Graph Analysis

1.3.1 Connectomics

Understanding brain function by investigating connectivity of human brain might lead to improve comprehension of the development of neurodegenerative disorders. Brain function does not depend solely on the properties of individual regions, but rather emerges from interaction patterns across the entire network. Indeed, as at a microscopic level the neurons form a network, also at the macroscopic level the WM neuronal bundles interconnect brain areas allowing functional communication among them [121]. It is possible to analyze this macroscopic brain communication thanks to the advent of new advanced neuroimaging techniques, which allowed to reconstruct anatomical and functional connectivity across regions of the human brain [122]. For example, through diffusion MRI tractography, WM streamlines that connect anatomically distinct regions of GM are mapped, and it allows the construction of structural connectome. Moreover, with the use of fMRI it was possible to analyze the functional connectivity between brain areas, measuring the spontaneous co-activation of them in a resting situation [123]. Overall, structural and functional connectivity are closely related; structural connectivity is highly informative of functional connectivity [124].

Hence, through the connectome, it is possible to mathematically represent human brain with a graph, where the nodes are modeled by the GM areas and the edges represent the structural or functional connections between brain regions (Figure 20). Brain network might be also represented by a two-dimensional connectivity matrix wherein the rows and columns correspond to specific brain GM regions, and the value stored within each element of the matrix is the computed connectivity “strength” between those regions corresponding to that row and column [125].

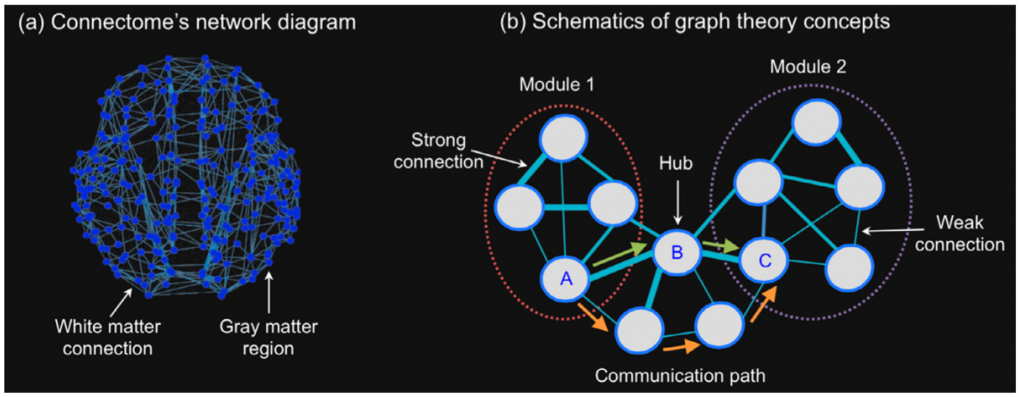

Figure 20: Graph theory basic principles representation [68]

The brain connectivity matrix was firstly introduced in 2005 by Olaf Sporns and Patric Hagmann as the human "Connectome" [125, 126]. Connectome is an advanced MRI technique that might provide new insight on how brain architecture enables functional communication between brain areas and into how brain function is affected if the structural substrate is disrupted [125].

The human connectome includes all the neuronal connections and is considered as a single entity, highlighting the power of the connectivity architecture that allows brain neuronal communication capacity and computational power [126].

Extracting specific features from connectome (for example graph analysis measures) and through specific analyses it is possible to find useful biomarker to help prediction of pathologies and to prevent prion-like spread. Therefore, it is possible to mathematically model "prion-like" transynaptic transmission of disease agents like misfolded tau and beta amyloid by a diffusive mechanism mediated by the brain's connectivity network [127].

1.3.2 Graph analysis

Graph Theory is a branch of mathematics that defines structures that are used to represent system's elements and model the interactions and relations between them [128]. Network models describe brain as a set of nodes and edges (Figure 20a, Figure 21a,b). Indeed, to construct a brain graph it is necessary to choose connectivity measures that will serve as the network edges and to find an appropriate way to parcellate the brain into regions that will serve as the network nodes. Graph network are usually represented as connectivity matrix.

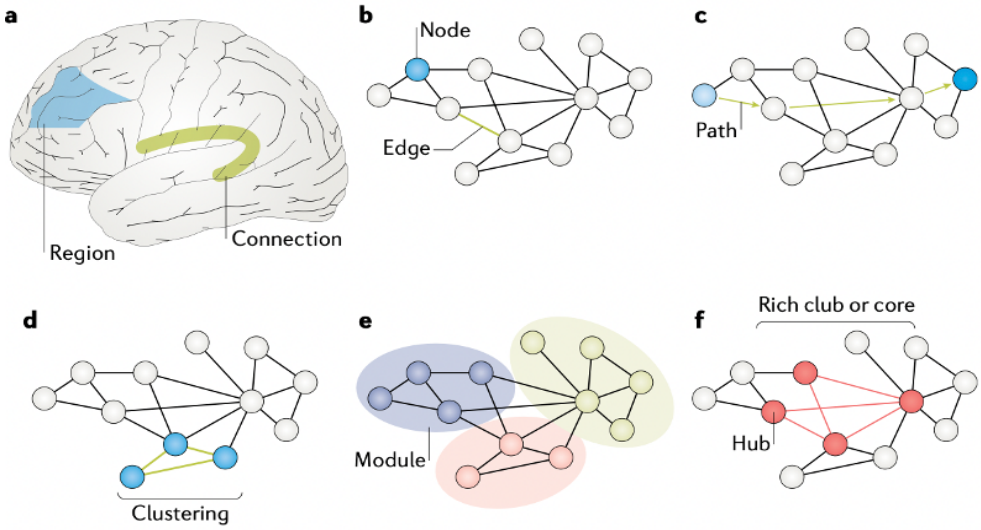

Figure 21: a,b: brain graph construction. c,d,e,f: illustration of some graph theory concepts [122].

In particular, as mentioned above, diffusion MRI tractography allows to map WM tracts. Before, it is necessary to define a parcellation of the brain so that streamlines (WM pathways) between the segmented GM nodes of the brain are selected. For each structural connection, the level of microstructural integrity is measured extracting the mean FA or MD and NODDI measures (ICVF, ODI). Each of these measures are inserted within the structural connectivity matrix. Structural connectome allows to study the integrity of the fibers and tracts that is of particular interest in the assessment of neurodegeneration. Indeed, FA and ICVF structural measures the directionality of water flow instead of ODI and MD that measure water diffusion in brain tracts.

Whereas, functional connectivity matrices contain the Pearson correlation coefficient between the mean RS-fMRI time-series obtained averaging over the time-series of all voxels contained in a brain region. Negative correlation coefficients, whose meaning is uncertain, will be set to 0 to mark these brain regions as unconnected [129]. Functional connectivity is proposed to characterize the relationship between the neuronal activation patterns of physically distinct brain regions in the context of functional neuroimaging [123]. Indeed, different types of neurodegeneration differentially affect functional networks of the brain. To sum up, an illustration of structural and functional connectome reconstruction is shown in Figure 22.

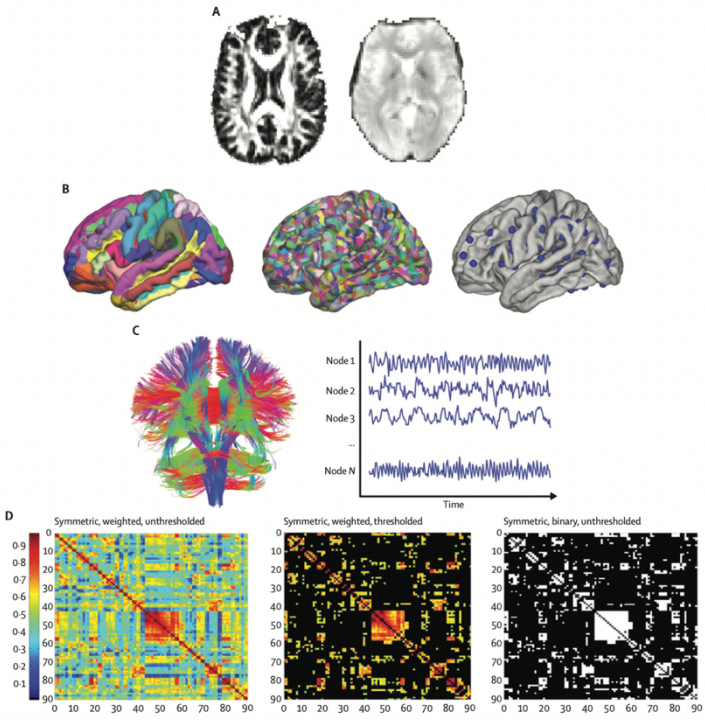

Figure 22: A: DTI image on the left and RS-fMRI on the right. B: brain parcellation and definition of brain nodes. C: MRI tractography on the left and time-series extracted from RS-fMRI images on the right. D: Connectivity matrix. Typically, a threshold is used to discriminate spurious connections from real connections [121].

A graph may be classified as undirected or directed depending on whether links have directions or not as we can see in figure 23 [130].

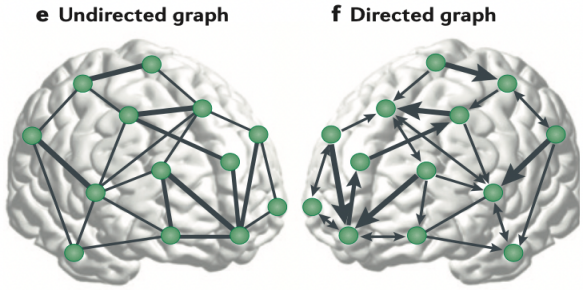

Figure 23: directed connectivity on the right, undirected on the left [131]

Furthermore, some graph metrics can be obtained and used to describe properties of network's architecture. Hereafter, the most common graph metrics will be listed. Degree centrality, perhaps the most popular metric employed in brain network, equates the number of connections at each node to that node's centrality:

$$DC(i) = \sum_{i=1}^{220} A(i,:)$$

(16)

Centrality is a concept in graph theory used to classify nodes as central, or more important, within a system [132]. Nodes with high degrees and an overall central position in a network's topological organization are often described as hubs [121]. Martijn P. van den Heuvel and Olaf Sporns in 2011 showed that brain hubs form a so-called "rich club," with a propensity for high-degree nodes to be more densely interconnected than nodes with a lower degree [133]. Another measure of centrality is eigenvector centrality that defines the importance of a node by the connection originating from that node [132]. The eigenvector centrality of node i is equivalent to the ith element in the eigenvector corresponding to the largest eigenvalue of the connectome. If the neighbors of a node have higher centrality it plays a more crucial role in mediating information transfers in the network. Additionally, path length (mean distance) is the minimum number of edges that must be traversed to go from one node to another and it is inversely related to the global efficiency of a network for the transfer of information between nodes by multiple parallel paths. Another metrics is the sum node weights, that is the sum of strength weight of each node

$$SN(i) = \sum_{i=1}^{220} c(i,:)$$

(17)

where c(i,:) selects the i-row of the connectome.

Nevertheless, the archetypal brain network has a short path length (associated with high global efficiency of information transfer), high clustering coefficient, otherwise high local efficiency of information transfer and robustness [134]. Indeed, this organization of the brain network was called "small-world" [135] architecture (Figure 24) and it is a result of a natural process to satisfy the balance between the speed of information transfer and a reduced energy consumption [130].

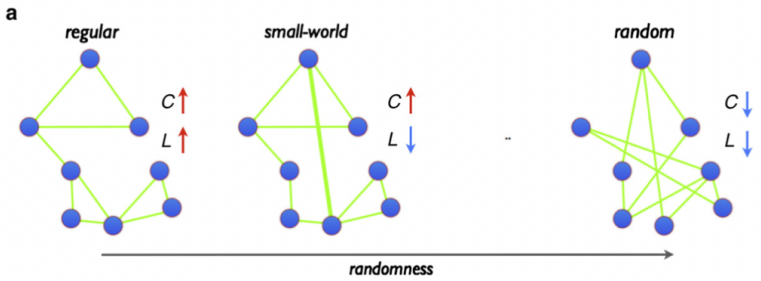

Figure 24: Regular network has high clustering coefficient (C) and high path length (L). Small-worls architecture has high C and low L. Random network has low C and L. [123]

It is also possible to identify modules within a network, which contain several densely interconnected nodes, with few connections between nodes in different modules as showed in Figure 21e [134]. Modularity can be seen as the measure of functional brain network organization [136].

Network Based Statistics

The graph model offers a perfect framework for identifying the structural or functional connections underlying a given effect or contrast of interest, such as a group difference in a case-control comparison, a difference brought on by shifting task requirements in a functional paradigm, or a correlation with a particular clinical measure. To identify these connections, a statistical approach called Network Based Statistic (NBS) is used [137]. This new approach is a method to control the family-wise error (FWE) rate when mass-univariate testing is performed at every connection comprising the graph. The purpose of NBS procedure is to show that impaired connections forming a connected component in a network have a greater possibility of indicating a true alteration than single connections that do not form a connected component [137]. A detailed description of NBS procedure can be found at paragraph 3.1.5.

1.3.3 Structural and functional connectome in FTLD

Structural connectivity

Several studies analyze structural connectome in FTLD spectrum. In particular, bvFTD selectively affects connectome showing decreased FA and increased MD predominantly in frontal, temporal and parietal lobe and insula compared to controls (Figure 25) [138]. These findings suggested selective alterations of the structural brain network in bvFTD patients.

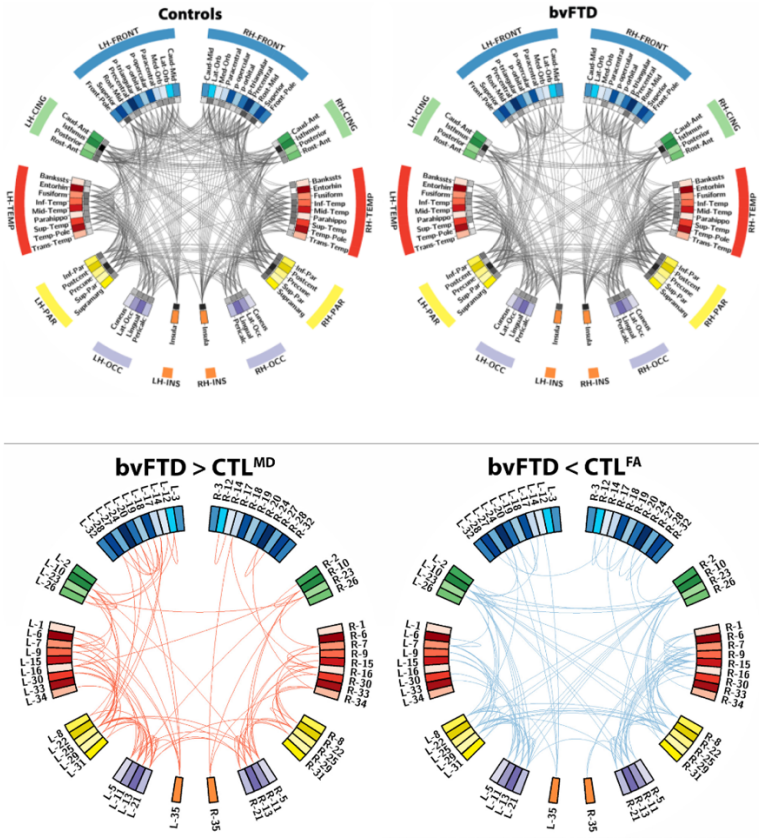

Figure 25: Above, connectograms of the average pattern of healthy controls and bvFTD. Below, groups differences (MD and FA) [138].

Moreover, other studies using graph theory revealed a decreased global efficiency and clustering coefficient in frontal and temporal lobe and posterior brain regions (i.e., precuneus and cuneus), which suggests a generally decreased capacity for information transfer (Figure 26) [139-141]. Moreover, it was demonstrated that bvFTD atrophy was associated with structural connectome alterations providing a possible advice to the typical atrophy pattern of bvFTD patients [142].

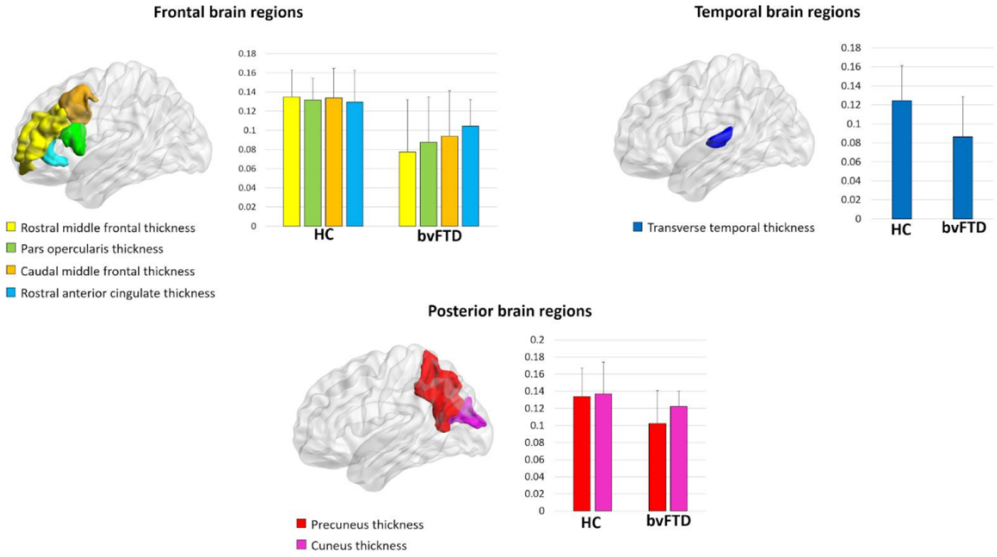

Figure 26: regions where behavioral variant bvFTD patients' local efficiency is lower compared to healthy controls [139].

In recent years, few study have analyzed structural connectome in PPA. Particularly, svPPA have shown asymmetrical alterations in MD and FA connectivity (augmented FA and decreased MD compared to healthy controls) in temporal and occipital lobes with the left side significantly different from controls [143]. Also nfvPPA patients showed changes with a major predominance in the left hemisphere, but predominantly involving frontal inferior regions, premotor and motor cortex, and the basal ganglia [143]. In these abovementioned regions, also graph metrics were found altered in these two PPA variants (Figure 27), offering more evidence that the neurodegenerative mechanisms underlying each PPA variant are associated with specific patterns of structural network changes [144].

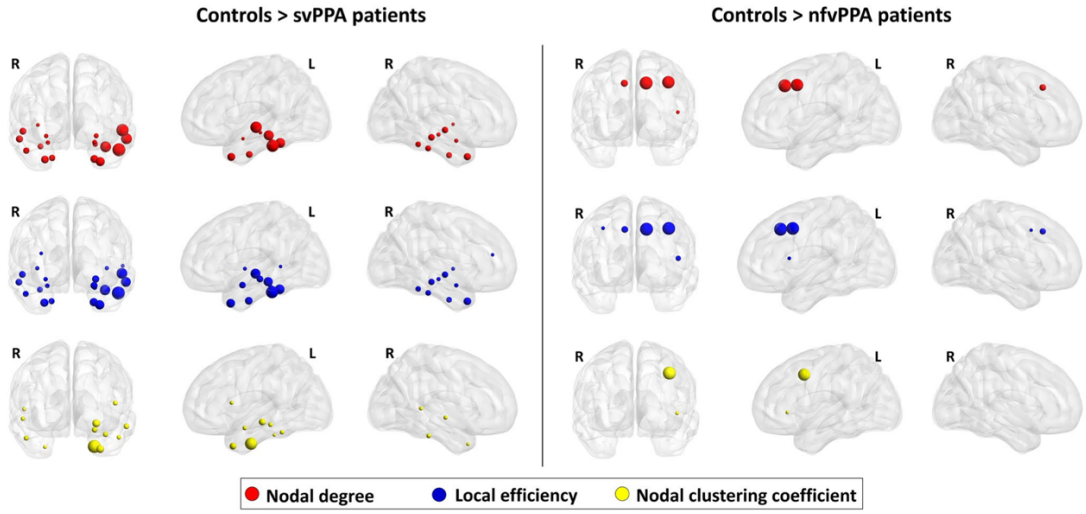

Figure 27: cortical and subcortical brain regions showing reduced local properties between patients and svPPA patients on the left, and between patients and nfvPPA patients on the right [144].

Graph analysis and connectomics were also applied to investigate ALS. When evaluating the structural brain network in ALS, the most recurrent finding is reduced WM connectivity (FA) within the principal motor connections and frontal cortex (Figure 28) [145, 146]. Additionally, overall efficiency and clustering coefficient were found to be decreased in ALS patients [146]. Moreover, connectome and graph analysis were helpful in distinguishing MND variants. Patients with PLS present alterations in sensorimotor network relative to ALS group and patients with ALS showed decreased FA relative to PMA patients within the sensorimotor network including precentral and postcentral gyri and frontal network [147]. These studies showed widespread motor and extramotor network degeneration in MND patients, suggesting that graph analysis and connectomics might represent a powerful approach to detect upper motor neuron degeneration and delivering potential prognostic markers.

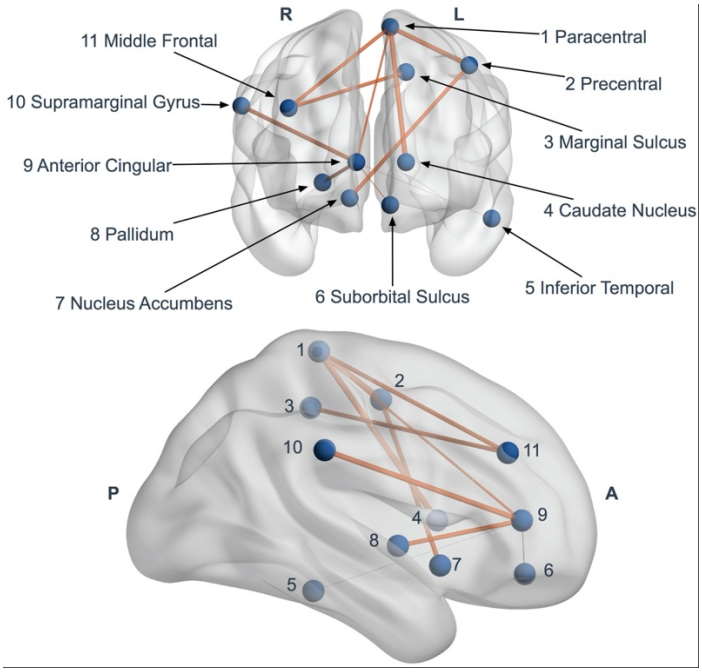

Figure 28: Edge with significant reduced FA in ALS patients relative to healthy controls found through NBS analysis [145].

Functional connectivity

It was investigated in previous studies, through connectome and graph analysis, whether brain functional network connectivity is disrupted in FTLD patients. Overall, using NBS, decreased functional strength in bvFTD patients compared to controls was found, including frontotemporal pathways and connections to the motor cortex and basal ganglia (Figure 29, 30a) [115, 148]. These findings helped to characterize disease-specific patterns of functional network topology and connectivity alterations [148]. Moreover, bvFTD selectively affected network centrality in the fronto-temporo-insular network and subcortical regions, which is associated with high-level social and executive profile [115, 149].

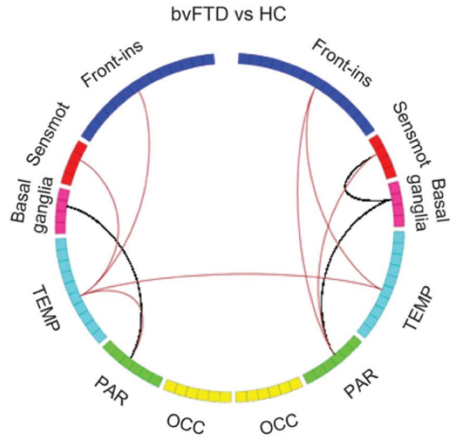

Figure 29: Red connections: bvFTD<HC; Black connections: bvFTD>HC [148]

Considering the results with linguistic variants, NBS showed more functional alterations in nfvPPA than svPPA compared to healthy controls, as shown in Figure 30b,c [115]. In particular, svPPA patients were characterized by a significantly lower mean network degree, clustering coefficient, and global efficiency, longer characteristic path length compared with controls, with deficits occurring majorly in the left inferior and ventral temporal region and the occipital area [150]. Whereas nfvPPA patients showed lower clustering coefficient and efficiency within the left inferior frontal, dorsal insular and supplementary motor area [39]. Hence, functional connectivity might be a useful to identify biomarkers to distinguish also PPA variants.

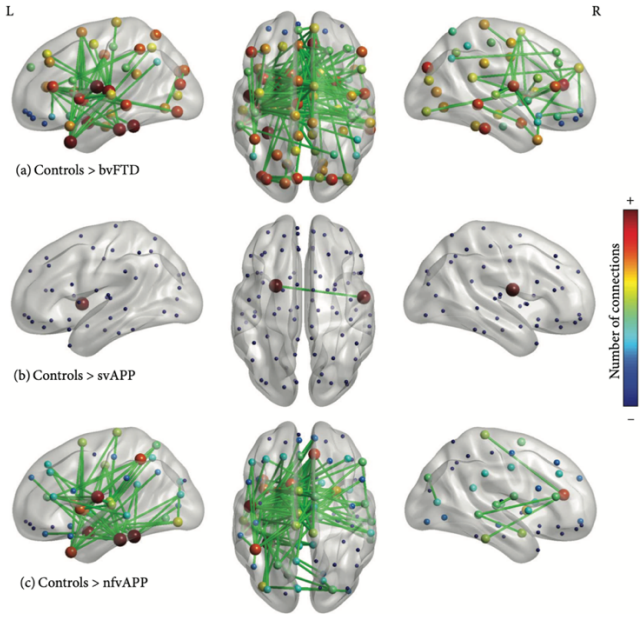

Figure 30: NBS results between controls and bvFTD, svPPA and nfvPPA patients from Reyes et al, 2018 [115].

Few studies applied connectomics and graph analysis to the assessment of functional

alterations in ALS patients using RS-fMRI [151, 152], demonstrating connectivity alterations involving frontal, temporal and occipital regions.

Network-based analysis were applied in order to differentiate MND phenotypes, highlighting that PLS patients are characterized by widespread functional alterations encompassing both motor and extra-motor areas with a pattern resembling classic ALS patients (Figure 31) [108, 147, 153]. These findings suggested that graph analysis and connectomics might be a powerful technique for identifying extramotor brain alterations, upper motor neuron degeneration, and network remodeling related to these diseases. By contrast, PMA patients did not show any functional damages relative to healthy controls [147, 154, 155].

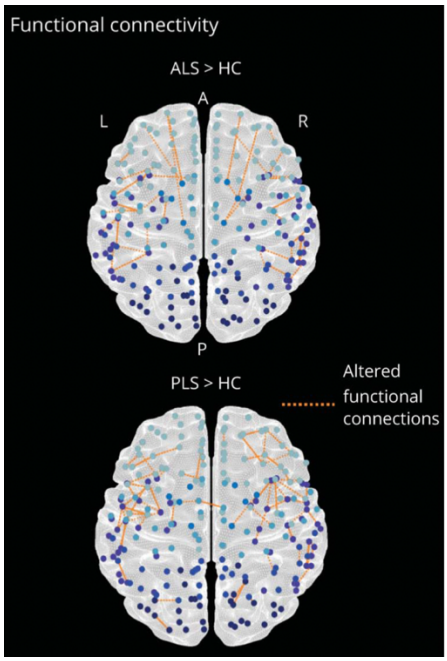

Figure 31: NBS showed functional alteration in ALS and PLS patients compared to HC [147].

1.3.4 Network Diffusion Model

Network diffusion model (NDM) is used to mathematically model the pathology diffusion process across the human brain connectome. NDM was firstly introduced by Ashish Raj (2012) who generalizes the "network heat equation" [156]. Indeed, the basic concepts of network diffusive mechanism were taken from the network heat equation, which can be expressed as the progression of any pathology from a high concentration to a lower concentration until the equilibrium state is accomplished [157]. The principal aim of NDM was to explore selective vulnerability and

pathological diseases progression through healthy connectome, using a quantitative network-based model of pathology spread originating from a single regional seed.

NDM was initially used to mathematically model the transmission of misfolded proteins (like tau and amyloid) that spreads along neuronal pathways, by a diffusive mechanism mediated by brain's connectivity network [127]. It was found that NDM has predictability on longitudinal progression of atrophy from baseline pattern [127, 158]. The computation of NDM's differential equation involves an eigenvector decomposition and it was found that each eigenmode represents spatial patterns that have a strong resemblance to known patterns of different dementias [127].

NDM was also applied on FDG-PET images to predict hypometabolism evolution in Alzheimer's Disease (AD) because of the pathology progression [158]. Afterwards, NDM was modified by introducing a directional connectome, where the direction of the connections is considered. This method was applied on a rare disorder called progressive supranuclear palsy (PSP) and it explains PSP topography more accurately than non-directional transmission [159]. Moreover, NDM was also used to estimate the seed region where the pathology starts to spread in Parkinson's Disease (PD) [160]. Finally, in other study, NDM was applied to find the disconnections in Huntington's Disease (HD) as WM connections connecting the nodes with the highest amount of disease factors [157]. Anyway, the implementation of NDM to cross-sectional structural connectome data is a valuable tool to predict future atrophy patterns and pathology spreading in neurodegenerative disorders, simulating the hypothetical spread of disease-causing proteinopathy into the network. Furthermore, studies mentioned above suggested that NDM has greater predictability on longitudinal progression starting from the baseline pattern of each patient. To conclude, the model was then validated though a correlation between MRI longitudinal data and data predicted by NDM. A schematic illustration of the model is given in figure 32.

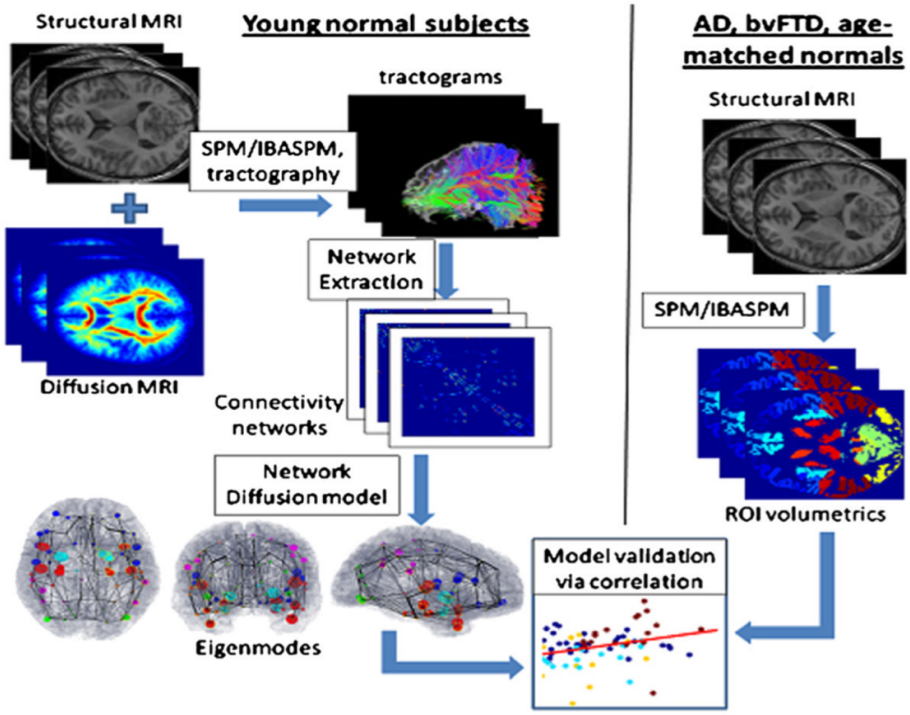

Figure 32: NDM procedure [127]

CHAPTER 2: AIM OF THE PROJECT

FTLD is a heterogeneous group of disorders characterized by the deposition of abnormal proteins inclusions in neurons and glial cells [41, 161]. Starting from disease-specific epicenters of neurodegeneration, misfolded proteins follow a "prion-like" trans-synaptic transmission along neuronal pathways, which can be studied in whole-brain structural and functional connectivity networks [127]. Moreover, MRI connectomics has demonstrated a close relationship between strength in brain connectivity and the magnitude of atrophy accumulation in FTLD disorders, supporting a network-based spread model of pathology [39, 87, 116]. In addition, pathology is more likely to spread to brain regions with functional proximity to the epicenters [162]; indeed, it is reasonable to model pathologies spreading both on structural and functional connectome.

Therefore, MRI advanced techniques will be used to explore the role of network alterations in different FTLD diseases, by identifying changes in structural and functional connectivity at a brain-system level through the so-called 'connectome' analysis, mapping patterns of different pathologies. Finally, tracking the initial event and predicting the way of misfolding protein propagation across the brain would be valuable for identifying therapeutic targets that could be modulated before potentially irreversible spreading of protein pathology and neuron loss [163]. Identification of network biomarkers was the main objective of this study in order to use them in intervention trials, preventing or delaying the progression of the disease.

To sum up, the main aims of this thesis are:

- To investigate alterations in structural and functional brain network in FTLD spectrum using connectome-analysis.
- To predict spatiotemporal patterns of neurodegeneration exploring the relationship between selective network vulnerability and longitudinal pathological progression in patients of the FTLD spectrum, using Network Diffusion Model.

CHAPTER 3: MATERIAL AND METHODS

3.1 Participants

A total of 176 patients with a suspected diagnosis of disorders of the FTLD spectrum were referred between October 2009 and April 2021 to the Neurology Unit of San Raffaele Hospital in Milan to perform a complete neurological work-up, as well as a neuropsychological evaluation and an MRI scan on a 3 Tesla scanner. MRI protocol included longitudinal T1-weighted MRI and single multi-shell diffusion MRI resting-state and functional MRI (RS fMRI) sequences. Longitudinal follow-up were performed at 6, 12, 18 and 24 months (Table 4). Patients received a clinical diagnosis of FTD according to either bvFTD [164], nfvPPA or svPPA [42] clinical criteria, and were therefore evaluated for inclusion in the present study. Genetic patients (i.e., 6 *C9orf72*, 9 *GRN*, 1 *MAPT* and 1 *TREM2*) were identified and excluded from the present study. Patients, who demonstrated a high cerebrovascular burden or motion artifacts on MRI, were not included in the study. Patients with at least 2 follow-up visits were included. After the screening process, the final baseline cohort included 74 sporadic FTLD patients, divided into 34 bvFTD, 11 nfvPPA, 11 svPPA and 18 MND patients (Table 5).

Table 4: number of patients included in this study at each time-point. Abbreviations: behavioral-variant frontotemporal dementia (bvFTD), semantic variant primary progressive aphasia (svPPA), nonfluent variant primary progressive aphasia (nfvPPA), motor neuron disease (MND), healthy controls (HC)

	Baseline	6 Months	12 Months	18 Months	24 Months
bvFTD	34	29	20	15	10
nfvPPA	11	11	4	-	-
svPPA	11	11	8	-	-
MND	18	18	-	-	-
TOT	74	69	32	15	10

Forty-eight healthy controls (HC), comparable for age and sex with patients, were recruited among spouses of patients and by word of mouth. The controls were included if the following criteria were satisfied: normal neurological assessment; Mini-Mental State Examination (MMSE) [165] score ≥28; no family history of neurodegenerative diseases. All subjects were screened using the following exclusion criteria: significant systemic, psychiatric, or neurological diseases; any (other) major neurological,

psychiatric, or neurologic disorders; and other causes of focal or diffuse brain damage, including lacunae and extensive cerebrovascular disorders at routine MRI.
In addition to FTLD patients and age-matched healthy controls (age range between 41 and 85 years), 48 young healthy controls (HC-young, i.e., age range between 20 and 30 years) were also recruited at IRCCS San Raffaele Hospital. Young healthy subjects represented a "gold-standard" healthy connectome for the construction of functional and structural connectivity matrices, and in order to implement NDM.

*Table 5: Values are reported as means ± standard deviations (min – max). The threshold of statistical significance was set at p<0.05. p values refer to ANOVA models followed by post-hoc, Bonferroni-corrected comparisons or Pearson's chi square, as appropriate. * = statistically significant difference with HC; # = statistically significant difference with bvFTD; $ = statistically significant difference with MND. Abbreviations: CDR = Clinical Dementia Rating; CDR-sb = Clinical Dementia Rating sum of boxes; MMSE = Mini-Mental State Examination; ALSFRS = Amyotrophic Lateral Sclerosis Functional Rating Scale; behavioral-variant frontotemporal dementia (bvFTD); semantic variant primary progressive aphasia (svPPA); nonfluent variant primary progressive aphasia (nfvPPA); motor neuron disease (MND); healthy controls (HC).*

	HC	**HC young**	**svPPA**	**nfvPPA**	**bvFTD**	**MND**
N	48	48	11	11	34	18
Age [years]	61.98±8.56 (40.14-76.73)	25.05±2.79 (20-31)	66.40±9.02 (49.91±75.31)	70.16±7.9 (53.83-78.98)*	64.52±9.01 (36.50-79.76)	62.88±9.02 (44-78)
Sex [women/men]	35/13#	22/26	7/4#	9/2#	24/10	9/9
Education [years]	12.08±3.92 (5-20)	12.01±3.75 (5-20)	12.36±3.85 (5-17)	9.51±4.59 (5-18)	11,03±3.36 (3-19)	11.61±3.57 (6-18)
Disease duration [months]	-	-	36.99±19.40 (11.50-60.88)	22.03±5.83 (16,56-21.11)	42.10±21.51 (12.71-107.60)	29.20±18.50 (4.80-66.86)
MMSE	29.29±0.87 (27-30)	29.81±0.39 (29-30)	20.20±8.75*$ (5-30)	23.22±8.94 (5-30)	23.33±6.50*$ (6-30)	28.67±1.70 (24-30)
CDR	-	-	0.57±0.35 (0-1)	0.44±0.68 (0-2)	1,154±0.98 (0-3)	-
CDR SB	-	-	2.57±3.05 (5-7)	2.05±2.75# (0-8.5)	7±5.26 (0.5-17)	-
ALSFRS [0-48]	-	-	-	-	-	42.37±3.28 (36-46)

3.2 MRI Acquisition

All patients and healthy controls underwent brain MRI on a 3T scanner (Philips Medical Systems, Best, the Netherlands) at IRCCS San Raffaele Hospital. The following sequences with their respective parameters were acquired:

- 3D T1-weighted turbo field echo (TFE) (TR=7 ms, TE=3.2 ms, TI=1000 ms, 204 sagittal slices with voxel size=1x1x1 mm, matrix=256x256, FOV=256x256 mm^2)
- Axial pulsed-gradient spin echo (PGSE) single shot DW EPI (3 shells at b value = 700/1000/2855 s/mm2 along 6/30/60 non-collinear directions and 10 b = 0 volumes were acquired, FOV = 240 × 233 mm, pixel size = 2.14 × 2.69 mm, 56 slices, 2.3 mm thick, matrix=112×85, TR=5900 ms, TE=78 ms, TA = 10 min)
- T2*-weighted single-shot EPI for RS fMRI (TR/TE 1567/35 ms, flip angle 70°, FOV 240 mm^2, pixel size = 2.5x2.5 mm, 320 sets of 48, 3-mm thick axial slices)

A line connecting the most infero-anterior and infero-posterior portions of the corpus callosum was used as the reference for positioning all slices. Subjects were asked to remain motionless, keep their eyes closed, and not focus on anything specific while undergoing RS fMRI scanning.

3.3 MRI Analysis

3.3.1 Brain Parcellation

The nodes of the brain network were identified using anatomical T1-weighted images (Figure 33). Grey matter (GM) was parcellated using a novel method based on 220 similarly sized areas, which combines the requirement for a large number of equal sized nodes with respecting anatomical landmarks [148, 166]. The 220 regions included the cerebral cortex and basal ganglia, while the cerebellum was excluded. The 220 GM regions of interest (ROIs) were moved into the subject's space by calculating and concatenating the registrations between subject's T1-weighted image and MNI152 standard space (linear and non-linear using FLIRT [167] and FNIRT [168], respectively, as implemented in FSL [FSLv5.0.9; http://www.fmrib.ox.ac.uk/fsl]), between subject's RS-fMRI and T1-weighted images

(linear registration as implemented in FLIRT), and between subject's DT MRI (B0 image) and T2-weighted images (linear and non-linear using FLIRT and FNIRT). In order to concatenated T2-weighted images and AAL brain regions, T1-weighted and T2-weighted images registration was implemented in FSL (linear using FLIRT [167]).

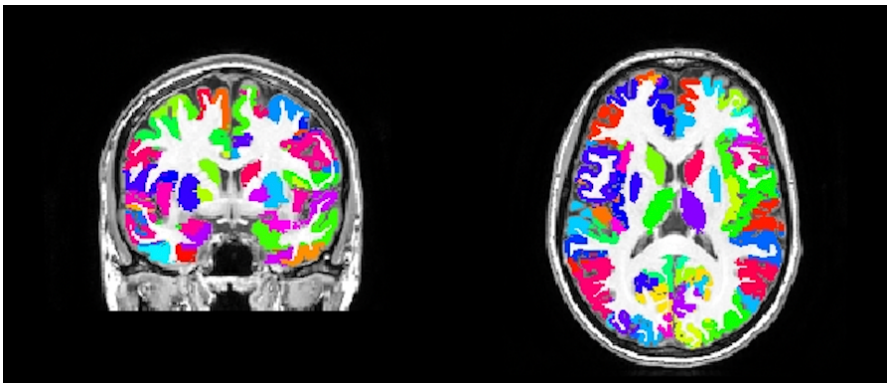

Figure 33: T1-weighted image parcellation.

3.3.2 T1-Weighted Image Processing

T1-weighted images of patients and healthy controls were registered to AAL atlas using linear and non-linear registrations (FLIRT [167] and FNIRT [168], respectively, as implemented in FSL). Cortical GM was segmented using SPM12, while basal ganglia, hippocampus and amygdala were obtained using FIRST in FSL.

3.3.3 Diffusion MRI Processing

3.3.3.1 Pre-Processing

The diffusion-weighted data were skull-stripped using the *Brain Extraction Tool* implemented in FSL and were corrected for distortions, caused by susceptibility-induced field and eddy currents, and movements (Figure 34). Corrections were implemented using more acquisitions, since it has been demonstrated that along the same direction but with opposite phase gradients applied, off-resonance fields change but diffusion signal is the same; predictions of the distortions are made along each diffusion direction and then averaged [169-172].

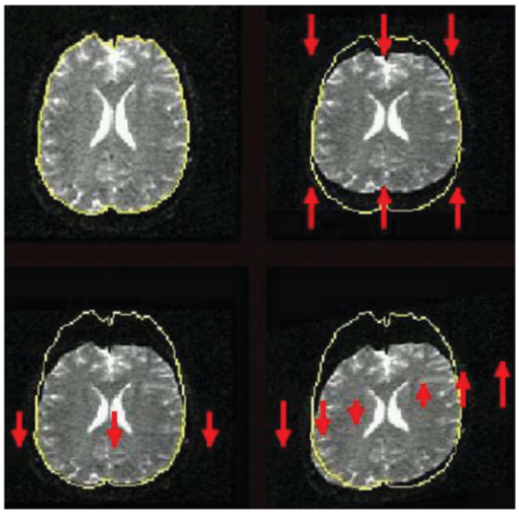

Figure 34: Three modes of distorsion resulting from eddy currents: contraction (top right), shift (bottom left), and shear [173].

Topup. Human body disrupts homogeneous magnetic field in the MRI scanner, causing susceptibility-induced off-resonance field and distortion in the images [171]. The topup tool in FSL (http://fsl.fmrib.ox.ac.uk/fsl/fslwiki/TOPUP) was used to make a prediction of susceptibility induced field and then applied in eddy correction.

Eddy correction. Rapidly switched diffusion encoding gradients are an additional source of off-resonance, inducing eddy currents. DWIs were corrected for eddy current induced distortions using the Eddy *tool within the FSL library (https://fsl.fmrib.ox.ac.uk/fsl/fslwiki/eddy).*

3.3.3.2 DTI

The diffusion tensor was estimated on a voxel-by-voxel basis using diffusion-tensor imaging fit provided by the FMRIB Diffusion Toolbox (https://fsl.fmrib.ox.ac.uk/fsl/fslwiki/FDT). In particular, *dtifit* command fits a diffusion tensor model at each voxel.

Input files required:

- Diffusion-weighted volumes;
- BET binary mask: A single binarised volume in diffusion space containing ones inside the brain and zeroes outside the brain;
- Gradient directions (bvecs);

- 3 b values (bvals) – 3 shells.

Outputs files are the 3 main eigenvectors and eigenvalues, and FA and MD maps.

3.3.3.3 NODDI

NODDI Matlab Toolbox (http://www.nitrc.org/ projects/noddi_toolbox) was used with default settings to estimate Intra-cellular Volume Fraction (ICVF), Orientation Dispersion Index (ODI) maps, providing a direct quantification of neurite morphology and its integrity [71, 72].

3.3.3.4 Tractography

Anatomically Constrained Tractography (ACT) method was used to generate white matter streamlines using MRtrix3 (http:// www.mrtrix.org/). This method allows generating streamlines coherent with white matter tracts, which tend to both originate and terminate in grey matter (Figure 35).

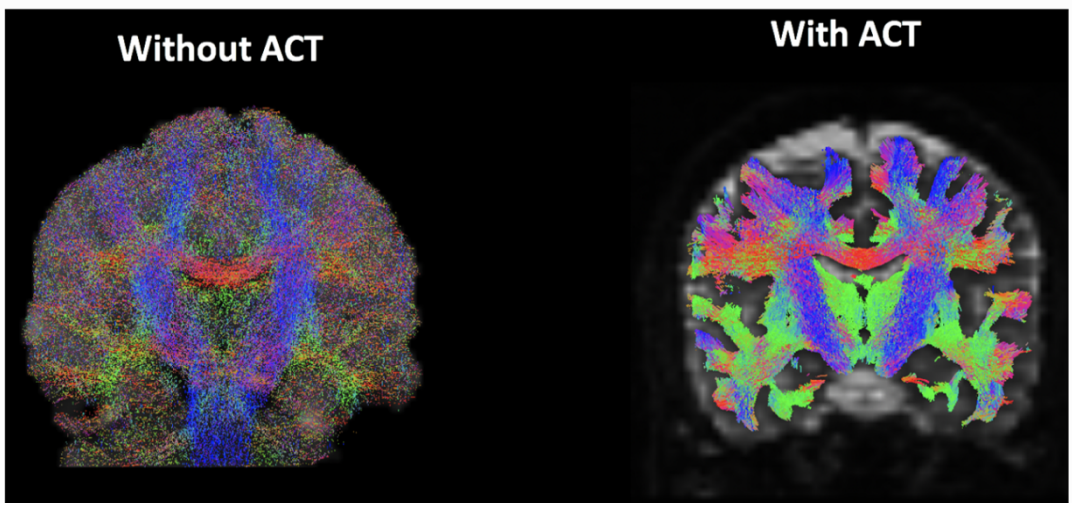

Figure 35: Tractograpgy without ACT on the left, Tractography with ACT on the right [64]

First, fiber orientation distributions (FODs) (Figure 36) estimation is obtained following the next MRtrix3 commands (http:// www.mrtrix.org/):

- *dti2response*: selection of voxels to use as basis functions for each tissue type in response to different b-values.
- *dwi2fod*: basis functions are used to create FODs for each tissue type (in figure 36 blue represents WM, green GM and red CSF)

With FODs estimation, MRtrix allows for the estimation of multiple crossing fibers within a single voxel, and can resolve the diffusion signal into multiple directions [64, 174].

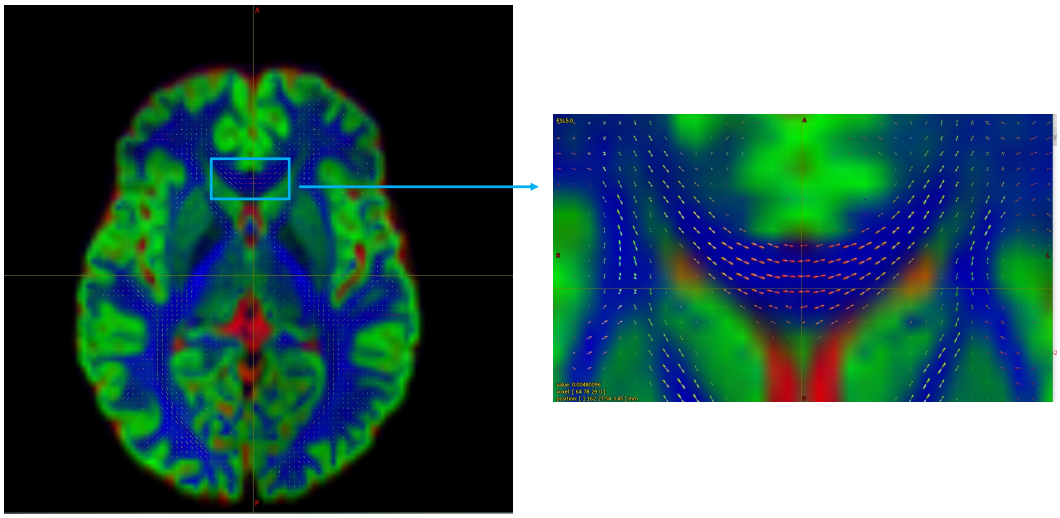

Figure 36: FODs representation.

Successively, using T1-weighted images, brain was segmented in five tissue types (GM, WM, subcortical regions, CSF, lesions) with 5ttgen MRtrix3's command, in order to create boundaries useful for ACT algorithm (Figure 37).

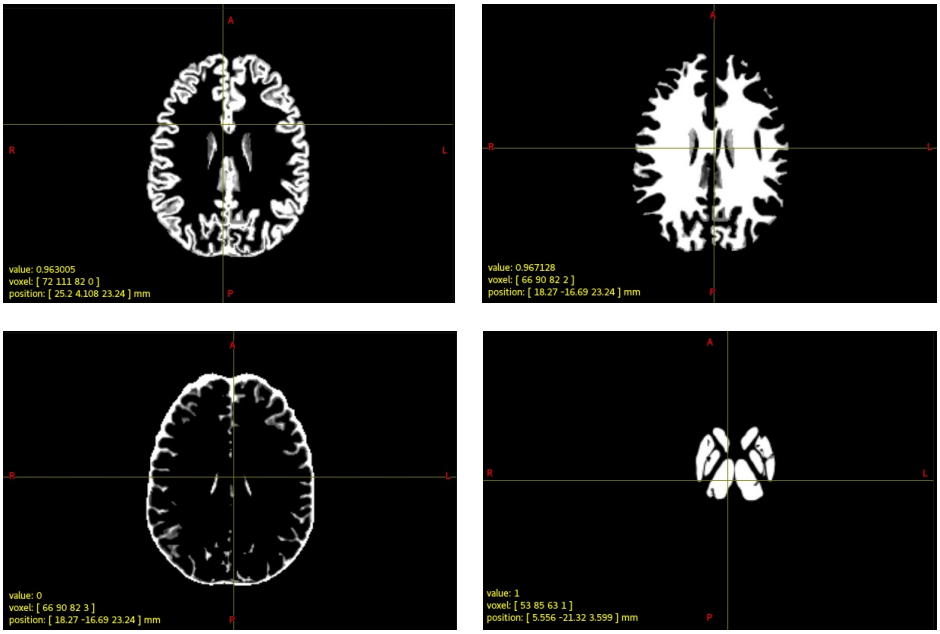

Figure 37: in order: GM, WM, CSF and subcortical regions segmentations.

After, co-registration of segmentations and diffusion weighted images. Finally, boundaries between GM and WM are created with 5tt2gmwmi, which are used as seed for streamlines.

Tractography can be now generated with *tckgen* command, using ACT method (Figure 38). A probabilistic tractography approach (*iFOD2 algorithm*) was used: at each voxel if there is high FOD amplitude along a path, streamline is more likely to follow that path, and rather than stepping along straight-line segments, the algorithm steps along a path given by arcs of fixed length (the step-size), tangent to the current direction of tracking at the current point [175]. It may also rarely traverse orientations where the FOD amplitudes are small, as long as the amplitude remains above the FOD amplitude threshold set to 0.06.

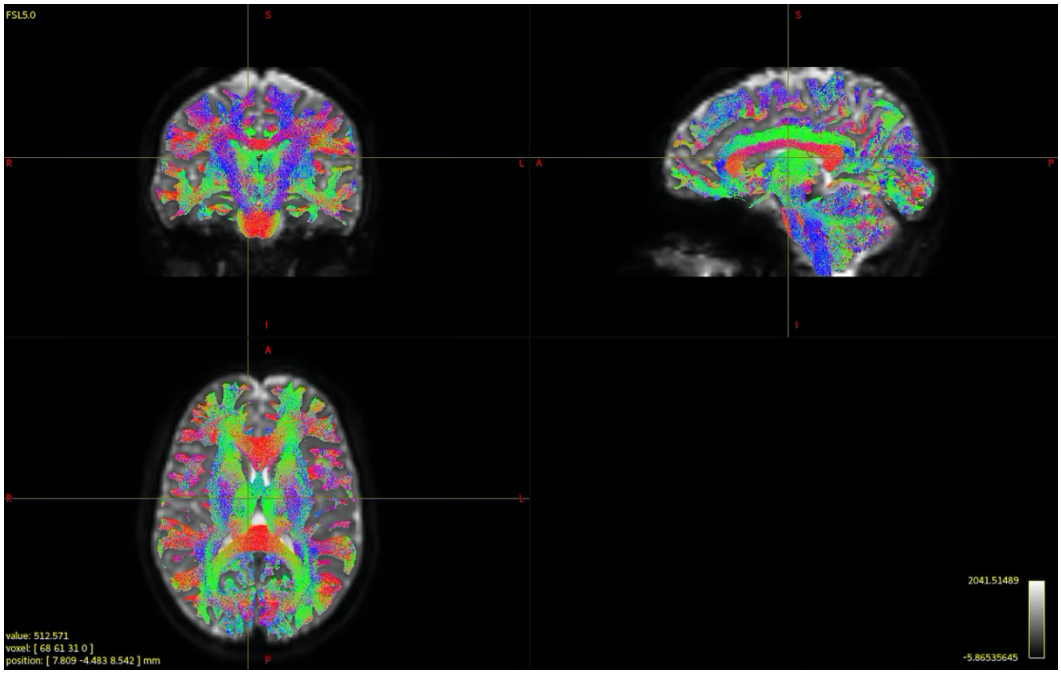

Figure 38: Final tractography obtained with SIFT algorithm.

The number of generated streamlines was set to 10 million, in order to reach a more accurate reconstruction of WM tracts. Some tracts could be over-represented because the fiber orientation densities are much clearer in some directions and so with more sights for the probabilistic algorithm. To counterbalance this overfitting, streamlines were then filtered through *tcksift* command that implement spherical-deconvolution informed filtering (SIFT) method. *Tcksift* implements a mechanism that compare FOD lobe integrals with streamline densities; a cost function contribution is evaluated in an iterative algorithm [176]. The process stops when it is achieved a target number of

remaining streamline (set to 1M streamlines) [176]. The tractography obtained presented an improved biological accuracy of a streamline reconstruction.

3.3.4 Structural matrices construction

Connectome matrices weighted by FA, ICVF and ODI measures were computed using MRtrix3 (http:// www.mrtrix.org/) in all groups of patients and old and young healthy controls. Firstly, using tcksample command, a mean FA/ICVF/ODI value per streamline was extracted. Then, through tck2connectome command, each streamline was assigned to a connectome nodes i and j and after for each connectome edge, the mean FA/ICVF/ODI of all streamlines assigned touching the couple i and j of node was calculated.

In order to mask weighted connectomes, connectivity matrices containing the number of streamlines (NOS) were obtained for each healthy young control by using the following procedure. 220 GM nodes of the connectome were defined by DWI brain parcellation (see section 3.3.1 for details). After, by using tck2connectome (http:// www.mrtrix.org/) command, streamlines from the whole-brain tractogram touching each couple i and j of nodes were selected. Then, the number of streamlines for each of these tracts was calculated and inserted in the symmetric and zero-diagonal connectivity matrix. If there was no streamline connecting a couple of nodes, then a zero was inserted in the corresponding cell of the NOS matrix to describe the lack of connections between that couples of nodes.

At this point, the averaged NOS connectivity matrix of young controls was used to mask FA/ICVF/ODI connectome; all connections with less than 3 NOS were set to zero.

To avoid considering spurious structural connections, the connections that were present in less than 60% of independent controls were set to zero [177, 178]. Finally, cells corresponding to zero were set to “Not a Number” (NaN) values in order not to be included in the network [146].

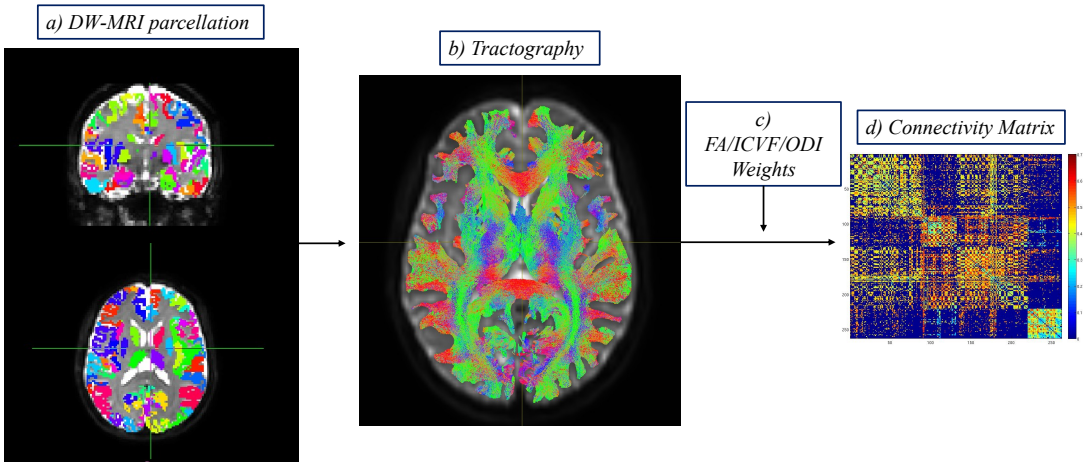

Figure 39: Structural connectome construction

3.3.5 Resting-State fMRI Processing

RS fMRI were pre-processed using the Statistical Parametric Mapping software package (SPM12; http://www.fil.ion.ucl.ac.uk/spm/) running on Matlab and FSL. Preprocessing included the following steps: removal of the first four volumes to allow for signal equilibration; minor head movement correction by volume-realignment to the middle volume using MCFLIRT; removal of nonbrain tissue. The REST software (http://resting-fmri.sourceforge.net/) was used to perform linear detrending and band-pass filtering between 0.01 and 0.08 Hz in an effort to largely eliminate physiological high-frequency noise and low-frequency drifts. By regressing out the six motion parameters calculated by MCFLIRT, as well as the average signals of the ventricular cerebrospinal fluid and white matter, non-neuronal sources of synchrony between RS fMRI time series and motion-related artifacts, were reduced using REST.

3.3.6 Functional matrices construction

In patients and both young and old healthy controls, undirected, weighted graphs describing brain network functional connectivity were obtained by computing correlations between the 220 GM segmented ROIs (section 3.3.1). By averaging the signal from all of the voxels inside each region, mean time series were derived from each ROI. In order to consider only the voxels that correspond to the GM and prevent the influence of atrophy, RS-fMRI data were mask with the subject's GM map. The

basal ganglia, including the bilateral caudate, globus pallidus, putamen, and thalamus, the hippocampus, and the amygdala, were mapped using FIRST in FSL while the cortical GM was segmented using SPM12. The Pearson's correlation coefficient between the mean time-series of each node pair, indicating the level of functional connectivity between regions *i* and *j*, was enter into cell *c*(*i*,*j*) of the matrix. Pearson's correlation coefficients were then converted to *z*-scores using Fisher's r-to-z transformation. In addition, functional connectivity matrices were masked using NOS of healthy young controls and setting to zero the connections that were present in less than 60% of independent controls [177, 178]. Negative values were set as 'NaN' to mark these brain regions as unconnected [146]. Finally, cells corresponding to zero were set to 'NaN' values in order not to be included in the network [146].

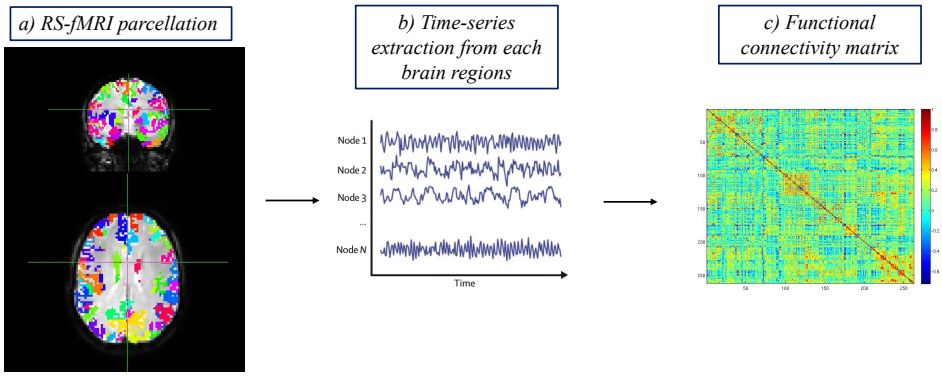

Figure 40: Functional connectome construction. [121]

3.3.7 Graph metrics

Global and mean lobar structural and functional network characteristics were explored using the Brain Connectivity Matlab toolbox (http://www.brain-connectivity-toolbox.net).

The following metrics were extracted from both structural and functional maps: *degree centrality (DC), Sum node weights (SN), Eigenvector centrality (EC) and Mean distance (MD)*

In order to investigate the network characteristics in different brain regions, the 220 GM areas were grouped into six anatomical macro-areas: frontal lobe, sensorimotor area, basal ganglia, parietal lobe, temporal lobe and occipital lobe. Global and local metrics were compared between groups using ANOVA models adjusted for age and

sex, followed by post-hoc pairwise comparisons, Bonferroni-corrected for multiple comparisons ($p<0.05$). Violin plots were used to visualize metrics distribution among patients in the six different macro-areas.

3.3.8 Network Based Statistics

NBS [137] were used to compare FA/ICVF/ODI and functional connectivity strength between patients and controls at the level of significance $p<0.05$.

The NBS analysis was performed as follow: first, for each connection in the brain network, the mean difference in regional connectivity network data between two groups was tested using a two-sample t-test (leaving out zeros). Within this procedure, differences in connectivity with a $p < 0.05$ were marked as ones in an "affected matrix". Then, the size of the largest connected component, which is the largest cluster of connections that was altered when comparing two groups, was found. At this point, the permutation test is used to assign a p value controlled for the FWE to the considered altered connectivity pattern due to the inherent massive number of multiple comparisons that must be performed and the great effort in testing the normality per each connection. At each permutation, subjects were randomly assigned to two different groups of the same size of the starting groups and the t-test with the NBS procedure was repeated estimating each time the size of the largest connected component. The null distribution of maximal component size was obtained and a corrected p-value was calculated as the number of the components that had a higher size value than the observed component size, to confirm the statistical significance of the components observed in the initial logical difference matrix. In this study, 10000 permutations were performed for all network analyses. If such a procedure resulted in a corrected p value <0.05, affected connections were obtained. All the analyses were adjusted for age and sex.

3.3.9 Network Diffusion Model

NDM [127] was implemented to simulate the spread of disease into the network represented by the connectivity matrix (C) over time t starting from a "seed" region. Particularly, the diffusion model started from baseline MRI data of healthy subjects' connectome $C= \{e, n\}$, where $e_{i,j}$ represents the pathways connecting structures *i* and

j; n_i represent the i^{th} cortical or subcortical gray matter structure. FA, ICVF and functional measures were used to implement the model.

The spread of pathology between an affected brain region (R_2) to an unaffected one (R_1) is given by:

$$\frac{dx_1}{dt} = \beta c_{1,2}(x_2 - x_1)$$

(18)

- $x_{1,2}$: pathology concentration in region $R_{1,2}$
- $c_{1,2}$: connectivity between R_1 and R_2
- β: diffusivity constant (higher is the value higher is the speed of pathology progression);

Pathology from all brain regions is combined into a vector $x(t)=\{x_i(t)\}$, and equation 3 becomes:

$$\frac{dx(t)}{dt} = -\beta L x(t)$$

(19)

- $x(t)=\{x_i(t)\}$: represents the amount of diffusion of pathology at node *i* and timepoint *t* starting from an initial distribution at time t=0 (x(0));
- L: Graph Laplacian matrix;
- t: time-points (arbitrary unit);

From matrix algebra, equation (19) is satisfied by:

$$x(t) = e^{-\beta t L} x(0)$$

(20)

where x(0) is a vector with 1 at the index corresponding seed brain regions where it is thought that the pathology begins to spread, 0 at all other brain regions. Four disease epicenters were identified from the peaks of atrophy of each FTLD variant: left inferior

temporal gyrus (svPPA), right orbitofrontal cortex (bvFTD), left supplementary motor area (nfvPPA) and precentral gyrus (MND).

The graph Laplacian represents the discretization of Laplacian operator and indicates how a graph differs at one vertex from its values at nearby vertices. It was implemented as follow:

$$L = I - D^{-\frac{1}{2}} C D^{-\frac{1}{2}}$$

(21)

- I: identity matrix;
- D: Diagonal matrix whose diagonal entries contain degree of each node;
- C: Averaged connectome of healthy subjects;

Because brain regions are not the same size and have different node degree, L in eq. (5) is the normalized version of graph Laplacian operator. It is a symmetric matrix and its eigenvector are orthonormal.
The solution of equation (1) was mathematically implemented in Matlab by the eigenvalue decomposition:

$$x(t) = \sum_{i=1}^{N} (e^{-\beta \lambda_i t} u_i^t x_0) u_i$$

(22)

- *N*: brain regions
- λ: eigenvalues of matrix L
- *u*: eigenvectors of matrix L

Brain Net Viewer was used to create diffusion maps [179]. (http://www.nitrc.org/projects/bnv/)

Subsequently, network vulnerability was tested through correlation between predicted atrophy obtained by NDM in young controls and longitudinal pattern of atrophy in FTLD patients. Specifically, Pearson's correlation will be calculated between the estimated atrophy by the NDM in young controls and the atrophy empirically

calculated in different groups. The latter was calculated as follow: GM maps were obtained starting from T1-weighted imaging and parcellated into 220 AAL regions of interest, obtaining the volumes of each brain region for healthy subjects at baseline and from patients at each follow-up. Afterwards, t-score was implemented as follow [127]:

$$t = \frac{\mu_{HC} - \mu_{pat}}{\sqrt{\frac{\sigma_{HC}^2}{N_{HC}} + \frac{\sigma_{pat}^2}{N_{pat}}}} \quad (23)$$

- μ_{HC}: mean of the healthy controls volumes at baseline
- μ_{pat}: mean of the patients volumes at each follow-up
- σ_{HC}: standard deviation (std) of the healthy controls volumes at baseline
- σ_{pat}: std of the patients volumes at each follow-up
- N_{HC}: number of healthy subjects
- N_{pat}: numbers of patients

Therefore, Pearson's Correlation was tested between NDM prediction in young controls and t-score at different follow-up in patients.

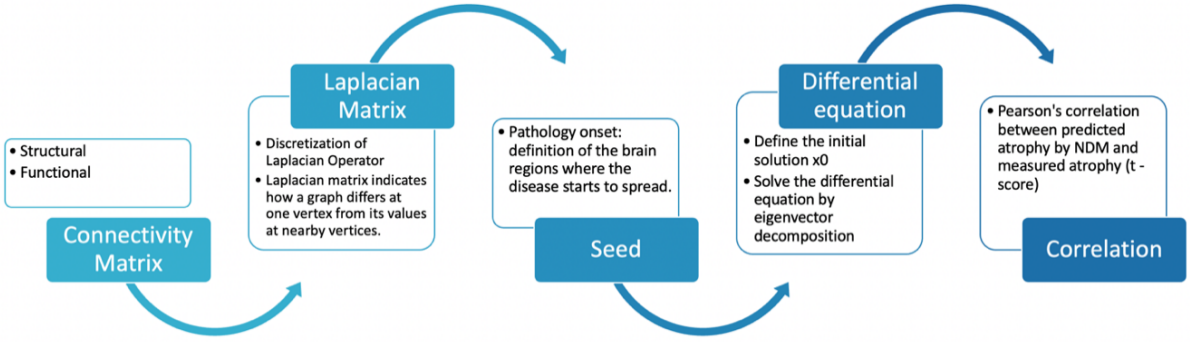

Figure 41: Summary of NDM procedure

3.3.10 Structural-functional correlations

To assess the relationship between structural and functional connections, correlation analysis was performed in each group (patients and both young and old controls).

Correlations between MRI measures were estimated using Pearson correlation coefficient (R), at the level of significance $p < 0.05$. Specifically, correlations were tested between FA measure and functional connectivity and between ICVF measure and functional connectivity, for each subjects group.

CHAPTER 4: RESULTS

4.1 Graph metrics

A summary of structural altered metrics at global, lobar and regional levels in the FTLD spectrum are shown in figures 42, 43 and 44. Overall, groups did not show significant differences in functional graph metrics within whole brain.

bvFTD patients vs other groups

Overall, bvFTD patients showed altered structural FA global network properties, such as higher MD and lower DC, SN and EC compared to healthy controls, MND and svPPA patients. Also in all lobes, bvFTD patients showed a reduced DC and SN, and longer MD relative to healthy controls and MND patients. Only in the temporal and occipital lobes, it was observed an increased EC in bvFTD patients compared to MND patients (Figure 42). ICVF and ODI measurements showed network properties similar to FA maps, with the exception of SN in ODI maps, which showed no significant results.

nfvPPA vs other groups

Overall, nfvPPA patients showed altered FA properties, high DC, SN and EC and low MD, at a global level compared to healthy controls and MND patients. This condition was also verified at a lobar level, in particular in frontal, sensorimotor, basal ganglia, parietal, and temporal lobes. ICVF and ODI metrics showed the same results as FA.

svPPA vs other groups

svPPA patients did not showed altered FA metrics. In contrast, ICVF graph analysis showed that svPPA had a low DC and SN in the temporal lobe compared to healthy controls and MND (Figure 43). In addition, ODI metrics distinguished svPPA patients from controls and MND in the temporal lobe (DC) and at a global level (EC) (Figure 44).

MND vs other groups

MND patients showed an altered EC in FA maps, in the sensorimotor lobe compared to healthy controls. ICVF and ODI maps did not show altered metrics in MND patients compared with other groups.

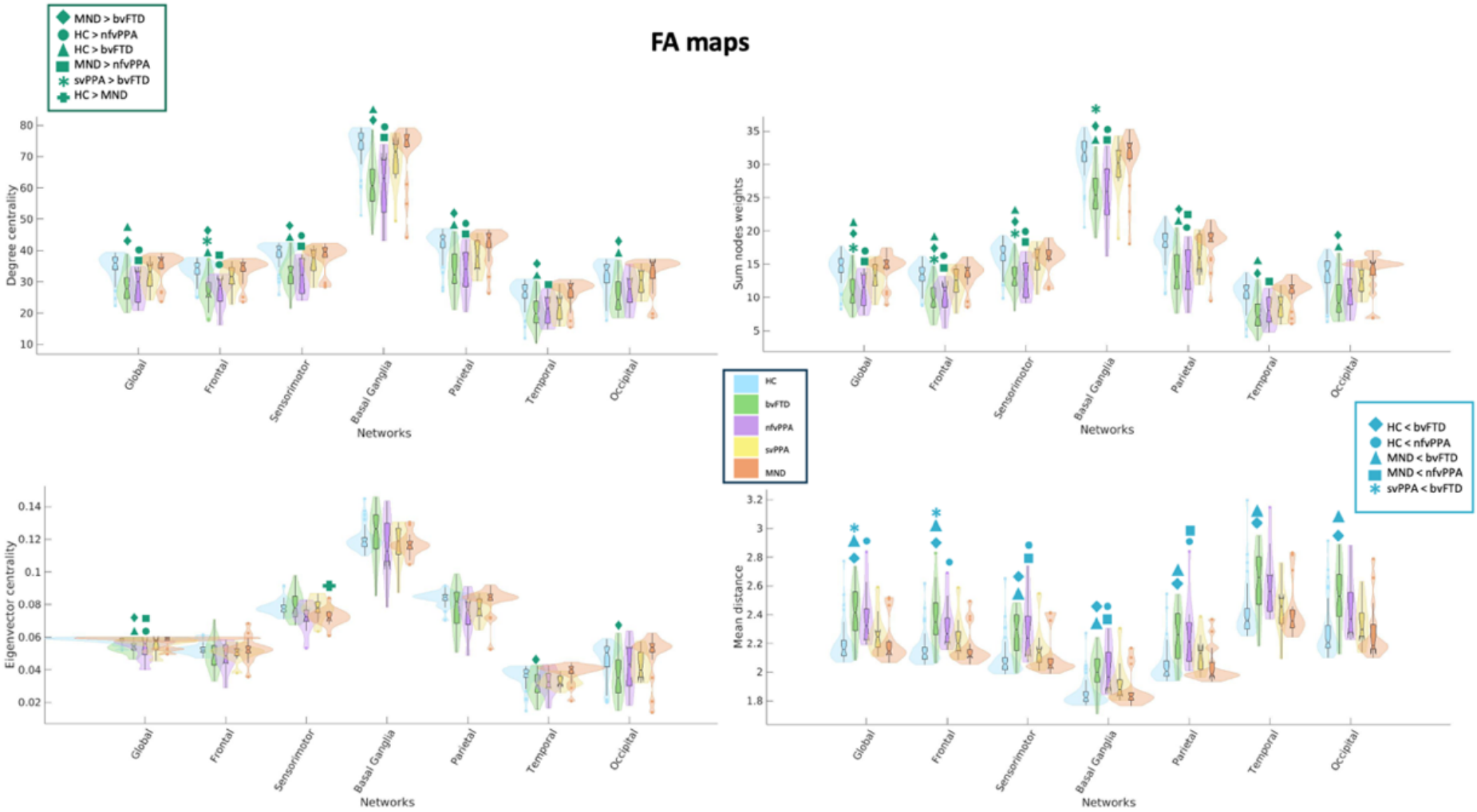

Figure 42: Violin plot of FA degree centrality (DC), sum of the node weights (SN), eigenvector centrality (EC) and mean distance (MD) of each brain lobe and global brain.

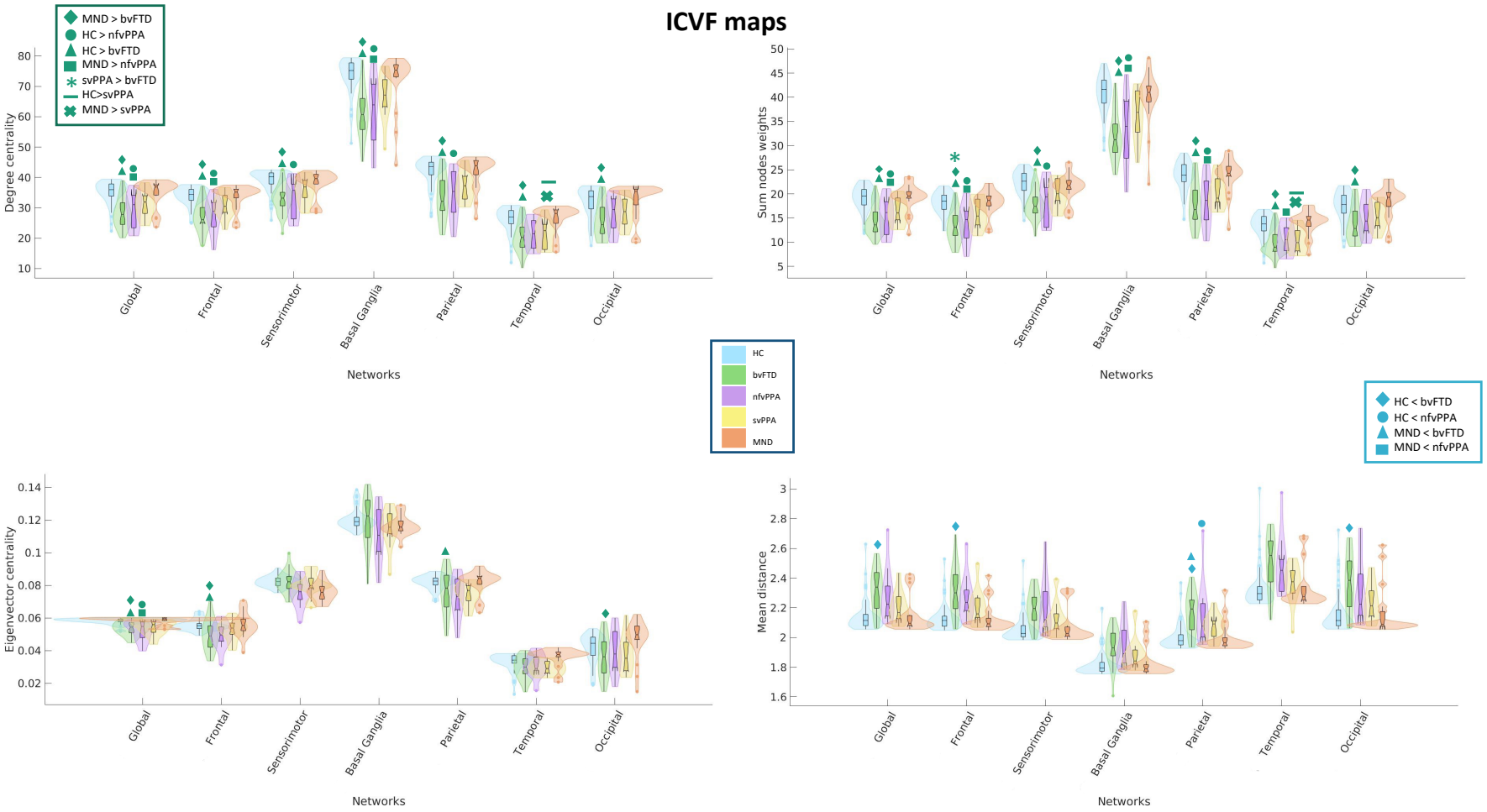

Figure 43: Violin plot of ICVF degree centrality (DC), sum of the node weights (SN), eigenvector centrality (EC) and mean distance (MD) of each brain lobe and global brain.

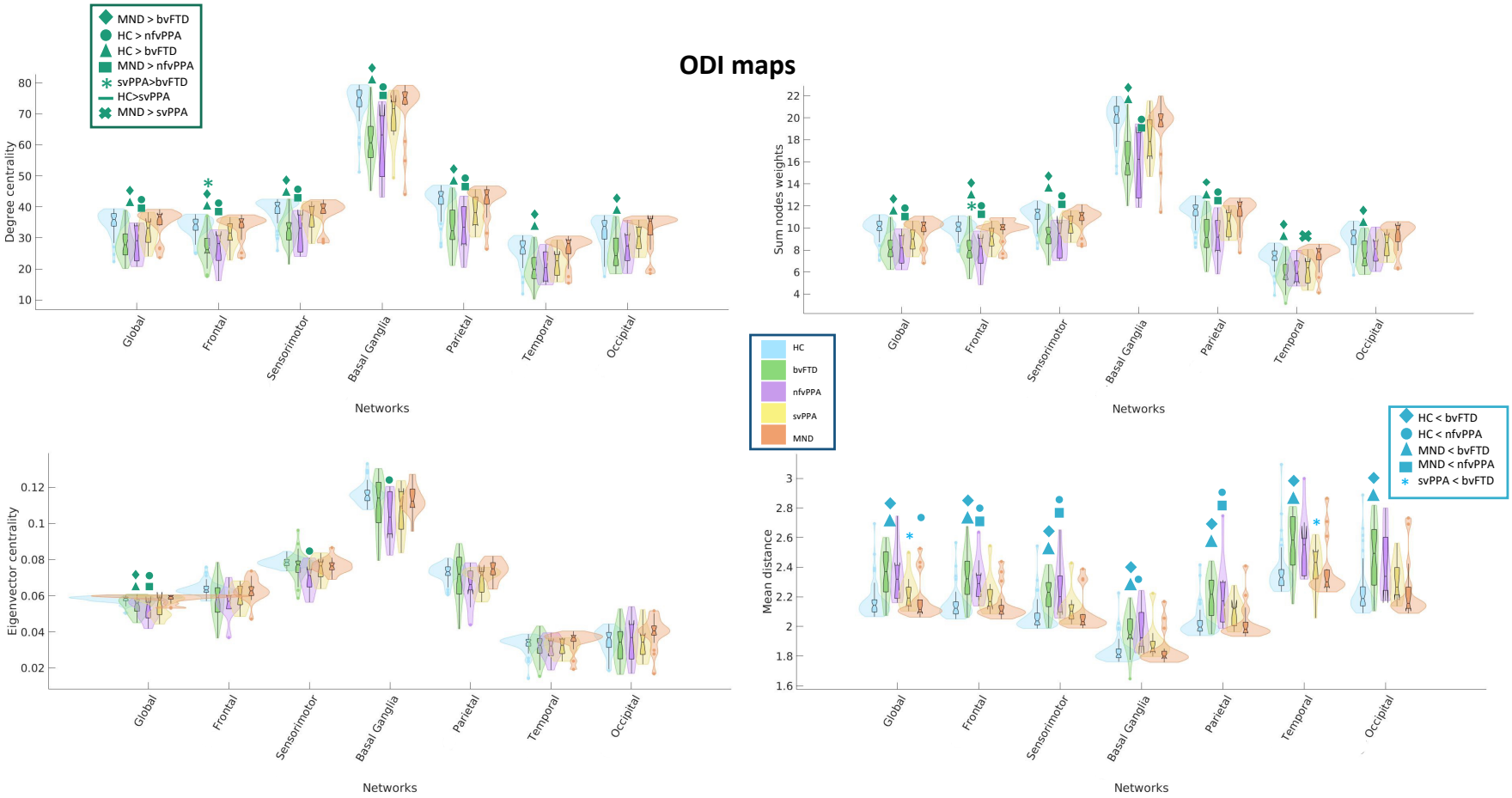

Figure 44: Violin plot of ODI degree centrality (DC), sum of the node weights (SN), eigenvector centrality (EC) and mean distance (MD) of each brain lobe and global brain.

4.2 Network Based Statistics

bvFTD patients vs other groups

Using NBS, widespread structural changes were observed in patients with bvFTD relative to controls: FA decreased significantly in all brain areas. In addition, MND patients showed increased FA compared to bvFTD patients in all brain areas except the occipital lobe where fewer connections were involved. In addition, bvFTD patients showed marked decreased FA strength relative to svPPA patients, in particular in the right hemisphere, involving the whole frontal lobe, sensorimotor lobe (supplementary motor area), basal ganglia (putamen), parietal, temporal (superior and middle temporal gyri) and occipital (middle and superior occipital gyri, calcarine) lobes. However, considering ICVF measure, it was detected a more widespread pattern of structural alterations compared to FA maps in bvFTD compared to controls, svPPA, and MND patients (Figure 45). Furthermore, bvFTD patients presented a decreased ODI compared to controls, in particular in the right hemisphere, involving sensorimotor (precentral gyrus, supplementary motor area), basal ganglia (thalamus), parietal (inferior and superior parietal, and postcentral gyri) and temporal (temporal middle gyrus, superior temporal pole and hippocampus) lobes and insula and cingulum.

Considering functional results, NBS analysis showed that bvFTD patients had a decreased functional connectivity compared to healthy controls, in particular in the temporal lobe (superior and middle gyri), and an increased functional connectivity in the occipital lobe (calcarine sulcus, cuneus) relative to MND patients. An increased functional connectivity of bvFTD patients was also found compared to nfvPPA patients, involving in particular sensorimotor and occipital areas (Figure 46).

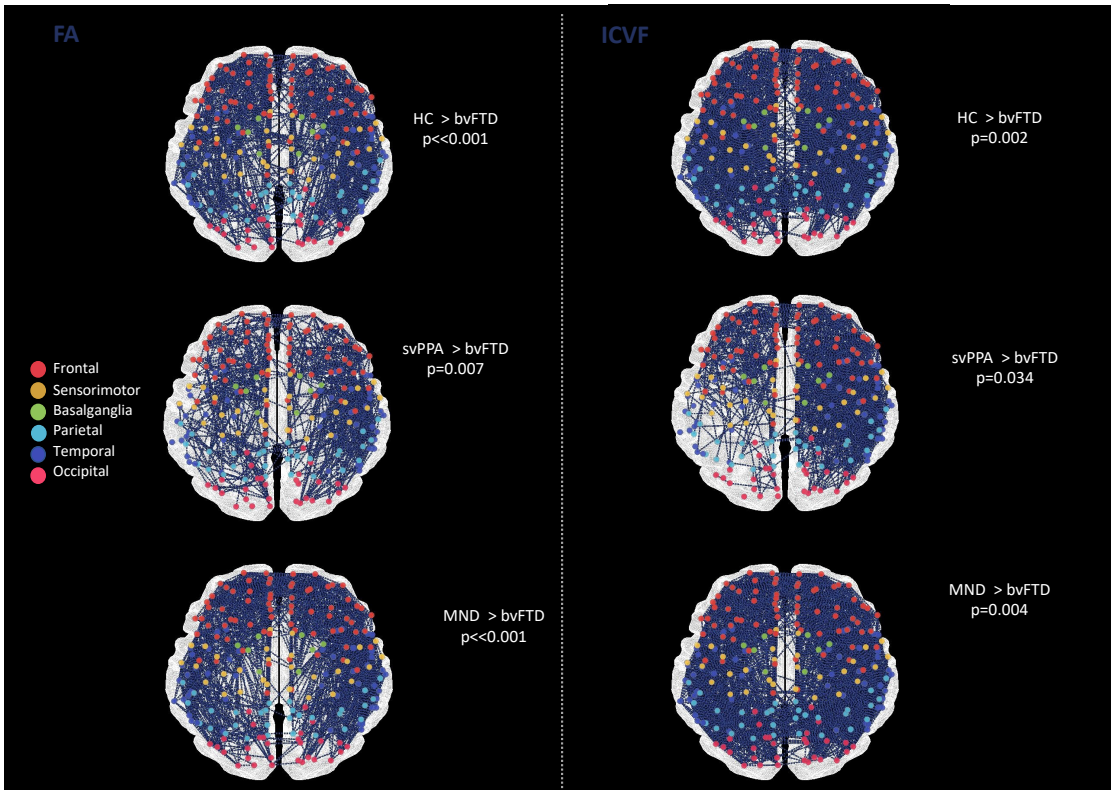

Figure 45: On the left, FA NBS results involving bvFTD patients, on the right ICVF NBS results involving bvFTD patients.

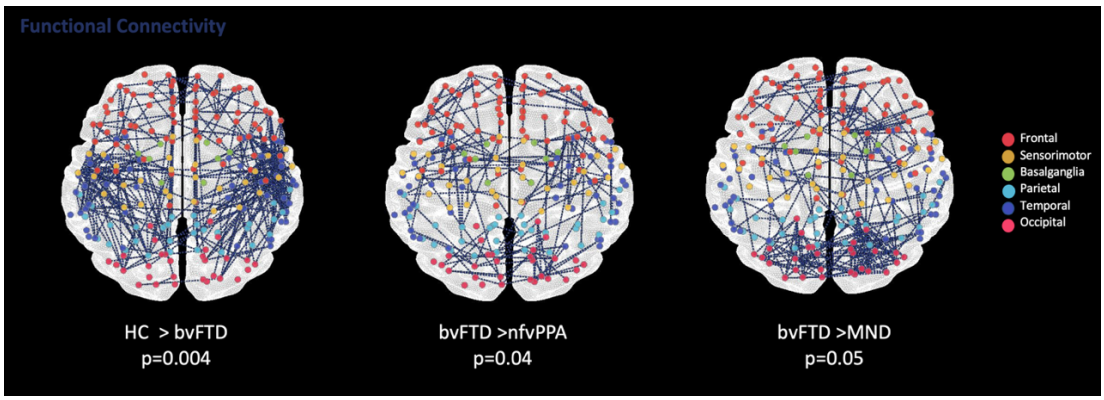

Figure 46: NBS results on functional connectivity matrices.

nfvPPA vs other groups

NBS analysis showed an evident decreased FA in nfvPPA patients relative to controls and MND patients predominantly in the left hemisphere, involving frontal lobe, sensorimotor (precentral gyrus, supplementary motor area), basal ganglia (putamen), the whole temporal lobe and insula and cingulum. Moreover, using NBS on IVCF matrices it was found, as in bvFTD patients, an increase number of altered connections were present in FA maps, allowing to differentiate also svPPA and nfvPPA patients. Indeed, nfvPPA patients showed a decreased ICVF compared to svPPA patients,

involving frontal, sensorimotor (supplementary motor area), and parietal (postcentral gyri) areas and insula and cingulum as shown in figure 47. While nfvPPA patients compared to controls showed a widespread alteration of ICVF connectivity, marked decrease pattern of connectivity was found only in the left hemisphere relative to MND patients. nfvPPA show also a decreased functional connectivity in the frontal, sensorimotor (supplementary motor area) and occipital (occipital superior gyrus and calcarine) lobes compared to bvFTD (Figure 46). Moreover, nfvPPA patients showed a decreased ODI compared to healthy controls involving frontal (inferior frontal gyri), sensorimotor (supplementary motor area and precentral gyri) and parietal (postcentral and supramarginal gyri) areas.

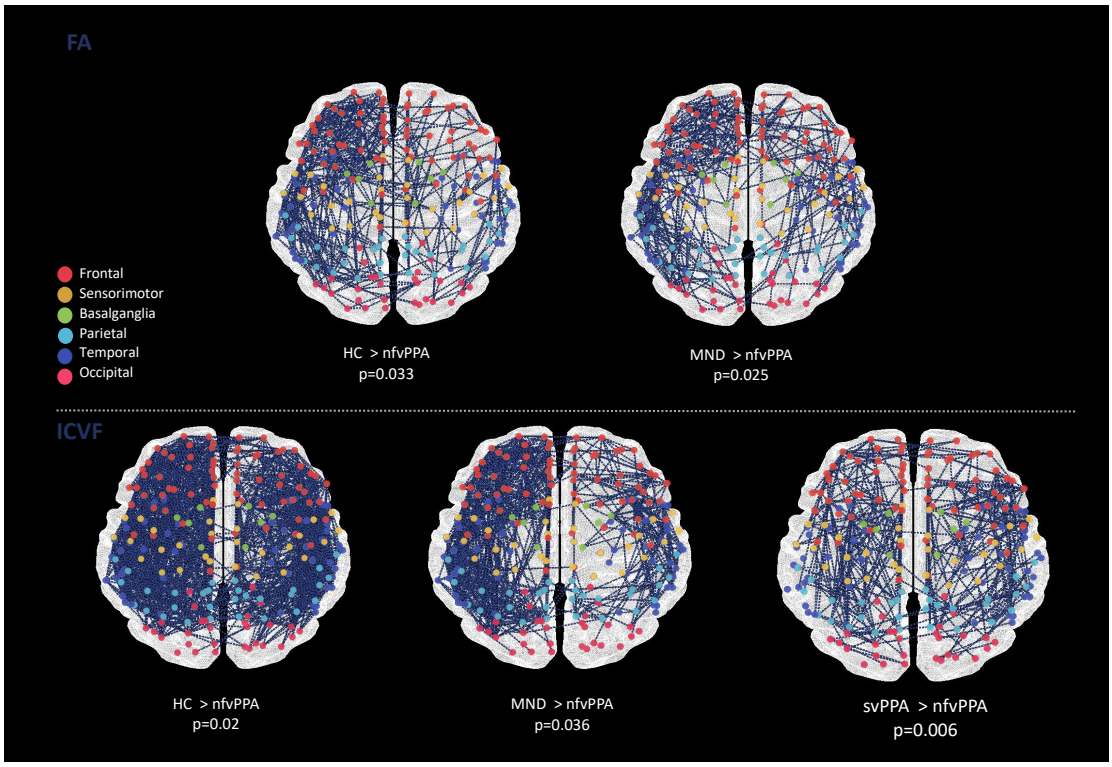

Figure 47: on the left FA NBS results involving nfvPPA patients, on the right ICVF NBS results involving nfvPPA patients

svPPA vs other groups

svPPA patients did not showed altered FA and ICVF measures compared to other groups. Whereas, svPPA patients showed a reduced ODI compared to control and MND involving more the left hemisphere in the sensorimotor (supplementary motor area), superior and inferior parietal (superiorior and inferior parietal and supramarginal

gyri), temporal (superior and middle gyri, hippocampus, parahippocampal, and fusiform gyri) lobes (Figure 48).

MND vs other groups

MND patients did not showed altered structural or functional connectivity, but rather they preserved connectivity compared to all other patients groups except in the occipital lobe where NBS analysis showed a decreased functional strength relative to bvFTD patients (Figure 46).

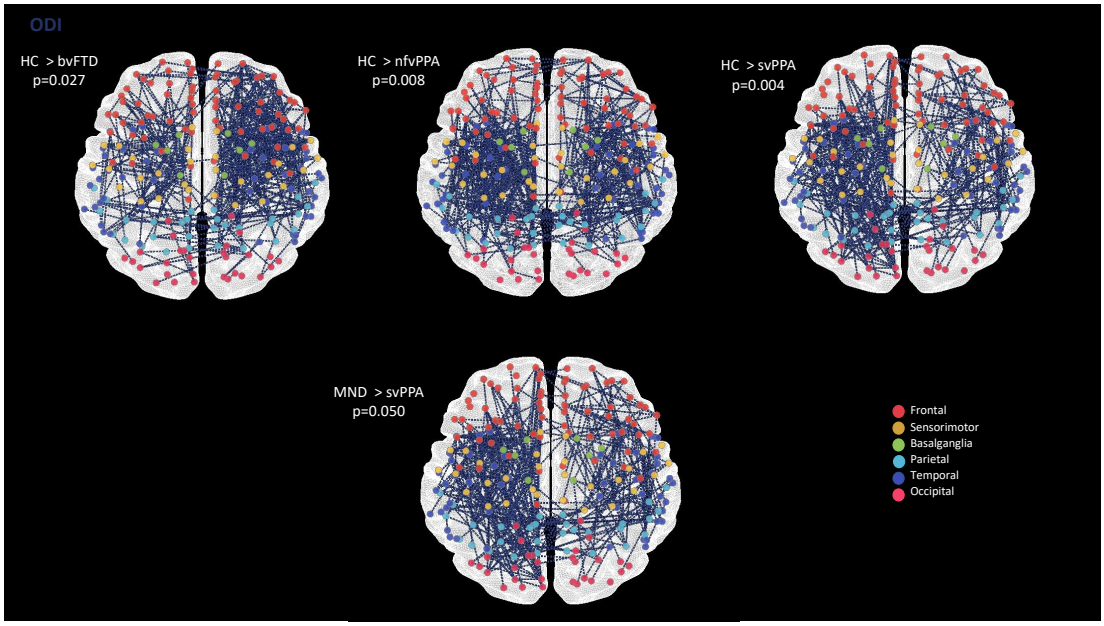

Figure 48: ODI NBS results.

4.3 Network Diffusion Model

The predictive maps obtained by NDM in 48 young controls are shown in Figures 49, 50, 52, 53, 55, and 56, where pathologies progression at each time point are represented. The biggest sphere is in the region chosen as seed, whereas the size of the other spheres represent where and how much the pathology is more likely to spread. Overall, FA, ICVF and functional connectome showed the same pattern of spreding.

Considering bvFTD cases, NDM showed an early spread to the frontal lobe and basal ganglia (caudate, and putamen) and cingulum. After 12 months also the right sensorimotor (postcentral gyri and supplementary motor area), parietal (postcentral gyrus and precuneus), temporal and occipital (calcarine sulcus and lingual gyrus) lobes are involved, predominantly in the contra-lateral hemisphere between 18 and 24 months (Figure 49 and 50).

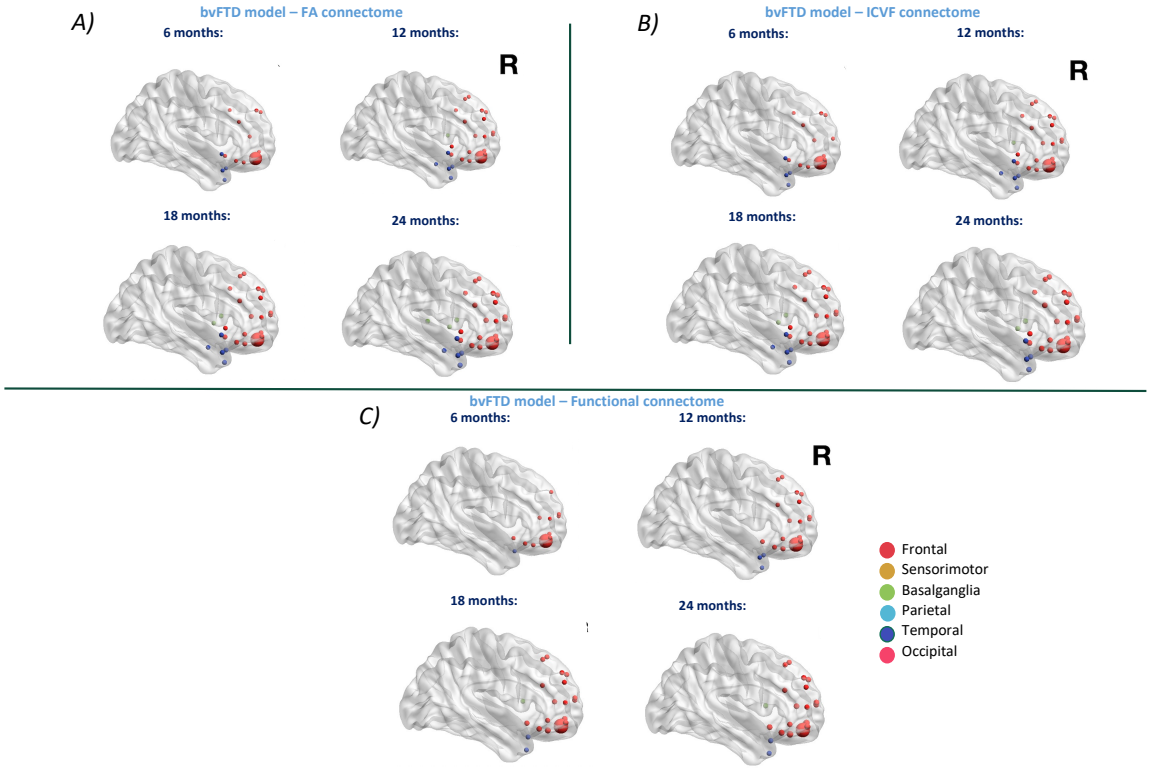

Figure 49: Sagittal view A) bvFTD spreading prediction by NDM applied on FA connectome B) bvFTD spreading prediction by NDM applied on ICVF connectome C) bvFTD spreading prediction by NDM applied on functional connectome.

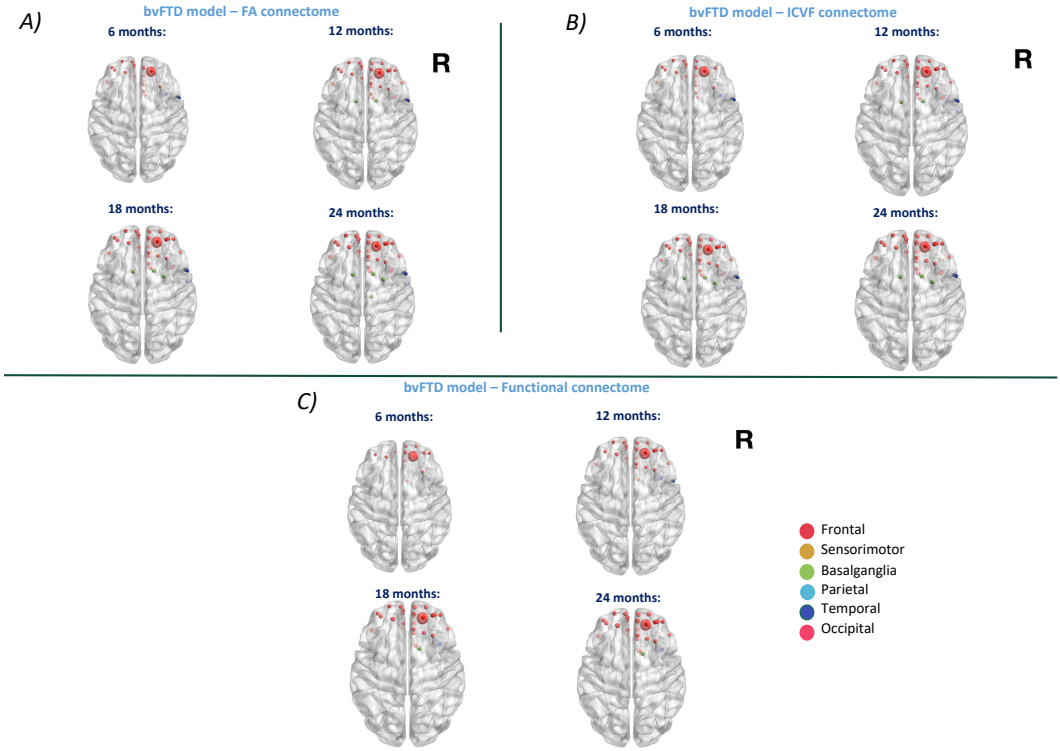

Figure 50: Transversal view A) bvFTD spreading prediction by NDM applied on FA connectome B) bvFTD pathology spreading prediction by NDM applied on ICVF connectome C) bvFTD pathology spreading prediction by NDM applied on functional connectome

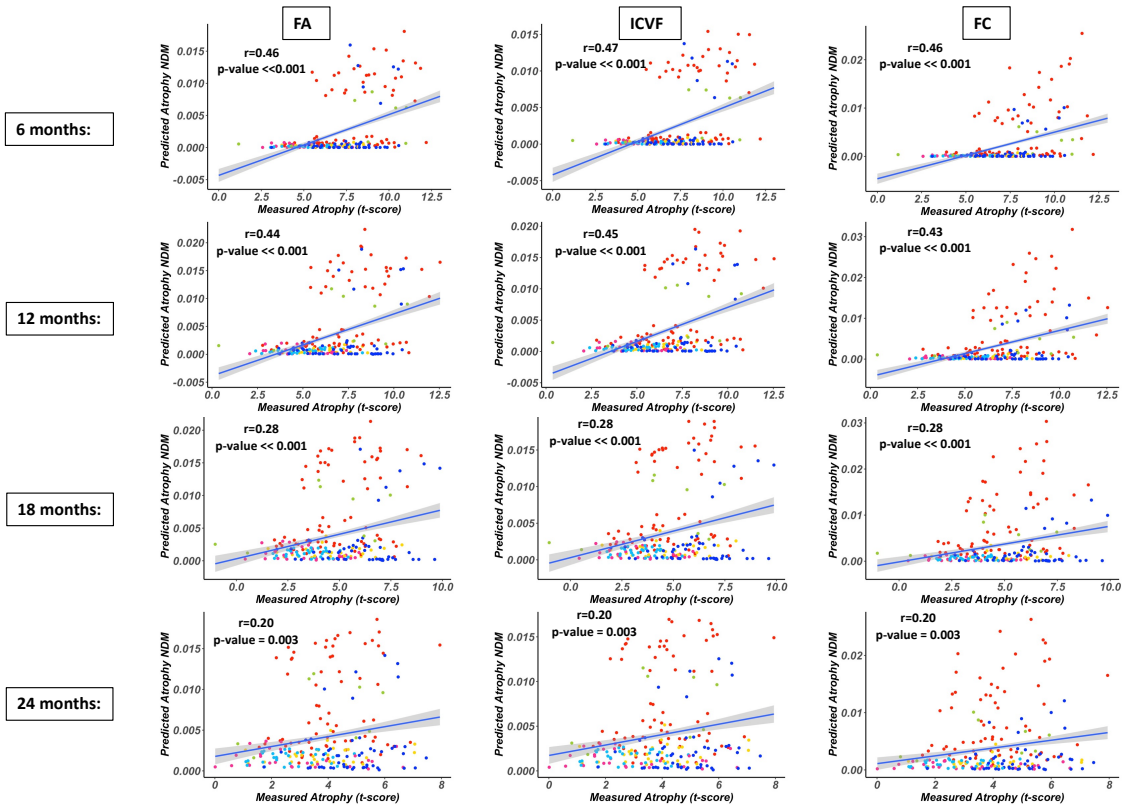

Figure 51: Correlations between atrophy t-score and atrophy predictions in svPPA patients on FA, ICVF and functional connectivity (FC) matrices are represented, at 6,12, 18 and 24 months

In nfvPPA patients, the disease initially involves frontal, sensorimotor (precentral gyrus, supplementary motor area), parietal and temporal (superior and middle temporal gyri) lobes. Finally, after 12 months, there is an involvement of the occipital lobe (occipital middle gyrus) (Figure 52 and 53).

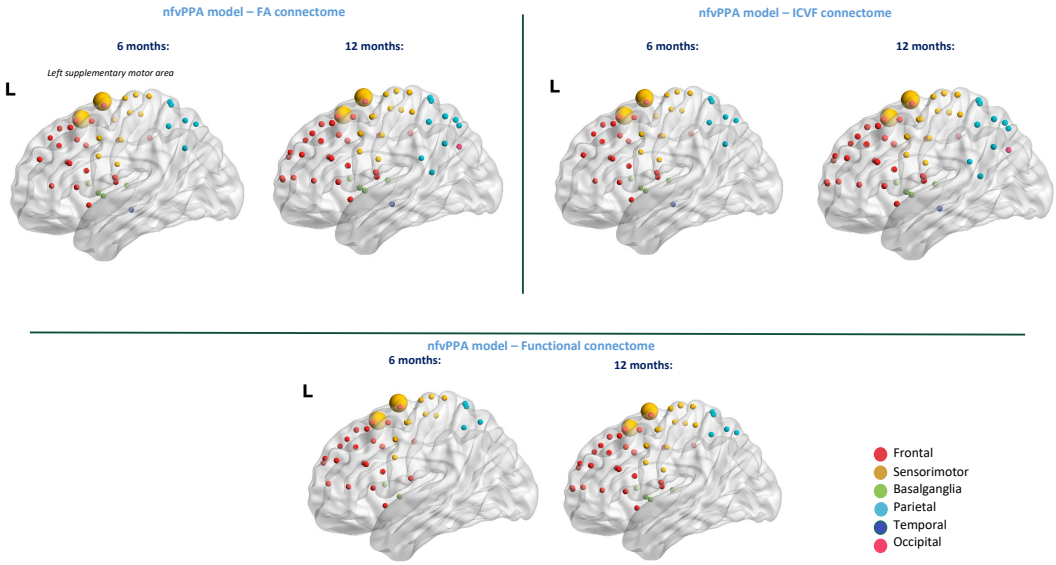

Figure 52: Sagittal view A) nfvPPA spreading prediction by NDM applied on FA connectome B) nfvPPA pathology spreading prediction by NDM applied on ICVF connectome C) nfvPPA pathology spreading prediction by NDM applied on functional connectome.

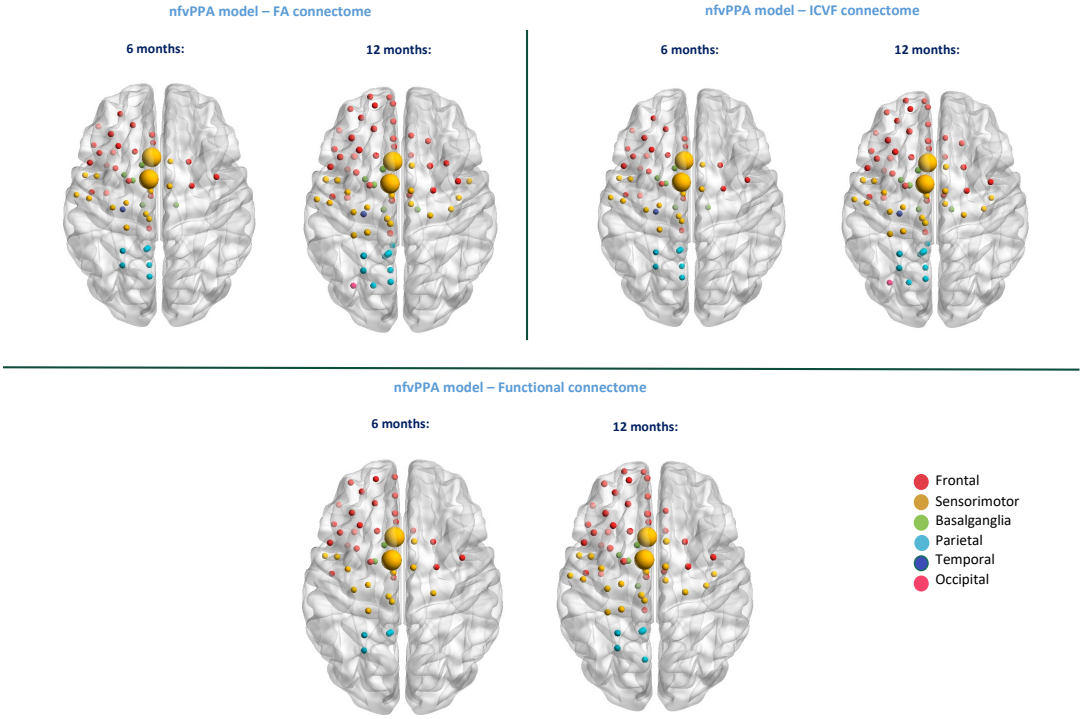

Figure 53: Transversal view A) nfvPPA spreading prediction by NDM applied on FA connectome B) nfvPPA pathology spreading prediction by NDM applied on ICVF connectome C) nfvPPA pathology spreading prediction by NDM applied on functional connectome

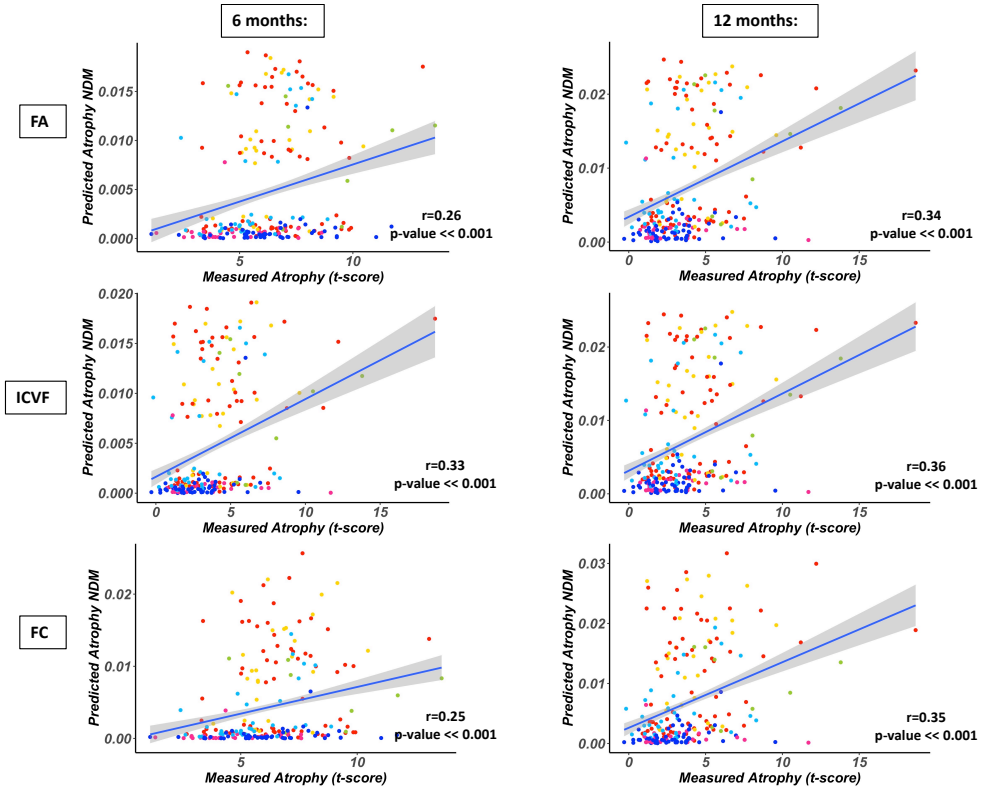

Figure 54: Correlations between atrophy t-score and atrophy predictions in nfvPPA patients on FA, ICVF and functional connectivity (FC) matrices are represented. On the left it is represented the correlation at 6 months, on the right at 12 months.

Maps suggested an early spread of svPPA pathology to the whole left temporal lobe, part of the occipital lobe (calcarine and fusiform) and insula at 6 months (Figure 55) and basal ganglia (amygdala, putamen) and frontal lobe (inferior frontal gyrus) at 12 months (Figure 55).

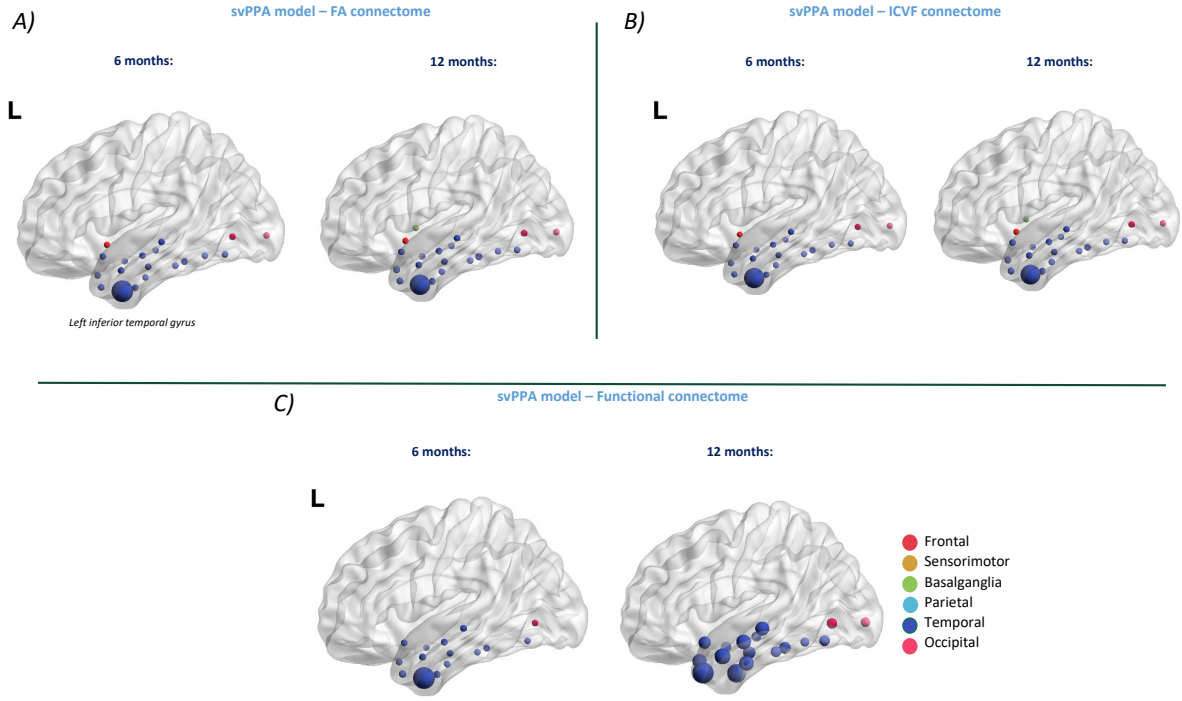

Figure 55:Sagittal view A) svPPA spreading prediction by NDM applied on FA connectome B) svPPA spreading prediction by NDM applied on ICVF connectome C) svPPA spreading prediction by NDM applied on functional connectome.

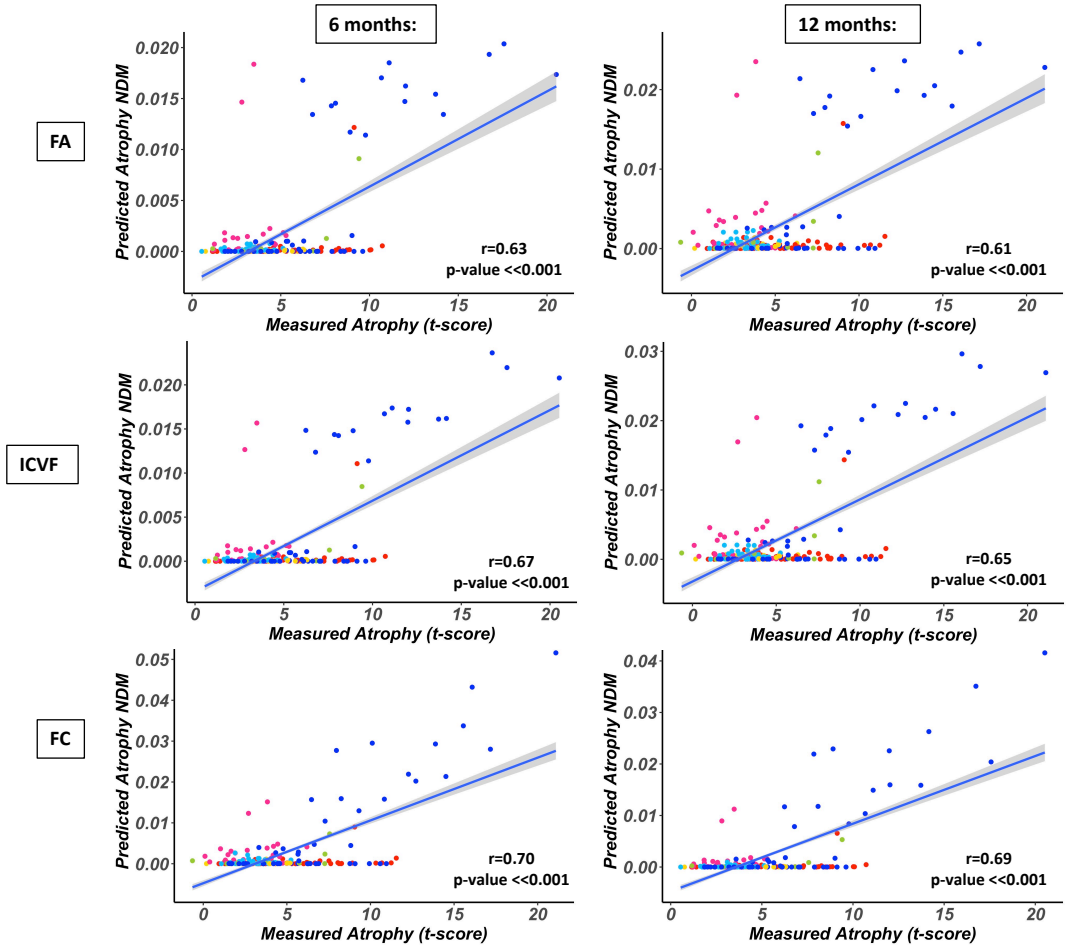

Figure 56: Correlations between atrophy t-score and atrophy predictions in svPPA patients on FA, ICVF and functional connectivity (FC) matrices are represented. On the left it is represented the correlation at 6 months, on the right at 12 months.

In MND, NDM predicted a pathology pattern involving predominantly sensorimotor lobe. Other brain areas involved in the spreading are frontal lobe, basal ganglia (thalamus, putamen, and caudate), parietal lobe and temporal lobe (hippocampus and superior temporal gyrus) (Figure 57).

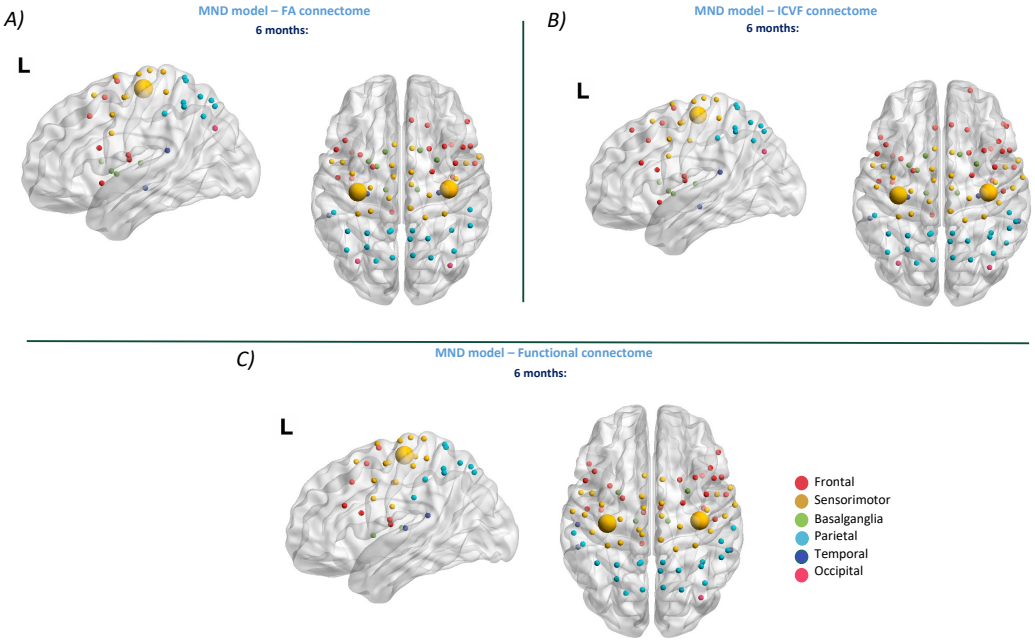

Figure 57: Saggital and transversal view A) MND spreading prediction by NDM applied on FA connectome B) MND spreading prediction by NDM applied on ICVF connectome C) MND spreading prediction by NDM applied on functional connectome

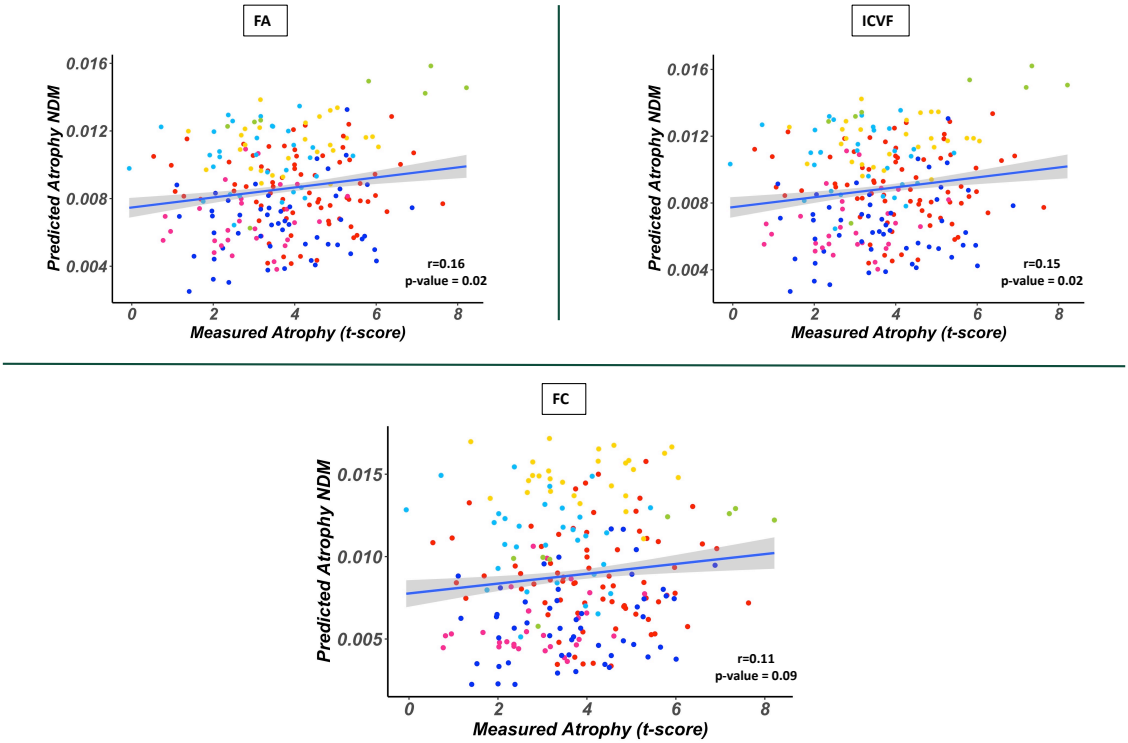

Figure 58 Correlations between atrophy t-score and atrophy predictions in MND patients on FA, ICVF and functional connectivity (FC) matrices are represented.

Moreover, the degree of atrophy predicted in each region by NDM in healthy young subjects was significantly positively associated with the empirical atrophy of the

FTLD patients ($p<0.05$), as shown in Figures 51, 54, 56 and 58. Overall, pathology diffusion predicted by NDM applied on ICVF connectome pointed out higher values of correlation related to atrophy predicted by NDM applied on FA maps (Figure 51, 54 and 56). In addition, NDM applied on functional matrices also revealed significant results. Particularly, in the case of svPPA patients, correlations with NDM applied on functional matrices demonstrated higher values of correlation in respect to NDM applied on FA and ICVF connectome. Considering bvFTD and nfvPPA patients, atrophy correlations with NDM applied on functional matrices showed similar results to NDM applied on FA connectome.

4.4 Structural-functional correlations

In all the patients, structural (measured by both FA and ICVF) was significantly positively related to functional connectivity (Figure 58 and 59).

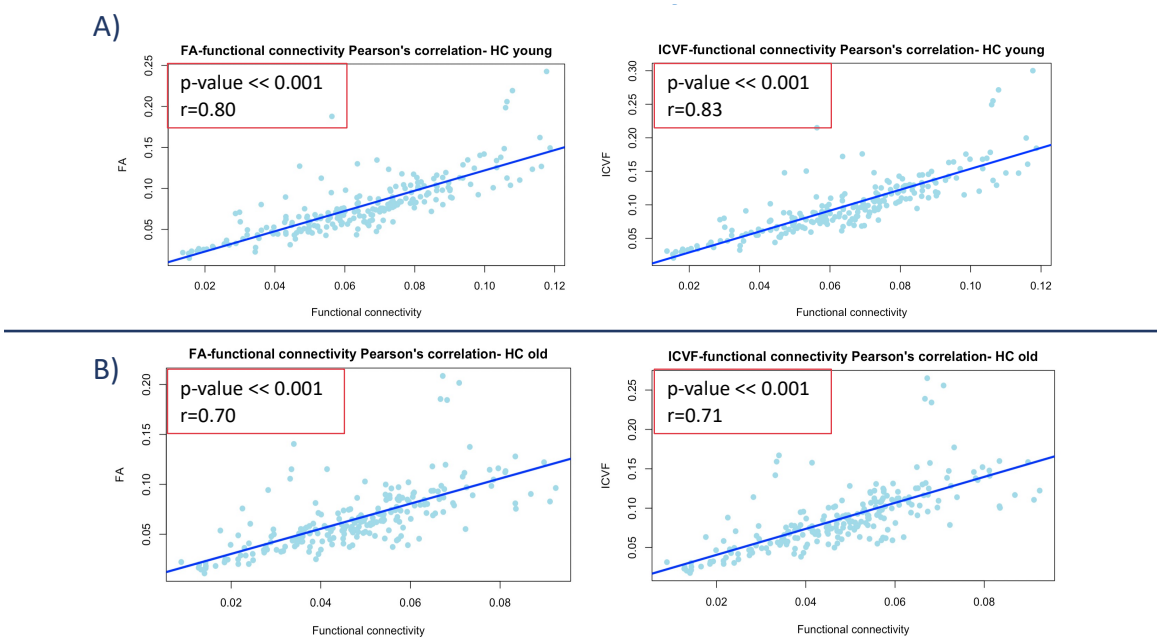

Figure 59: A) Pearson's correlation of structural-functional connectivity in young HC. B) Pearson's correlation of structural-functional connectivity in old HC. On the left there is represented the correlation between FA measures and functional connectivity, on the right ICVF measures and functional connectivity.

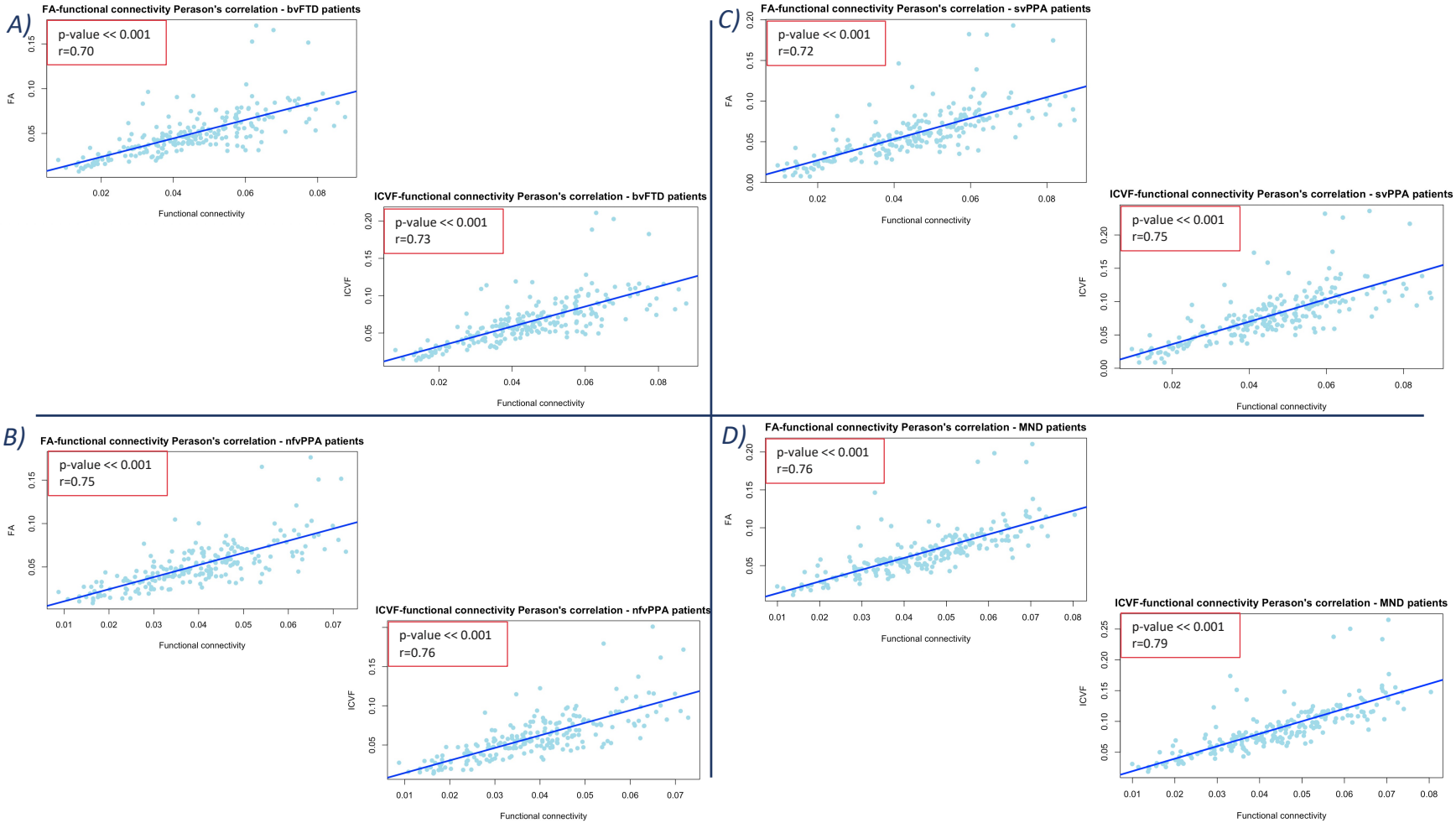

Figure 60: A) Pearson's correlation of structural-functional connectivity in bvFTD patients. B) Pearson's correlation of structural-functional connectivity in nfvPPA patients. C) Pearson's correlation of structural-functional connectivity in svPPA patients. D) Pearson's correlation of structural-functional connectivity in MND patients.

CHAPTER 5: DISCUSSION AND CONCLUSIONS

The present MRI study investigated alterations in structural and functional brain network in patients within the FTLD spectrum using connectome-analysis with advanced diffusion-weighted metrics. NODDI indices have been identified as clinically useful, highly specific biomarkers to distinguish FTLD syndromes. Benefits specifically appeared in the differentiation of svPPA patients from other groups. Moreover, a Network Diffusion Model (NDM) was developed to assess whether the progression of FTLD pathology over time might be modeled by a spreading process, originating from a single regional seed and then proceeding through the healthy structural connectome.

Clinical changes within the FTLD spectrum result in different patterns of brain network reorganization, using graph analysis and connectomics to analyze structural and functional brain networks. Neuroimaging research has recently been focused on structural and functional changes at a brain-system level rather than on network-level in specific brain areas. Such advanced technique, the so-called "connectome" analysis, has already been shown to be an effective way to monitor structural and functional rearrangement in different neurodegenerative disorders. There are many advantages of such analysis approach: (i) Complex network analysis promises to reliably quantify brain networks with a small number of neurobiologically meaningful and easily computable measures [180]; (ii) Network analysis allows to explore structural–functional connectivity relationship [181-183]; (iii) Comparisons of structural or functional network organization in case-control studies are likely to reveal connectivity abnormalities in neurological and psychiatric disorders [184-186]. In our work, connectome and graph analysis were performed in the early stage of diseases, highlighting the ability of connectome to detect brain alterations in the first phase of the disease. From this perspective, connectome analysis might be useful as biomarker to enhance prediction and to prevent prion-like spread.

Recent evidence suggests that the spreading of pathology occurs along neuronal pathways rather than simply as diffusion among neighboring cells, suggesting the idea that functional and structural connections between regions may significantly contribute to pathology propagation [127, 163]. Indeed, exploring the relationship between selective network vulnerability in healthy young controls and longitudinal

pathological progression in FTLD patients, it might be possible to provide information on how the pathology spread. This study provided an opportunity to identify biomarkers for FTLD syndromes progression and clinical trials for potential treatments. Firstly, biomarkers are very important in clinical longitudinal studies spanning from early pre-symptomatic disease through symptomatic stages. In this way, it might be interesting to detect how pathological events start, progress over time and how work with clinical symptoms. Biomarkers are also important in clinical trials. It has been demonstrated that disease-modifying therapies presented different efficacy during the course of the disease. Therapies are more effective during early pre-symptomatic or prodromal phase, before the manifestation of the neurodegeneration. Furthermore, the early accumulation of Tau and TDP-43 in FTLD might trigger the spread of cortical and subcortical pathology.

Results of the present study suggested that conventional DTI measures might be sensitive to highlight connections vulnerable in the FTLD spectrum. Overall, this study revealed that bvFTD patients showed the greatest structural impairment, compared to healthy controls, MND and svPPA patients, with a predominant damage in the fronto-temporo-parietal network, consistent with previous studies [138-141]. This finding supports the hypotheses that connectome architecture influences neurodegeneration, as network changes in bvFTD patients reflect their typical atrophy distribution, demonstrating that network structure shapes atrophy patterns [142, 187]. Afterwards, also nfvPPA patients demonstrated a widespread structural damage compared with healthy controls and MND, predominantly involving the left hemisphere (precentral gyrus, supplementary motor area and temporal lobe), as shown in previous studies [87, 115, 143]. Such neurodegenerative pattern supports the view of the left supplementary motor area as the epicenter of nfvPPA degenerative process, following by pathology spread in the inter-connected areas [188]. In contrasts, svPPA and MND patients did not show altered FA measure compared to other FTLD groups, suggesting that this metric is unable to distinguish between different types of connection alterations.

To our knowledge, this was the first study applying NODDI model to detect structural WM changes in FTLD spectrum using connectomics. Such model provided a better quantification of the extent of WM architecture deterioration in the FTLD spectrum, in terms of density and orientation dispersion, being more specific to individual tissue

microstructure [72, 189]. Indeed, ICVF demonstrated to be a clinically relevant biomarker more specific than FA to differentiate pathologies of FTLD spectrum. A decrease in FA may be brought on by a variety of tissue microstructural changes, including a decrease in neurite density, an increase in the dispersion of neurite orientation distribution [72, 190]. ICVF seems to overcome this issue, estimating neuronal density within intra-cellular compartment. In this study, the benefits emerged in the differentiation between svPPA patients and other groups. Indeed, graph analysis showed differences between svPPA patients and healthy controls and MND patients, in particular involving the temporal lobe. This brain region was identified as the most atrophic in svPPA patients in previous study [188, 191]. Moreover, NBS showed also a widespread decreased ICVF in nfvPPA patients compared to svPPA patients. In addition to NODDI specificity, also the implementation of FODs estimation algorithm contributes to obtain more specific indices, solving the issue of multiple crossing fibers within a single voxel [174, 192].

Moreover, ODI index was found altered in WM tracts. Specifically, considering that ODI measures the dispersion of fibers, we expect an increased ODI in patients, where there is a loss of directionality. Nevertheless, research on other neurological conditions, such as Multiple Sclerosis, showed that the degree of dispersion was estimated from only a small fraction of the tissue's signal, because axonal loss was present (as indicated by lower ICVF in patients). It may have led to numerical instability in the NODDI model fit [193, 194]. These findings suggested that WM loss could be represented by lower values of ODI.

Thanks to connectomics approach, a direct comparison between functional and structural connectivity is possible thanks to the common parcellating system and statistical methodology. However, only NBS analysis showed that bvFTD patients had a decreased functional strength compared to healthy controls, involving in particular the frontal, temporal and parietal lobe, in line with the current literature [101, 109, 148]. This finding is in line with the selective, early vulnerability of fronto-insular, prefrontal and temporal regions to frontotemporal lobar degeneration (FTLD) pathology [91]. Moreover, these regions are critical for social and emotional processing, task control and maintenance of social decorum, which represent common clinical features of bvFTD patients.

Conversely, functional connectivity graph analysis did not show key results such as structural connectivity, indicating that structural changes may occur earlier in the course of the disease than functional network impairments. This observation is consistent with the previous observations in other neurodegenerative disorders [147, 195].

Concerning NDM results, it was possible to explain regional pattern of FTLD pathologies. These findings are consistent with the possibility that a single misfolded protein might cause the spreading of pathology affecting several brain regions [162, 196]. In the case of bvFTD patients, predictive maps showed a pathology spread consistent with the four stages defined by Brettschneider and colleagues [33]. In detail, the first stage was characterized by widespread WM alterations in the orbital gyri, rectus gyrus, and amygdala, as we can see in predictive maps (Figure 52, and 53) where at 6 months there is an early spread to the frontal lobe. Considering the second stage, connectivity appeared altered in the middle frontal, anterior cingulate, anteromedial temporal lobe, superior, and medial temporal gyri, as showed in the predictive maps, where the involvement of these areas is more lateralized (right hemisphere). Whereas the third and fourth pattern were not yet involved in our predictive maps. Usually, in svPPA patients, atrophy initially appears in left hemisphere and progressively spreads. Indeed, the left inferior temporal lobe was identified as svPPA seed. Literature showed that earliest changes include GM loss in the inferior temporal and fusiform gyri, then progression of disease leads to involvement of the middle and inferior frontal gyri, posterior temporal gyrus and occipital lobe [36-38]. Our maps showed this pattern of spreading, but we cannot see a contralateral spread in the right hemisphere. In nfvPPA patients, peak of atrophy was identified in the left supplementary motor area, and then spread in the inter-connected areas, involving left frontal operculum, premotor area, anterior insula, and superior and transverse temporal gyri. nfvPPA predictive maps showed an initial lateralized spread, in particular in the left frontal, superior temporal lobes and insula, involving after contralateral areas as we expected [36, 38, 39]. Regarding MND patients spreading model showed typical pattern of the early stages of pathology [34], involving in particular frontal, sensorimotor and parietal lobes. Whereas the last stage of TDP-43 progression is not yet involved, indeed very few areas of this stage are reached (temporal superior gyrus and hippocampus).

The model of bvFTD progression showed a bilateral spread of pathology, compared to svPPA patients whose pathology seed is more lateralized in the left hemisphere. nfvPPA and MND, whose seed was in a medial brain region, showed a more diffuse damage compared to other groups.

The strong correlations that we found with the empirical atrophy support the hypothesis that the healthy architecture of the structural connectome might influence the spatio-temporal progression of atrophy in each FTLD variant. The accuracy values of each model also showed that ICVF has greater specificity than FA to model pathology spread. NDM showed significant results also applied on functional matrices. For this reason, the significant correlation between structural and functional connectivity suggested that structural and functional measures might be combined in a single model to predict the pathology spreading where both of them demonstrate higher strength connectivity in the network to obtain more relevant results.

Limitations. Our results are encouraging; however, they should be confirmed in a larger sample and, more importantly, in path-proven cases. Moreover, the lack of a reference standard for the regional parcellation of brain MR imaging can markedly affect graph theoretical metrics [166, 197] so that comparisons with previous MRI studies using different approaches can be challenging. In order to avoid a regional atrophy influence, MRI data were registered to and masked with GM maps; nonetheless, a potential partial volume effect on these results cannot be completely ruled out. Additionally, it has been noted that even the smallest head movements (on a submillimeter scale) can throw off functional connectivity analyses [198-201]. As a result, image preprocessing and motion correction steps have a significant impact on the degree and relative magnitude of network-level functional connectivity. Furthermore, the NDM is a first-order, linear model of diffuse spread that assumes the structural connection network stays constant during the progression of the illness. Even though all neurodegenerative disorders result in abnormal structural connections, constant connectomes like the ones used here typically do not significantly reduce the model's predictive power [202]. The next stage to better understand the atrophy spread mechanism should be non-linear active modeling.

Conclusions. Overall, connectomics and graph analysis might be useful biomarkers to distinguish different clinical syndromes within the FTLD spectrum. Importantly, connectome study was carried out in patients in the early phase of the disease, highlighting the potential of these advanced methods when the clinical diagnosis is more challenging. Moreover, connectome-analysis based on advanced diffusion-weighted models (i.e., NODDI) may be useful to evaluate structural disruptions with greater differentiation among FTLD spectrum compared to diffusion-tensor derived measures. Finally, the implementation of NDM to cross-sectional structural connectome data is a valuable tool to predict future atrophy patterns and pathology spreading in the main variants of the FTLD spectrum.

Appendix

MATLAB SCRIPTS NDM:

```
clear all
close all
clc

%% Network Diffusion Model (NDM)
%% Variables initialization
global x0
global L
global t
global beta

brain_regions=220;
C=load('connectivity_HCyoung_FA.mat');
C=C.connectivity;% Connectome
C(isnan(C))=0;
D=diag(sum(C));   % diagonal matrix whose elements are degree of
each node: sum of weighted connection from the node.
I=eye(brain_regions);  % identity matrix
beta=1; % diffusivity: higher value --> rapidly pathology, lower
value --> slower pathology
t=[0,6,12,18,24]; % time points


%% Laplacian Graph: symmetric and normalized by the sum of weigth of
each node

L=I-(D^(-1/2)*C*D^(-1/2));

%% Seed definition
x0=zeros(brain_regions,1); %initial condition
seeds=[1:10];
x0(seeds)=1;

%% Eigenvector solution:

[eig_vec,A]=eig(L);
eig_val=diag(A);

xt=NDM(eig_vec,eig_val,x0,t,beta); % NDM prediction
```

```
function [xt]=NDM(eig_vect,eig_val,x0,t,beta)
% NDM solution → Eigenvector decomposition
% input: eig_vect: eigen vectors of graph laplacian
%        eig_val: eigenvalues
%        t: time points
%        beta: diffusion cofficient

x0 = x0(:);
x0V = eig_vect'*x0;
```

```
xt=[];

%predictions for each time-point
for i=1:length(t)
   P = x0V.*exp(-eig_val*beta*t(i));
   xt(:,i) = eig_vect*P;
end
```

Acknowledgments

Ringrazio il Professor Filippi e la Professoressa Agosta per avermi dato la grande opportunità di far parte di questo progetto e per avermi inserito in questo gruppo di lavoro interdisciplinare, dandomi la possibilità di comprendere l'importanza del lavoro di squadra.
Grazie al Professor Molinari per aver acconsentito a seguirmi in questo progetto di tesi e per avermi trasmesso la sua passione in tutti i suoi insegnamenti durante questi anni di università.

Un enorme grazie a Silvia e Camilla, per avermi sostenuta, guidata e formata in questi ultimi mesi. A Silvia, per esser stata molto più di una semplice tutor, per avermi fatto capire quanto sia importante avere passione e precisione in ciò che si fa. Grazie per essere stata un supporto costante, per avermi capita e spronata. A Camilla, per essere sempre stata pronta a risollevarmi e confortami, ma soprattutto per aver avuto la capacità di trasmettermi ogni giorno il buon umore. A voi, Grazie! Vi porto nel cuore.

A tutte le persone del CAB, chi c'è ancora e chi c'è stato, che in un modo o nell'altro hanno contribuito ad alleggerire e rendere speciali questi ultimi mesi. Siete un gruppo meraviglioso e sono orgogliosa di averne fatto parte.

Alla mia famiglia, per essere sempre il mio posto sicuro nel mondo.

Ad Andrea, per il continuo supporto (e sopportazione), per l'immenso amore che mi dimostri ogni giorno e per essere, senza ombra di dubbio, il mio migliore amico.

Ai compagni di corso. Un grazie speciale a Martina, per essere stata una certezza fin dal primo istante, per essere stata un supporto ogni giorno, anche a km di distanza. A Diletta, la sintonia che c'è stata tra di noi fin dal primo giorno è stato qualcosa di speciale, grazie per aver sempre creduto in me e per esser stata un'ottima compagna di lamentele.

Ai miei amici, quelli di una vita, senza di voi niente sarebbe stato lo stesso. Grazie per le risate e per gli infiniti momenti di spensieratezza. Vi voglio bene.

Alle mie coinquiline, per essere state le mie sorelle maggiori, per non avermi mai fatto sentire sola, per le lunghe chiacchierate e le immense risate.

Bibliography

1. Meeter, L.H., et al., Imaging and fluid biomarkers in frontotemporal dementia. Nat Rev Neurol, 2017. 13(7): p. 406-419.
2. Seltman, R.E. and B.R. Matthews, Frontotemporal lobar degeneration: epidemiology, pathology, diagnosis and management. CNS Drugs, 2012. 26(10): p. 841-70.
3. Bang, J., S. Spina, and B.L. Miller, Frontotemporal dementia. Lancet, 2015. 386(10004): p. 1672-82.
4. Lashley, T., et al., Review: an update on clinical, genetic and pathological aspects of frontotemporal lobar degenerations. Neuropathol Appl Neurobiol, 2015. 41(7): p. 858-81.
5. Young, J.J., et al., Frontotemporal dementia: latest evidence and clinical implications. Ther Adv Psychopharmacol, 2018. 8(1): p. 33-48.
6. Onyike, C.U. and J. Diehl-Schmid, The epidemiology of frontotemporal dementia. Int Rev Psychiatry, 2013. 25(2): p. 130-7.
7. Knopman, D.S. and R.O. Roberts, Estimating the number of persons with frontotemporal lobar degeneration in the US population. J Mol Neurosci, 2011. 45(3): p. 330-5.
8. Logroscino, G., et al., Incidence of frontotemporal lobar degeneration in Italy: The Salento-Brescia Registry study. Neurology, 2019. 92(20): p. e2355-e2363.
9. Onyike, C.U., What is the life expectancy in frontotemporal lobar degeneration? Neuroepidemiology, 2011. 37(3-4): p. 166-7.
10. Hu, W.T. and M. Grossman, TDP-43 and frontotemporal dementia. Curr Neurol Neurosci Rep, 2009. 9(5): p. 353-8.
11. Nonaka, T., et al., Prion-like properties of pathological TDP-43 aggregates from diseased brains. Cell Rep, 2013. 4(1): p. 124-34.
12. Sieben, A., et al., The genetics and neuropathology of frontotemporal lobar degeneration. Acta Neuropathol, 2012. 124(3): p. 353-72.
13. Mackenzie, I.R., et al., Nomenclature for neuropathologic subtypes of frontotemporal lobar degeneration: consensus recommendations. Acta Neuropathol, 2009. 117(1): p. 15-8.
14. Mackenzie, I.R., R. Rademakers, and M. Neumann, TDP-43 and FUS in amyotrophic lateral sclerosis and frontotemporal dementia. Lancet Neurol, 2010. 9(10): p. 995-1007.
15. Hock, E.M. and M. Polymenidou, Prion-like propagation as a pathogenic principle in frontotemporal dementia. J Neurochem, 2016. 138 Suppl 1: p. 163-83.
16. Neve, R.L., et al., Human chromosome 21-encoded cDNA clones. Gene, 1986. 49(3): p. 361-9.
17. Goedert, M., et al., Multiple isoforms of human microtubule-associated protein tau: sequences and localization in neurofibrillary tangles of Alzheimer's disease. Neuron, 1989. 3(4): p. 519-26.
18. Mandelkow, E.M. and E. Mandelkow, Biochemistry and cell biology of tau protein in neurofibrillary degeneration. Cold Spring Harb Perspect Med, 2012. 2(7): p. a006247.
19. Fontana, F., K. Siva, and M.A. Denti, A network of RNA and protein interactions in Fronto Temporal Dementia. Front Mol Neurosci, 2015. 8: p. 9.
20. Lee, H.G., et al., Tau phosphorylation in Alzheimer's disease: pathogen or protector? Trends Mol Med, 2005. 11(4): p. 164-9.
21. Zhang, Y., et al., Tauopathies: new perspectives and challenges. Mol Neurodegener, 2022. 17(1): p. 28.
22. Warraich, S.T., et al., TDP-43: a DNA and RNA binding protein with roles in neurodegenerative diseases. Int J Biochem Cell Biol, 2010. 42(10): p. 1606-9.
23. Buratti, E. and F.E. Baralle, TDP-43: gumming up neurons through protein-protein and protein-RNA interactions. Trends Biochem Sci, 2012. 37(6): p. 237-47.

24. King, O.D., A.D. Gitler, and J. Shorter, The tip of the iceberg: RNA-binding proteins with prion-like domains in neurodegenerative disease. Brain Res, 2012. 1462: p. 61-80.
25. Ayala, Y.M., et al., Structural determinants of the cellular localization and shuttling of TDP-43. J Cell Sci, 2008. 121(Pt 22): p. 3778-85.
26. Scotter, E.L., H.J. Chen, and C.E. Shaw, TDP-43 Proteinopathy and ALS: Insights into Disease Mechanisms and Therapeutic Targets. Neurotherapeutics, 2015. 12(2): p. 352-63.
27. Winton, M.J., et al., Disturbance of nuclear and cytoplasmic TAR DNA-binding protein (TDP-43) induces disease-like redistribution, sequestration, and aggregate formation. J Biol Chem, 2008. 283(19): p. 13302-9.
28. Ayala, Y.M., et al., TDP-43 regulates its mRNA levels through a negative feedback loop. EMBO J, 2011. 30(2): p. 277-88.
29. Xu, Z.S., Does a loss of TDP-43 function cause neurodegeneration? Mol Neurodegener, 2012. 7: p. 27.
30. Neumann, M., Molecular neuropathology of TDP-43 proteinopathies. Int J Mol Sci, 2009. 10(1): p. 232-46.
31. Ling, S.C., M. Polymenidou, and D.W. Cleveland, Converging mechanisms in ALS and FTD: disrupted RNA and protein homeostasis. Neuron, 2013. 79(3): p. 416-38.
32. Mackenzie, I.R., et al., Novel types of frontotemporal lobar degeneration: beyond tau and TDP-43. J Mol Neurosci, 2011. 45(3): p. 402-8.
33. Brettschneider, J., et al., Sequential distribution of pTDP-43 pathology in behavioral variant frontotemporal dementia (bvFTD). Acta Neuropathol, 2014. 127(3): p. 423-439.
34. Brettschneider, J., et al., Stages of pTDP-43 pathology in amyotrophic lateral sclerosis. Ann Neurol, 2013. 74(1): p. 20-38.
35. Schmidt, R., et al., Simulating disease propagation across white matter connectome reveals anatomical substrate for neuropathology staging in amyotrophic lateral sclerosis. Neuroimage, 2016. 124(Pt A): p. 762-769.
36. Rohrer, J.D., et al., Patterns of cortical thinning in the language variants of frontotemporal lobar degeneration. Neurology, 2009. 72(18): p. 1562-9.
37. Gordon, E., J.D. Rohrer, and N.C. Fox, Advances in neuroimaging in frontotemporal dementia. J Neurochem, 2016. 138 Suppl 1: p. 193-210.
38. Rogalski, E., et al., Progression of language decline and cortical atrophy in subtypes of primary progressive aphasia. Neurology, 2011. 76(21): p. 1804-10.
39. Mandelli, M.L., et al., Healthy brain connectivity predicts atrophy progression in non-fluent variant of primary progressive aphasia. Brain, 2016. 139(Pt 10): p. 2778-2791.
40. Rascovsky, K., et al., Sensitivity of revised diagnostic criteria for the behavioural variant of frontotemporal dementia. Brain, 2011. 134: p. 2456-2477.
41. Rohrer, J.D., Behavioural variant frontotemporal dementia--defining genetic and pathological subtypes. J Mol Neurosci, 2011. 45(3): p. 583-8.
42. Gorno-Tempini, M.L., et al., Classification of primary progressive aphasia and its variants. Neurology, 2011. 76(11): p. 1006-14.
43. Norris, F., et al., Onset, natural history and outcome in idiopathic adult motor neuron disease. J Neurol Sci, 1993. 118(1): p. 48-55.
44. Talbot, K., Motor neurone disease. Postgrad Med J, 2002. 78(923): p. 513-9.
45. Swinnen, B. and W. Robberecht, The phenotypic variability of amyotrophic lateral sclerosis. Nat Rev Neurol, 2014. 10(11): p. 661-70.
46. Brooks, B.R., et al., El Escorial revisited: revised criteria for the diagnosis of amyotrophic lateral sclerosis. Amyotroph Lateral Scler Other Motor Neuron Disord, 2000. 1(5): p. 293-9.
47. Garg, N., et al., Differentiating lower motor neuron syndromes. J Neurol Neurosurg Psychiatry, 2017. 88(6): p. 474-483.

48. Gordon, P.H., et al., The natural history of primary lateral sclerosis. Neurology, 2006. 66(5): p. 647-653.
49. Riedl, L., et al., Frontotemporal lobar degeneration: current perspectives. Neuropsychiatr Dis Treat, 2014. 10: p. 297-310.
50. Barton, C., et al., Non-pharmacological Management of Behavioral Symptoms in Frontotemporal and Other Dementias. Curr Neurol Neurosci Rep, 2016. 16(2): p. 14.
51. Teri, L., et al., Training community consultants to help family members improve dementia care: A randomized controlled trial. Gerontologist, 2005. 45(6): p. 802-811.
52. Gitlin, L.N., H.C. Kales, and C.G. Lyketsos, Nonpharmacologic Management of Behavioral Symptoms in Dementia. Jama-Journal of the American Medical Association, 2012. 308(19): p. 2020-2029.
53. Jadhav, S., et al., A walk through tau therapeutic strategies. Acta Neuropathol Commun, 2019. 7(1): p. 22.
54. Ljubenkov, P.A. and A.L. Boxer, FTLD Treatment: Current Practice and Future Possibilities. Adv Exp Med Biol, 2021. 1281: p. 297-310.
55. Yanamandra, K., et al., Anti-tau antibodies that block tau aggregate seeding in vitro markedly decrease pathology and improve cognition in vivo. Neuron, 2013. 80(2): p. 402-414.
56. Lauterbur, P.C., 1973. Image formation by induced local interactions: examples employing nuclear magnetic resonance, in A Century of Nature, G. Laura and L. Tim, Editors. 2010, University of Chicago Press: Chicago. p. 196-200.
57. Damadian, R., Tumor detection by nuclear magnetic resonance. Science, 1971. 171(3976): p. 1151-3.
58. Ghadimi, M. and A. Sapra, Magnetic Resonance Imaging Contraindications, in StatPearls. 2022: Treasure Island (FL).
59. Agosta, F., S. Galantucci, and M. Filippi, Advanced magnetic resonance imaging of neurodegenerative diseases. Neurol Sci, 2017. 38(1): p. 41-51.
60. Chavhan, G.B., et al., Principles, techniques, and applications of T2*-based MR imaging and its special applications. Radiographics, 2009. 29(5): p. 1433-49.
61. Stejskal, E.O. and J.E. Tanner, Spin Diffusion Measurements: Spin Echoes in the Presence of a Time-Dependent Field Gradient. The Journal of Chemical Physics, 1965. 42(1): p. 288-292.
62. Mori, S. and J. Zhang, Principles of diffusion tensor imaging and its applications to basic neuroscience research. Neuron, 2006. 51(5): p. 527-39.
63. Alexander, A.L., et al., Diffusion tensor imaging of the brain. Neurotherapeutics, 2007. 4(3): p. 316-29.
64. Jahn, A., We followed the AFNI preprocessing pipeline as outlined in Andy's Brain Book. 2022.
65. Li, Y. and W. Zhang, Quantitative evaluation of diffusion tensor imaging for clinical management of glioma. Neurosurg Rev, 2020. 43(3): p. 881-891.
66. Vasconcelos, L.G., et al., Diffusion tensor imaging for Alzheimer's disease: A review of concepts and potential clinical applicability. Dement Neuropsychol, 2009. 3(4): p. 268-274.
67. Thiebaut de Schotten, M., et al., From Phineas Gage and Monsieur Leborgne to H.M.: Revisiting Disconnection Syndromes. Cereb Cortex, 2015. 25(12): p. 4812-27.
68. Zhang, F., et al., Quantitative mapping of the brain's structural connectivity using diffusion MRI tractography: A review. Neuroimage, 2022. 249: p. 118870.
69. Fornito, A., A. Zalesky, and M. Breakspear, Graph analysis of the human connectome: promise, progress, and pitfalls. Neuroimage, 2013. 80: p. 426-44.
70. Broad, R.J., et al., Neurite orientation and dispersion density imaging (NODDI) detects cortical and corticospinal tract degeneration in ALS. J Neurol Neurosurg Psychiatry, 2019. 90(4): p. 404-411.

71. Tariq, M., et al., Bingham-NODDI: Mapping anisotropic orientation dispersion of neurites using diffusion MRI. Neuroimage, 2016. 133: p. 207-223.
72. Zhang, H., et al., NODDI: practical in vivo neurite orientation dispersion and density imaging of the human brain. Neuroimage, 2012. 61(4): p. 1000-16.
73. Vos, S.B., et al., The influence of complex white matter architecture on the mean diffusivity in diffusion tensor MRI of the human brain. Neuroimage, 2012. 59(3): p. 2208-16.
74. Winston, G.P., The physical and biological basis of quantitative parameters derived from diffusion MRI. Quant Imaging Med Surg, 2012. 2(4): p. 254-65.
75. Deligianni, F., et al., NODDI and Tensor-Based Microstructural Indices as Predictors of Functional Connectivity. PLoS One, 2016. 11(4): p. e0153404.
76. Gore, J.C., Principles and practice of functional MRI of the human brain. J Clin Invest, 2003. 112(1): p. 4-9.
77. Ogawa, S., et al., Brain magnetic resonance imaging with contrast dependent on blood oxygenation. Proc Natl Acad Sci U S A, 1990. 87(24): p. 9868-72.
78. Ogawa, S., et al., Oxygenation-sensitive contrast in magnetic resonance image of rodent brain at high magnetic fields. Magn Reson Med, 1990. 14(1): p. 68-78.
79. Barth, M. and B.A. Poser, Advances in High-Field BOLD fMRI. Materials (Basel), 2011. 4(11): p. 1941-1955.
80. Biswal, B., et al., Functional connectivity in the motor cortex of resting human brain using echo-planar MRI. Magn Reson Med, 1995. 34(4): p. 537-41.
81. Lee, M.H., C.D. Smyser, and J.S. Shimony, Resting-state fMRI: a review of methods and clinical applications. AJNR Am J Neuroradiol, 2013. 34(10): p. 1866-72.
82. Fox, M.D. and M. Greicius, Clinical applications of resting state functional connectivity. Front Syst Neurosci, 2010. 4: p. 19.
83. Menon, V., Large-scale brain networks and psychopathology: a unifying triple network model. Trends Cogn Sci, 2011. 15(10): p. 483-506.
84. Raichle, M.E., et al., A default mode of brain function. Proc Natl Acad Sci U S A, 2001. 98(2): p. 676-82.
85. Hafkemeijer, A., J. van der Grond, and S.A. Rombouts, Imaging the default mode network in aging and dementia. Biochim Biophys Acta, 2012. 1822(3): p. 431-41.
86. Day, G.S., et al., Salience network resting-state activity: prediction of frontotemporal dementia progression. JAMA Neurol, 2013. 70(10): p. 1249-53.
87. Mandelli, M.L., et al., Altered topology of the functional speech production network in non-fluent/agrammatic variant of PPA. Cortex, 2018. 108: p. 252-264.
88. Schroeter, M.L., et al., Towards a nosology for frontotemporal lobar degenerations-a meta-analysis involving 267 subjects. Neuroimage, 2007. 36(3): p. 497-510.
89. Pan, P.L., et al., Gray matter atrophy in behavioral variant frontotemporal dementia: a meta-analysis of voxel-based morphometry studies. Dement Geriatr Cogn Disord, 2012. 33(2-3): p. 141-8.
90. Du, A.T., et al., Different regional patterns of cortical thinning in Alzheimer's disease and frontotemporal dementia. Brain, 2007. 130(Pt 4): p. 1159-66.
91. Seeley, W.W., et al., Frontal paralimbic network atrophy in very mild behavioral variant frontotemporal dementia. Arch Neurol, 2008. 65(2): p. 249-55.
92. Agosta, F., et al., Neuroimaging findings in frontotemporal lobar degeneration spectrum of disorders. Cortex, 2012. 48(4): p. 389-413.
93. Diehl-Schmid, J., et al., Imaging frontotemporal lobar degeneration. Curr Neurol Neurosci Rep, 2014. 14(10): p. 489.
94. Seeley, W.W., et al., The natural history of temporal variant frontotemporal dementia. Neurology, 2005. 64(8): p. 1384-90.
95. Agosta, F., et al., Voxel-based morphometry study of brain volumetry and diffusivity in amyotrophic lateral sclerosis patients with mild disability. Hum Brain Mapp, 2007. 28(12): p. 1430-8.

96. Turner, M.R., et al., Volumetric cortical loss in sporadic and familial amyotrophic lateral sclerosis. Amyotroph Lateral Scler, 2007. 8(6): p. 343-7.
97. Kassubek, J., A.C. Ludolph, and H.P. Muller, Neuroimaging of motor neuron diseases. Ther Adv Neurol Disord, 2012. 5(2): p. 119-27.
98. Mezzapesa, D.M., et al., Whole-brain and regional brain atrophy in amyotrophic lateral sclerosis. AJNR Am J Neuroradiol, 2007. 28(2): p. 255-9.
99. Abrahams, S., et al., Frontotemporal white matter changes in amyotrophic lateral sclerosis. J Neurol, 2005. 252(3): p. 321-31.
100. Whitwell, J.L., et al., Gray and white matter water diffusion in the syndromic variants of frontotemporal dementia. Neurology, 2010. 74(16): p. 1279-87.
101. Whitwell, J.L. and K.A. Josephs, Recent advances in the imaging of frontotemporal dementia. Curr Neurol Neurosci Rep, 2012. 12(6): p. 715-23.
102. Agosta, F., et al., White matter damage in frontotemporal lobar degeneration spectrum. Cereb Cortex, 2012. 22(12): p. 2705-14.
103. Zhang, Y., et al., MRI signatures of brain macrostructural atrophy and microstructural degradation in frontotemporal lobar degeneration subtypes. J Alzheimers Dis, 2013. 33(2): p. 431-44.
104. Tu, S., et al., Divergent Longitudinal Propagation of White Matter Degradation in Logopenic and Semantic Variants of Primary Progressive Aphasia. J Alzheimers Dis, 2016. 49(3): p. 853-61.
105. Lam, B.Y., et al., Longitudinal white matter changes in frontotemporal dementia subtypes. Hum Brain Mapp, 2014. 35(7): p. 3547-57.
106. McMillan, C.T., et al., White matter imaging helps dissociate tau from TDP-43 in frontotemporal lobar degeneration. J Neurol Neurosurg Psychiatry, 2013. 84(9): p. 949-55.
107. Muller, H.P., et al., A large-scale multicentre cerebral diffusion tensor imaging study in amyotrophic lateral sclerosis. J Neurol Neurosurg Psychiatry, 2016. 87(6): p. 570-9.
108. Agosta, F., et al., Resting state functional connectivity alterations in primary lateral sclerosis. Neurobiol Aging, 2014. 35(4): p. 916-25.
109. Agosta, F., et al., MRI signatures of the frontotemporal lobar degeneration continuum. Hum Brain Mapp, 2015. 36(7): p. 2602-14.
110. Dopper, E.G., et al., Structural and functional brain connectivity in presymptomatic familial frontotemporal dementia. Neurology, 2014. 83(2): p. e19-26.
111. Filippi, M., et al., Functional network connectivity in the behavioral variant of frontotemporal dementia. Cortex, 2013. 49(9): p. 2389-401.
112. Seeley, W.W., J. Zhou, and E.J. Kim, Frontotemporal dementia: what can the behavioral variant teach us about human brain organization? Neuroscientist, 2012. 18(4): p. 373-85.
113. Farb, N.A., et al., Abnormal network connectivity in frontotemporal dementia: evidence for prefrontal isolation. Cortex, 2013. 49(7): p. 1856-73.
114. Battistella, G., et al., Differential intrinsic functional connectivity changes in semantic variant primary progressive aphasia. Neuroimage Clin, 2019. 22: p. 101797.
115. Reyes, P., et al., Functional Connectivity Changes in Behavioral, Semantic, and Nonfluent Variants of Frontotemporal Dementia. Behav Neurol, 2018. 2018: p. 9684129.
116. Collins, J.A., et al., Focal temporal pole atrophy and network degeneration in semantic variant primary progressive aphasia. Brain, 2017. 140(2): p. 457-471.
117. Mohammadi, B., et al., Changes of resting state brain networks in amyotrophic lateral sclerosis. Exp Neurol, 2009. 217(1): p. 147-53.
118. Agosta, F., et al., Divergent brain network connectivity in amyotrophic lateral sclerosis. Neurobiol Aging, 2013. 34(2): p. 419-27.

119. Luo, C., et al., Patterns of spontaneous brain activity in amyotrophic lateral sclerosis: a resting-state FMRI study. PLoS One, 2012. 7(9): p. e45470.
120. Agosta, F., et al., Sensorimotor functional connectivity changes in amyotrophic lateral sclerosis. Cereb Cortex, 2011. 21(10): p. 2291-8.
121. Filippi, M., et al., Assessment of system dysfunction in the brain through MRI-based connectomics. Lancet Neurol, 2013. 12(12): p. 1189-99.
122. van den Heuvel, M.P. and O. Sporns, A cross-disorder connectome landscape of brain dysconnectivity. Nat Rev Neurosci, 2019. 20(7): p. 435-446.
123. van den Heuvel, M.P. and H.E. Hulshoff Pol, Exploring the brain network: a review on resting-state fMRI functional connectivity. Eur Neuropsychopharmacol, 2010. 20(8): p. 519-34.
124. Fallon, J., et al., Timescales of spontaneous fMRI fluctuations relate to structural connectivity in the brain. Netw Neurosci, 2020. 4(3): p. 788-806.
125. Sporns, O., G. Tononi, and R. Kotter, The human connectome: A structural description of the human brain. PLoS Comput Biol, 2005. 1(4): p. e42.
126. Hagmann, P., FROM DIFFUSION MRI TO BRAIN CONNECTOMICS. 2005, ÉCOLE POLYTECHNIQUE FÉDÉRALE DE LAUSANNE.
127. Raj, A., A. Kuceyeski, and M. Weiner, A network diffusion model of disease progression in dementia. Neuron, 2012. 73(6): p. 1204-15.
128. Sporns, O., Graph theory methods: applications in brain networks. Dialogues Clin Neurosci, 2018. 20(2): p. 111-121.
129. Verstraete, E., et al., Structural brain network imaging shows expanding disconnection of the motor system in amyotrophic lateral sclerosis. Hum Brain Mapp, 2014. 35(4): p. 1351-61.
130. Farahani, F.V., W. Karwowski, and N.R. Lighthall, Application of Graph Theory for Identifying Connectivity Patterns in Human Brain Networks: A Systematic Review. Front Neurosci, 2019. 13: p. 585.
131. Fornito, A., A. Zalesky, and M. Breakspear, The connectomics of brain disorders. Nat Rev Neurosci, 2015. 16(3): p. 159-72.
132. Telesford, Q.K., et al., The brain as a complex system: using network science as a tool for understanding the brain. Brain Connect, 2011. 1(4): p. 295-308.
133. van den Heuvel, M.P. and O. Sporns, Rich-club organization of the human connectome. J Neurosci, 2011. 31(44): p. 15775-86.
134. Bullmore, E. and O. Sporns, Complex brain networks: graph theoretical analysis of structural and functional systems. Nat Rev Neurosci, 2009. 10(3): p. 186-98.
135. Watts, D.J. and S.H. Strogatz, Collective dynamics of 'small-world' networks. Nature, 1998. 393(6684): p. 440-2.
136. Arnemann, K.L., et al., Functional brain network modularity predicts response to cognitive training after brain injury. Neurology, 2015. 84(15): p. 1568-74.
137. Zalesky, A., A. Fornito, and E.T. Bullmore, Network-based statistic: identifying differences in brain networks. Neuroimage, 2010. 53(4): p. 1197-207.
138. Daianu, M., et al., Disrupted rich club network in behavioral variant frontotemporal dementia and early-onset Alzheimer's disease. Hum Brain Mapp, 2016. 37(3): p. 868-83.
139. Nigro, S., et al., Brain Structural Covariance Networks in Behavioral Variant of Frontotemporal Dementia. Brain Sci, 2021. 11(2).
140. Nigro, S., et al., The Role of Graph Theory in Evaluating Brain Network Alterations in Frontotemporal Dementia. Front Neurol, 2022. 13: p. 910054.
141. Vijverberg, E.G.B., et al., Gray matter network differences between behavioral variant frontotemporal dementia and Alzheimer's disease. Neurobiol Aging, 2017. 50: p. 77-86.
142. Shafiei, G., et al., Network structure and transcriptomic vulnerability shape atrophy in frontotemporal dementia. Brain, 2022.

143. Reyes, P.A., et al., Networks Disrupted in Linguistic Variants of Frontotemporal Dementia. Front Neurol, 2019. 10: p. 903.
144. Nigro, S., et al., Altered structural brain networks in linguistic variants of frontotemporal dementia. Brain Imaging Behav, 2022. 16(3): p. 1113-1122.
145. Fortanier, E., et al., Structural Connectivity Alterations in Amyotrophic Lateral Sclerosis: A Graph Theory Based Imaging Study. Front Neurosci, 2019. 13: p. 1044.
146. Verstraete, E., et al., Impaired structural motor connectome in amyotrophic lateral sclerosis. PLoS One, 2011. 6(9): p. e24239.
147. Basaia, S., et al., Structural and functional brain connectome in motor neuron diseases: A multicenter MRI study. Neurology, 2020. 95(18): p. e2552-e2564.
148. Filippi, M., et al., Brain network connectivity differs in early-onset neurodegenerative dementia. Neurology, 2017. 89(17): p. 1764-1772.
149. Agosta, F., et al., Brain network connectivity assessed using graph theory in frontotemporal dementia. Neurology, 2013. 81(2): p. 134-43.
150. Agosta, F., et al., Disrupted brain connectome in semantic variant of primary progressive aphasia. Neurobiol Aging, 2014. 35(11): p. 2646-2655.
151. Geevasinga, N., et al., Brain functional connectome abnormalities in amyotrophic lateral sclerosis are associated with disability and cortical hyperexcitability. Eur J Neurol, 2017. 24(12): p. 1507-1517.
152. Zhou, C., et al., Altered Brain Network in Amyotrophic Lateral Sclerosis: A Resting Graph Theory-Based Network Study at Voxel-Wise Level. Front Neurosci, 2016. 10: p. 204.
153. Muller, H.P., et al., Cortico-efferent tract involvement in primary lateral sclerosis and amyotrophic lateral sclerosis: A two-centre tract of interest-based DTI analysis. Neuroimage Clin, 2018. 20: p. 1062-1069.
154. Spinelli, E.G., et al., Brain MR Imaging in Patients with Lower Motor Neuron-Predominant Disease. Radiology, 2016. 280(2): p. 545-56.
155. Rosenbohm, A., et al., Corticoefferent pathways in pure lower motor neuron disease: a diffusion tensor imaging study. J Neurol, 2016. 263(12): p. 2430-2437.
156. Kondor, R.I.a.L., J., Diffusion Kernels on Graphs and Other Discrete Input Spaces. Proceedings of the International Conference on Machine Learning, 2002: p. 315-322.
157. Poudel, G.R., et al., Network spread determines severity of degeneration and disconnection in Huntington's disease. Hum Brain Mapp, 2019. 40(14): p. 4192-4201.
158. Raj, A., et al., Network Diffusion Model of Progression Predicts Longitudinal Patterns of Atrophy and Metabolism in Alzheimer's Disease. Cell Rep, 2015. 10(3): p. 359-369.
159. Pandya, S., C. Mezias, and A. Raj, Predictive Model of Spread of Progressive Supranuclear Palsy Using Directional Network Diffusion. Front Neurol, 2017. 8: p. 692.
160. Pandya, S., et al., Predictive model of spread of Parkinson's pathology using network diffusion. Neuroimage, 2019. 192: p. 178-194.
161. Neumann, M., et al., Ubiquitinated TDP-43 in frontotemporal lobar degeneration and amyotrophic lateral sclerosis. Science, 2006. 314(5796): p. 130-3.
162. Zhou, J., et al., Predicting regional neurodegeneration from the healthy brain functional connectome. Neuron, 2012. 73(6): p. 1216-27.
163. Brettschneider, J., et al., Spreading of pathology in neurodegenerative diseases: a focus on human studies. Nat Rev Neurosci, 2015. 16(2): p. 109-20.
164. Rascovsky, K., et al., Sensitivity of revised diagnostic criteria for the behavioural variant of frontotemporal dementia. Brain, 2011. 134(Pt 9): p. 2456-77.
165. Folstein, M.F., S.E. Folstein, and P.R. McHugh, "Mini-mental state". A practical method for grading the cognitive state of patients for the clinician. J Psychiatr Res, 1975. 12(3): p. 189-98.

166. Fornito, A., A. Zalesky, and E.T. Bullmore, Network scaling effects in graph analytic studies of human resting-state FMRI data. Front Syst Neurosci, 2010. 4: p. 22.
167. Jenkinson, M., et al., Improved optimization for the robust and accurate linear registration and motion correction of brain images. Neuroimage, 2002. 17(2): p. 825-41.
168. Andersson JL, J.M., Smith S., Non-linear registration, aka spatial normalisation. FMRIB technical report, 2007.
169. Andersson, J.L., S. Skare, and J. Ashburner, How to correct susceptibility distortions in spin-echo echo-planar images: application to diffusion tensor imaging. Neuroimage, 2003. 20(2): p. 870-88.
170. Andersson, J.L. and S.N. Sotiropoulos, Non-parametric representation and prediction of single- and multi-shell diffusion-weighted MRI data using Gaussian processes. Neuroimage, 2015. 122: p. 166-76.
171. Andersson, J.L.R., et al., Susceptibility-induced distortion that varies due to motion: Correction in diffusion MR without acquiring additional data. Neuroimage, 2018. 171: p. 277-295.
172. Andersson, J.L.R. and S.N. Sotiropoulos, An integrated approach to correction for off-resonance effects and subject movement in diffusion MR imaging. Neuroimage, 2016. 125: p. 1063-1078.
173. Le Bihan, D., et al., Artifacts and pitfalls in diffusion MRI. J Magn Reson Imaging, 2006. 24(3): p. 478-88.
174. Tournier, J.-D., F. Calamante, and A. Connelly, MRtrix: Diffusion tractography in crossing fiber regions. International Journal of Imaging Systems and Technology, 2012. 22(1): p. 53-66.
175. Tournier, J.D., F. Calamante, and A. Connelly. Improved probabilistic streamlines tractography by 2 nd order integration over fibre orientation distributions. 2009.
176. Smith, R.E., et al., SIFT: Spherical-deconvolution informed filtering of tractograms. Neuroimage, 2013. 67: p. 298-312.
177. de Reus, M.A. and M.P. van den Heuvel, Estimating false positives and negatives in brain networks. Neuroimage, 2013. 70: p. 402-9.
178. Galantucci, S., et al., Structural brain connectome and cognitive impairment in Parkinson disease. Radiology, 2017. 283(2): p. 515-525.
179. Xia, M., J. Wang, and Y. He, BrainNet Viewer: a network visualization tool for human brain connectomics. PLoS One, 2013. 8(7): p. e68910.
180. Sporns, O. and J.D. Zwi, The small world of the cerebral cortex. Neuroinformatics, 2004. 2(2): p. 145-62.
181. Honey, C.J., et al., Predicting human resting-state functional connectivity from structural connectivity. Proc Natl Acad Sci U S A, 2009. 106(6): p. 2035-40.
182. Schmidt, R., et al., Correlation between structural and functional connectivity impairment in amyotrophic lateral sclerosis. Hum Brain Mapp, 2014. 35(9): p. 4386-95.
183. Suarez, L.E., et al., Linking Structure and Function in Macroscale Brain Networks. Trends Cogn Sci, 2020. 24(4): p. 302-315.
184. Griffa, A., et al., Structural connectomics in brain diseases. Neuroimage, 2013. 80: p. 515-26.
185. Pievani, M., et al., Brain connectivity in neurodegenerative diseases--from phenotype to proteinopathy. Nat Rev Neurol, 2014. 10(11): p. 620-33.
186. Wang, L., et al., Altered small-world brain functional networks in children with attention-deficit/hyperactivity disorder. Hum Brain Mapp, 2009. 30(2): p. 638-49.
187. Whitwell, J.L., et al., Imaging signatures of molecular pathology in behavioral variant frontotemporal dementia. J Mol Neurosci, 2011. 45(3): p. 372-8.
188. Bejanin, A., et al., Longitudinal structural and metabolic changes in frontotemporal dementia. Neurology, 2020. 95(2): p. e140-e154.

189. Storelli, L., et al., Advanced diffusion-weighted imaging models better characterize white matter neurodegeneration and clinical outcomes in multiple sclerosis. J Neurol, 2022. 269(9): p. 4729-4741.
190. Beaulieu, C., The basis of anisotropic water diffusion in the nervous system - a technical review. NMR Biomed, 2002. 15(7-8): p. 435-55.
191. Spinelli, E.G., et al., Typical and atypical pathology in primary progressive aphasia variants. Ann Neurol, 2017. 81(3): p. 430-443.
192. Jeurissen, B., et al., Multi-tissue constrained spherical deconvolution for improved analysis of multi-shell diffusion MRI data. Neuroimage, 2014. 103: p. 411-426.
193. Schneider, T., et al., Sensitivity of multi-shell NODDI to multiple sclerosis white matter changes: a pilot study. Funct Neurol, 2017. 32(2): p. 97-101.
194. Collorone, S., et al., Reduced neurite density in the brain and cervical spinal cord in relapsing-remitting multiple sclerosis: A NODDI study. Mult Scler, 2020. 26(13): p. 1647-1657.
195. Filippi, M., et al., Changes in functional and structural brain connectome along the Alzheimer's disease continuum. Mol Psychiatry, 2020. 25(1): p. 230-239.
196. Seeley, W.W., et al., Neurodegenerative diseases target large-scale human brain networks. Neuron, 2009. 62(1): p. 42-52.
197. Wig, G.S., B.L. Schlaggar, and S.E. Petersen, Concepts and principles in the analysis of brain networks. Ann N Y Acad Sci, 2011. 1224: p. 126-146.
198. Power, J.D., et al., Spurious but systematic correlations in functional connectivity MRI networks arise from subject motion. Neuroimage, 2012. 59(3): p. 2142-54.
199. Satterthwaite, T.D., et al., Impact of in-scanner head motion on multiple measures of functional connectivity: relevance for studies of neurodevelopment in youth. Neuroimage, 2012. 60(1): p. 623-32.
200. Van Dijk, K.R., M.R. Sabuncu, and R.L. Buckner, The influence of head motion on intrinsic functional connectivity MRI. Neuroimage, 2012. 59(1): p. 431-8.
201. Ciric, R., et al., Benchmarking of participant-level confound regression strategies for the control of motion artifact in studies of functional connectivity. Neuroimage, 2017. 154: p. 174-187.
202. Pandya, S., et al., Modeling seeding and neuroanatomic spread of pathology in amyotrophic lateral sclerosis. Neuroimage, 2022. 251: p. 118968.